Dissertation

Studies on Minimum Quantity Lubrication in Turning Process

- Simplified and practical evaluation of lubricating and cooling effects of oil mist by means of Finite Element Method -

旋削加工における **MQL**（最少量潤滑）に関する研究

–有限要素法によるオイルミストの潤滑および冷却効果の簡易的かつ実践的評価法–

Graduate School of Natural Science & Technology

Kanazawa University

Division of Mechanical Science and Engineering

Student ID Number : 1424032001

Name : Ahmad Shahir bin Jamaludin

Chief advisor : Prof. Akira Hosokawa

Date of Submission : 24th March 2017

TABLE OF CONTENT

CHAPTER 1

INTRODUCTION

1.1 Research background

Consumer products, such as machine components or elements, had gone through manufacturing processes to obtain desired shapes, dimensional accuracy and surface integrity. There are several methods applied during the processes, one of them is called material removal process, such as cutting, grinding, laser machining, and electrical discharge machining (EDM) [1-5]. In the metal-cutting process, there are two main types of material removal method. One of them is called turning process, while the other, is called milling process. In turning process, workpiece is rotated to be cut by a fixed tool, capable of various applications such as cylindrical machining. On the other hand, in milling process, the tool is rotated onto a workpiece to remove unwanted material to make a desired shape. In both cases, cutting tool plays an important role during the machining process with respect to chip formation, surface roughness and cutting energy [1-5].

In the metal-cutting process, the majority of the cutting energy is consumed by the plastic deformation occurring in the shear plane of the workpiece. Additionally, most of the energy is changed into heat, which promotes higher tool wear rate and greatly affected the

quality of the surface finish of machined materials, which leads to the increment of production cost [1-5].

Conventionally, cutting oil is supplied in an excessive amount to the cutting point, which greatly influences product quality, as well as processing cost. The cutting oil plays a role in removing the heat from the work material and the cutting edge. In addition, cutting oil enables to reduce the cutting resistance by decreasing the friction coefficient due to the penetration between workpiece and tool flank plays a lubricating action [6-11]. It is believed that at a higher level, the cutting oil is capable of preventing oxidation onto the finished surface. Furthermore, cleaning process is needed for oil substance attached onto the workpiece after the process in the conventional method of supplying cutting oil during the machining process. The process adds an extra increment to the cost of waste oil management, and contaminates the working environment and soil due to the generated waste [12]. In spite of the importance and effectiveness of cutting fluid, conventional wet cutting method tends to shift to dry or semi-dry cutting processes, where a minuscule amount of cutting oil will be applied during the cutting process due to the economical and/or environmental reissues [12].

One of the most typical semi-dry machining is called MQL (Minimum Quantity Lubrication), in which fine droplets of cutting oil are mixed with the pressurized air and supplied to the proximity of the cutting zone [13]. The amount of lubricant applied is extremely small, approximately 1/10000 times of the amount of cutting oil in the conventional wet cutting process, which is expected capable in cooling-lubricating action, promoted as environmentally friendly processing technology. However, the currently available semi-dry cutting method is limited to a short period of processing time, due to inefficiency to remove heat as cutting temperature rises dramatically with increasing cutting speed [7-20].

1.2 Objectives of the study

This study aims to propose a new MQL system in turning difficult-to-machine materials. Additionally, finite-element analysis is applied to obtain more information in proposing this brand-new MQL system, which is called 'Extreme Cold Mist'. In the process, 2 FEM analyses are proposed as summarized as **Fig 1.1.**

Nevertheless, currently available FEM model is unable to estimate or calculate the effect of MQL properties and its characteristic, due to complexity in simulating inhomogeneous properties MQL mist molecule itself. Thus, in Stage I, a model that capable of estimating MQL by FEM method is proposed. In obtaining appropriate FEM model in evaluating the effect of Minimum Quantity Lubrication, FEM analytical models are designed

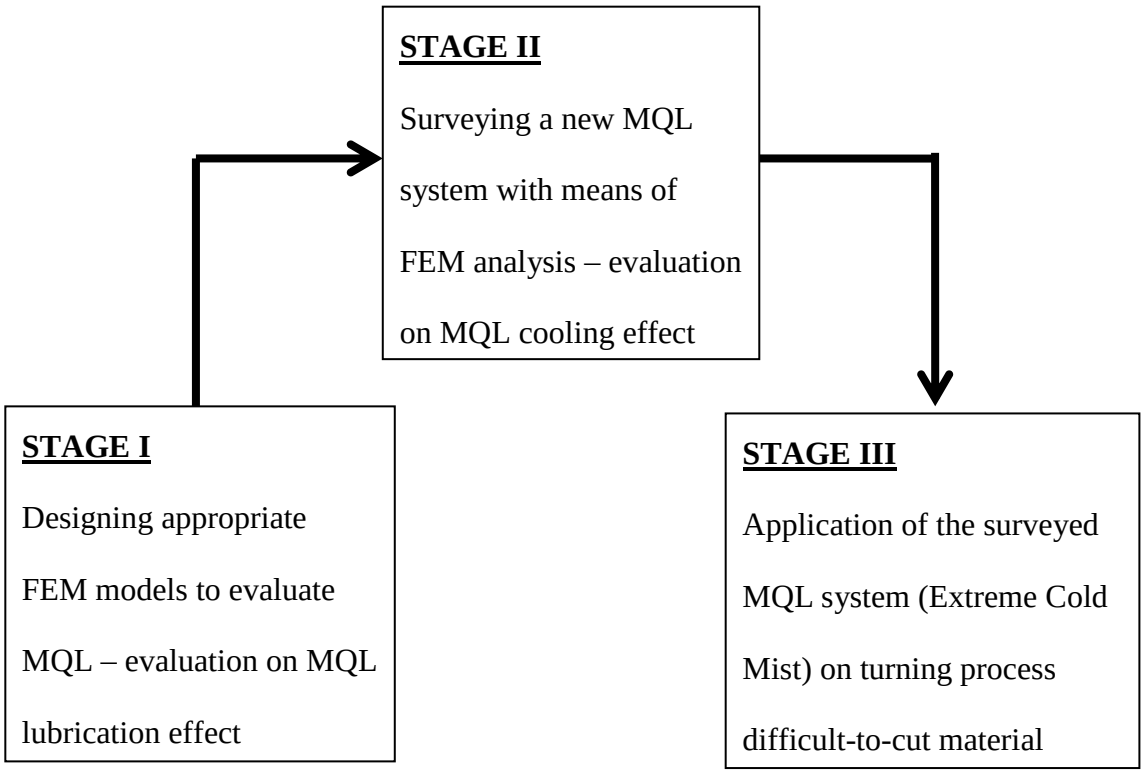

Fig. 1.1: Stages required in proposing a new MQL system

and executed using the application package software Deforms™-3D. In the meantime, equivalent orthogonal cutting tests are executed in order to verify FEM model, as well as the appropriate parameters for MQL analysis. Several MQL systems are utilized to gain more information and clear understanding on the lubrication and cooling effects during the cutting process with MQL.

In the next stage of the study, Stage II, a brand-new MQL system (Extreme Cold Mist) is surveyed with the application of the FEM model obtained from Stage I to understand its effect onto cutting temperature. During the survey of this new MQL system (Extreme Cold Mist), the effects of environment temperature and convective heat transfer coefficient are taken into consideration and studied.

In the final part of the study, Stage III, the surveyed MQL system (Extreme cold mist) is applied onto the actual turning process of difficult-to-cut material, stainless steel SUS316. Comparison with various MQL systems is done to prove the effectiveness of the new Extreme Cold Mist MQL system during the conventional turning process.

1.3 Thesis outline

This study aims to invent a highly effectiveness MQL system in turning process through several stages, from the evaluation of the effect of MQL, until the utilization of the newly invented MQL system in the actual turning process.

In the Chapter 2, overview of the fundamental of the metal-cutting process is covered.

In the Chapter 3, FEM models design is explained. A number of models are designed, expecting to be able to evaluate the MQL process. Several parameters such as cutting force,

chip thickness and contact length between tool and chip are analyzed. The most effective model in simulating and estimating MQL process is explained.

In the Chapter 4, the analyses continue with the application of designed FEM model from previous chapter in evaluating the effect of MQL as coolant. Parameters such as room temperature and heat convection coefficient to the environment are taken into consideration. At the end of the chapter, a new MQL is surveyed with the application of FEM simulation.

In the Chapter 5, the temperature measurement method applied throughout the study is explained. This chapter explains the overview of the pyrometer construction. The emission of infrared heated cutting tool edge is appreciated, and temperature is measured by the ratio between photovoltaic InAs element and InSb element.

In the Chapter 6, the surveyed MQL system (Extreme Cold Mist) is applied onto the actual turning process. The experimental results in terms of cutting force, cutting temperature and surface quality from various types of MQL methods in turning process of difficult-to-cut material, stainless steel SUS316 is analyzed and compared.

In the Chapter 7, all the work is concluded.

References:

[1] Groover, M. P. (1996). *Fundamentals of modern manufacturing: materials, processes, and systems*. Upper Saddle River, NJ: Prentice Hall.

[2] Kalpakjian, S. (2001). *Manufacturing engineering and technology*. Upper Saddle River, NJ: Prentice Hall.

[3] Astakhov, V. P. (2005). On the inadequacy of the single-shear plane model of chip formation. *International Journal of Mechanical Sciences, 47*(11), 1649-1672.

[4] Vaughn, R. L. (1966). Modern Metals Machining Technology. *Journal of Engineering for Industry, 88*(1), 65.

[5] Devries, W. R. (1992). Analysis of Material Removal Processes. *Springer-Verlag Publications*, New York.

[6] Hadad, M., & Sadeghi, B. (2013). Minimum quantity lubrication-MQL turning of AISI 4140 steel alloy. *Journal of Cleaner Production, 54*, 332-343.

[7] Liao, Y., & Lin, H. (2007). Mechanism of minimum quantity lubrication in high-speed milling of hardened steel. *International Journal of Machine Tools and Manufacture, 47*(11), 1660-1666.

[8] Zhang, S., Li, J., & Wang, Y. (2012). Tool life and cutting forces in end milling Inconel 718 under dry and minimum quantity cooling lubrication cutting conditions. *Journal of Cleaner Production, 32*, 81-87.

[9] Werda, S., Duchosal, A., Quilliec, G. L., Morandeau, A., & Leroy, R. (2016). Minimum Quantity Lubrication: Influence of the Oil Nature on Surface Integrity. *Procedia CIRP, 45*, 287-290.

[10] Lawal, S. A., Choudhury, I. A., & Nukman, Y. (2013). A critical assessment of lubrication techniques in machining processes: a case for minimum quantity lubrication using vegetable oil-based lubricant. *Journal of Cleaner Production, 41*, 210-221.

[11] Shokoohi, Y., Khosrojerdi, E., & Shiadhi, B. R. (2015). Machining and ecological effects of a new developed cutting fluid in combination with different cooling techniques on turning operation. *Journal of Cleaner Production, 94*, 330-339.

[12] Hsien, W. L. (2014). Utilization of Vegetable Oil, Solid Lubricant, Mist Lubrication, Minimum Quantity Lubrication (MQL) in Machining. *Springer Briefs in Molecular Science Towards Green Lubrication in Machining*, 19-31.

[13] Ueda, T., Hosokawa, A., & Yamada, K. (2006). Effect of Oil Mist on Tool Temperature in Cutting. *Journal of Manufacturing Science and Engineering, 128*(1), 130.

[14] Kamata, Y., Obikawa, T., & Shinozuka, J. (2004). Analysis of Mist Flow in MQL Cutting. *Key Engineering Materials, 257-258*, 339-344.

[15] Ueda, T., Nozaki, R., & Hosokawa, A. (2007). Temperature Measurement of Cutting Edge in Drilling -Effect of Oil Mist-. *CIRP Annals - Manufacturing Technology, 56*(1), 93-96.

[16] Dhar, N., Kamruzzaman, M., & Ahmed, M. (2006). Effect of minimum quantity lubrication (MQL) on tool wear and surface roughness in turning AISI-4340 steel. *Journal of Materials Processing Technology, 172*(2), 299-304.

[17] Cabanettes, F., Faverjon, P., Sova, A., Dumont, F., & Rech, J. (2016). MQL machining: from mist generation to tribological behavior of different oils. *The International Journal of Advanced Manufacturing Technology*.

[18] Dasch, J. M., & Kurgin, S. K. (2010). A characterisation of mist generated from minimum quantity lubrication (MQL) compared to wet machining. *International Journal of Machining and Machinability of Materials, 7*(1/2), 82.

[19] Dhar, N., Ahmed, M., & Islam, S. (2007). An experimental investigation on effect of minimum quantity lubrication in machining AISI 1040 steel. *International Journal of Machine Tools and Manufacture, 47*(5), 748-753.

[20] Sasahara, H., Satake, K., Takahashi, W., Goto, M., & Yamamoto, H. (2016). The effect of oil mist supply on cutting point temperature and tool wear in driven rotary cutting. *Precision Engineering*.

CHAPTER 2

OVERVIEW ON FUNDAMENTAL OF METAL CUTTING

2.1 Introduction

In this section, fundamental of metal cutting will be overviewed as well as the theories and previous works related to finite-element analysis on cutting process will be explained. In the metal cutting analysis, there are two types of cutting model commonly utilized, which are called as orthogonal and oblique cutting. During the orthogonal cutting, the chip is removed by the cutting edge which is parallel to the uncut surface (**Fig. 2.1**). [1-3]. Meanwhile, in the oblique cutting, the chip is removed by cutting edge that is inclined with an inclination angle in the direction of the tool feed and the work feed (**Fig. 2.2)**.

Most of conventional machining process is considered as oblique cutting, but orthogonal cutting has been extensively utilized during analysis due to its simplicity and easier to be understood, when equivalent chip formation is taken into assumption for both cutting model [1-3].

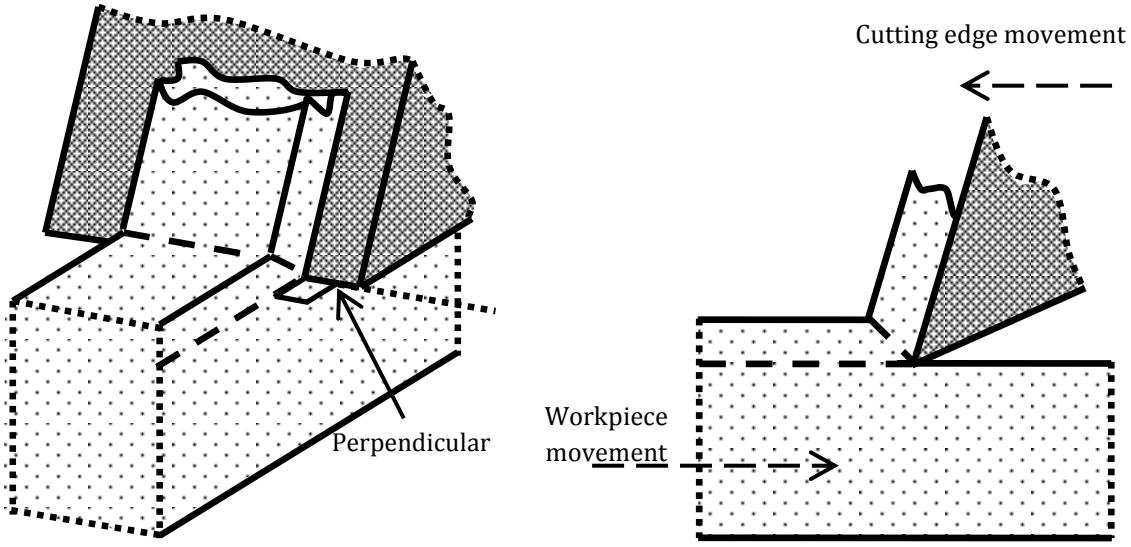

Fig. 2.1 Orthogonal cutting

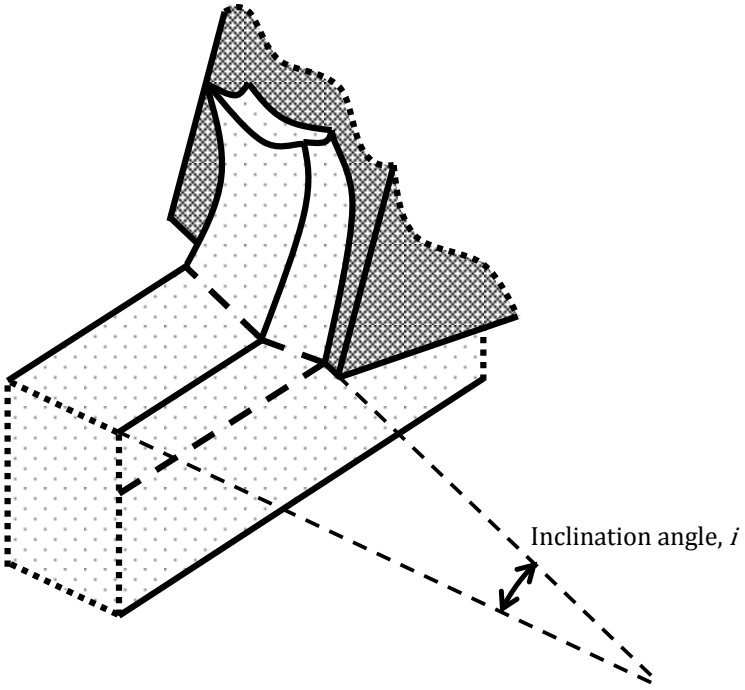

Fig. 2.2 Oblique cutting

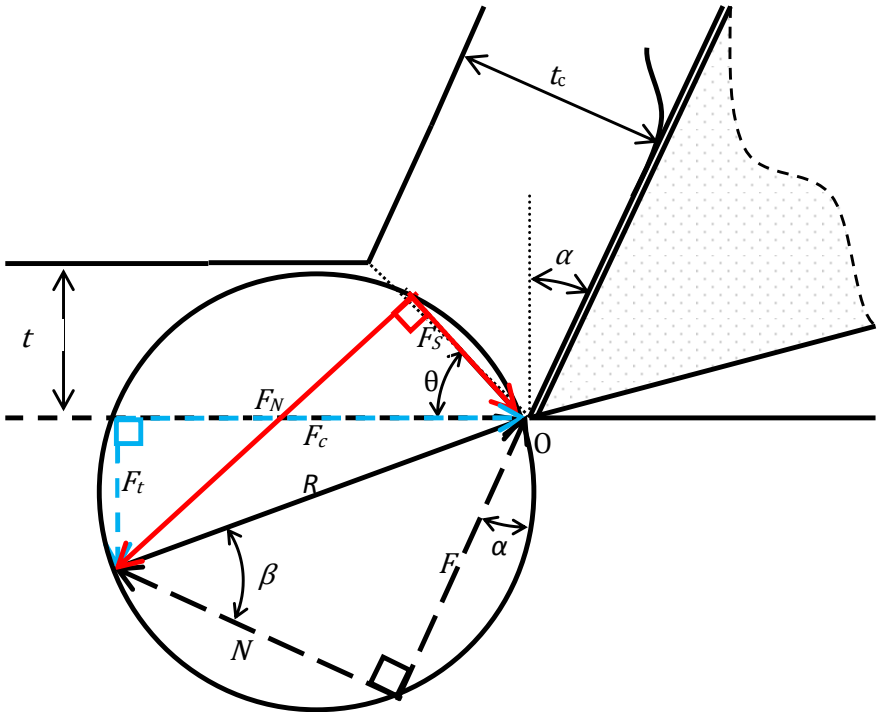

Fig. 2.3 Merchant thin zone model and force diagram

2.2 Physical behavior of material during cutting process

Previous researchers have been extensively studied about the physical behavior involved during a cutting process. Earlier FEM models represented basic mechanics of analytical models. In general, metal-cutting process involves removing process of unwanted materials from the workpiece. Several reliable models were developed by the previous researchers to represent this process called slip line models. There are two types of slip line models being utilized in the analysis; thin zone model and thick zone slip line model [1-9].

2.2.1 Thin zone slip line model

Thin zone slip line model is a simplified slip line model to describe formation of chip during high cutting speed, based on the following assumptions [10]:

i) Material deformation is two-dimensional

ii) The cutting tool edge is totally sharp,

iii) Cutting tool is assumed only to be in contact with cutting chip on the rake face

iv) Rubbing or contact is not occurred between cutting tool and workpiece.

v) Equal resultant force existed on the shear plane, collinear with the force applied across the tool-chip interface from opposite direction.

vi) Uniform stress is distribution across the shear plane.

Fig. 2.3 shows the force diagram where the assumptions are applied, which is known as Merchant Force Diagram. Technically, two force components, F_p and F_t are taken into consideration, as the direction and magnitude of resultant force R is variable. These force components are shown as **Eqs. (2.1)** and **(2.2)**. (α: rake angle, β: friction angle, b: width-of-cut, t: undeformed chip thickness)

$$F_p = \frac{tb\tau \cos(\beta - \alpha)}{\sin\theta \cos(\theta + \beta - \alpha)} \tag{2.1}$$

$$F_t = \frac{tb\tau \sin(\beta - \alpha)}{\sin\theta \cos(\theta + \beta - \alpha)} \tag{2.2}$$

Shear stress, τ is considered constant over the shear plane, and assumed equals to workpiece material shear yield stress. Shear angle θ is considered as an important metal-

cutting parameter. Shear angle depicts the deformation characteristic during the machining process. Principle of minimum energy is taken into assumption when a constant cutting speed is applied, where $dF_p/d\theta = 0$, as is shown in **Eq. (2.3)**.

$$\frac{dF_p}{d\theta} = \frac{tb\tau \cos(\beta - \alpha)\cos(2\theta + \beta - \alpha)}{\sin^2\theta \cos^2(\theta + \beta - \alpha))} = 0 \tag{2.3}$$

From **Eq. (2.3)**, θ is calculated as **Eq. (2.4)**.

$$\theta = \frac{\pi}{4} - \frac{1}{2}(\beta - \alpha) \tag{2.4}$$

The relationship between chip thickness t_c, undeformed chip thickness t and chip ratio r are shown in **Eq. (2.5)**. Meanwhile, the relationship between chip ratio, r and shear angle, θ as shown in **Eq. (2.6)**.

$$\frac{t_c}{t} = r \tag{2.5}$$

$$\tan\theta = \frac{r\cos\alpha}{1 - r\sin\alpha} \tag{2.6}$$

Shear force F_S and normal force F_N are shown by **Eqs. (2.7)** and **(2.8)**.

$$F_S = F_p \cos\theta - F_t \sin\theta \tag{2.7}$$

$$F_N = F_p \sin\theta + F_t \cos\theta \tag{2.8}$$

Shear stress τ and normal stress σ are shown as **Eqs. (2.9)** and **(2.10),** referring to **Eqs. (2.7)**, **(2.8)**, **(2.1)** and **(2.2)**,

$$\tau = \frac{F_S}{A_s} = \frac{\left(F_p \cos\theta - F_t \sin\theta\right)\sin\theta}{bt} \tag{2.9}$$

$$\sigma = \frac{F_N}{A_s} = \frac{\left(F_p \sin\theta + F_t \cos\theta\right)\sin\theta}{bt} \tag{2.10}$$

Chip's velocity v_c and shear velocity v_s in **Fig. 2.4** are expressed as **Eqs. (2.11)** and **(2.12)**.

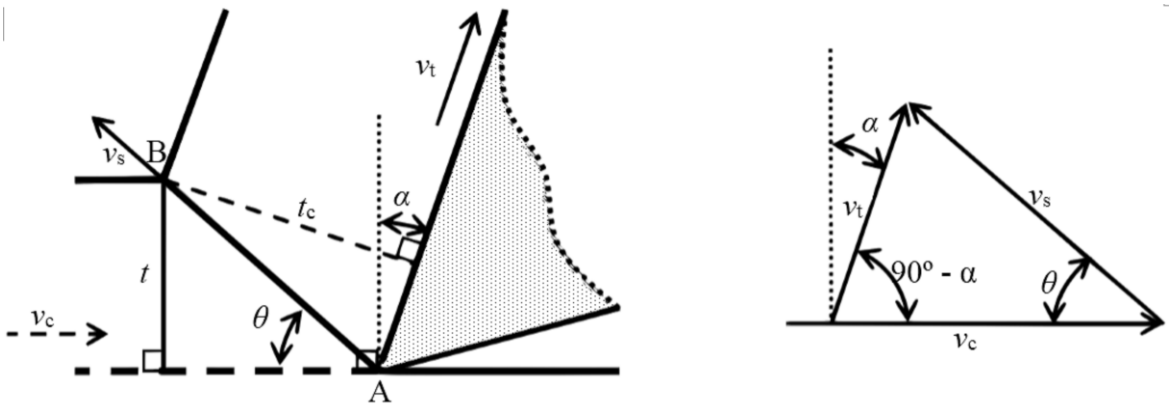

Fig. 2.4 Relationship of shear angle θ with (a) chip thickness t_c, (b) velocities v

$$v_w = \frac{\sin\theta}{\cos(\theta - \alpha)} v_c = r v_c \tag{2.11}$$

$$v_s = \frac{\cos\theta}{\cos(\theta - \alpha)} v_w \tag{2.12}$$

Here we denote shear zone thickness as Δy, shear strain ε and strain rate $\dot{\varepsilon}$ are given as **Eqs. (2.13)** and **(2.14).**

$$\varepsilon = \tan(\theta - \alpha) + \cos\theta \tag{2.13}$$

$$\dot{\varepsilon} = \frac{v_s}{\Delta y} = \frac{\cos\alpha}{\cos(\theta - \alpha)} \frac{v_w}{\Delta y} \tag{2.14}$$

2.2.2 Thick zone slip line model

Thick zone slip line model is considered complex and describes the deformation of material at low cutting speed. Previous study applied the assumption of ideal plastic deformation of workpiece material [11]. It is assumed that shear stresses τ_{OA} , τ_{OB} and τ_{OD} are equivalent to material flow stress *k*, based on Okushima and Hitomi's thick zone slip line model, as shown in **Eq. (2.15)** [11].

$$\tau_{OA} = \tau_{OB} = \tau_{OD} = k \tag{2.15}$$

It can be understood that, τ_{OA}, τ_{OB} and τ_{OD} are described as **Eqs. (2.16)**, **(2.17)** and **(2.18)** by referring to **Fig. 2.5** (*b*: width-of-cut, l_c: tool-chip contact length).

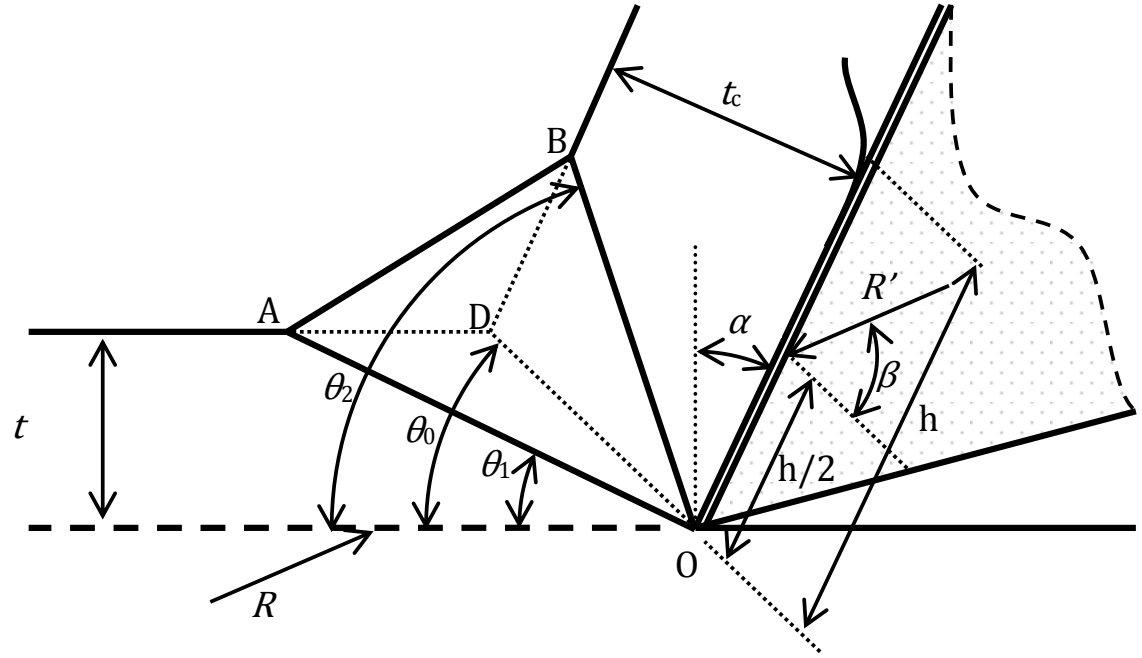

Fig. 2.5 Okushima and Hitomi's thick zone model

$$\tau_{\mathrm{OA}} = \frac{R \sin\theta_1 \cos(\theta_1 - \alpha + \beta)}{bt} \tag{2.16}$$

$$\tau_{\mathrm{OB}} = \frac{R \cos(\theta_2 - \alpha) \cos(\theta_2 - \alpha + \beta)}{bt_c} \tag{2.17}$$

$$\tau_{OD} = \frac{R \sin\beta}{bl_c} \tag{2.18}$$

Meanwhile, the angles θ_1 and θ_2 are expressed as **Eqs. (2.19)** and **(2.20)**.

$$\theta_1 = \frac{K_1}{2} - \frac{\beta}{2} + \frac{\alpha}{2} \tag{2.19}$$

$$\theta_2 = \frac{K_2}{2} - \frac{\beta}{2} + \frac{\alpha}{2} \tag{2.20}$$

Here K_1 and K_2 denote as **Eqs. (2.21)** and **(2.22)**, respectively.

$$K_1 = \sin^{-1}\left[\frac{2t}{h}\sin\beta + \sin(\beta - \alpha)\right] \tag{2.21}$$

$$K_2 = \cos^{-1}\left[\frac{2t_c}{h}\sin\beta - \cos\beta\right] \tag{2.22}$$

In the thick zone model, shear strain at A and B are described as **Eqs. (2.23)** and **(2.24)**.

$$\gamma_{\mathrm{A}} = 0 \tag{2.23}$$

$$\gamma_{\mathrm{B}} = \cot\theta_2 + \tan(\theta_2 - \alpha) \tag{2.24}$$

2.2.3 Flow stress constitutive material models

The material flow stress models derive the relationship of true strain, strain rate and temperature onto true stress [12-14] of a material. Several well-known flow stress constitutive material models are discussed as below.

a) Power Law Material Model

Power Law material model (**Eq. (2.25))** has been extensively utilized in estimating the flow stress for assorted materials with very large range of strain rate and temperature [12]. Meanwhile, when temperature effect onto strain rate is taken into consideration, Macgregor's material model is derived from Power law material model (**Eq. (2.26))**. The term T_{mod} represents the velocity-modified temperature which have inverse relationship with flow stress, where increasing temperature reduce the flow stress magnitude [13] (σ: True stress, *C*: Strength coefficient, ε: true strain, *n*: strain hardening, ε̇: strain rate, *m*: strain rate hardening, *n:* strain hardening for T_{mod} function).

$$\sigma = C\varepsilon^{n}\dot{\varepsilon}^{m} \tag{2.25}$$

$$\sigma = \mathrm{C}\,(\mathrm{T_{mod}})\varepsilon^{\mathrm{n(T_{mod})}} \tag{2.26}$$

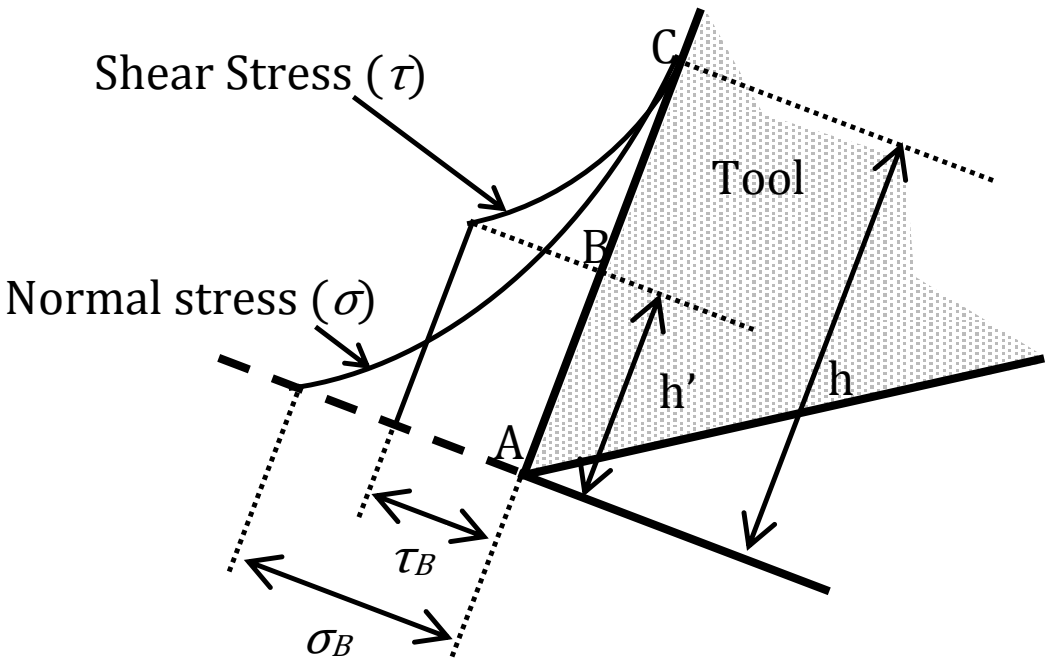

Fig. 2.6: Zorev's shear stress distribution (Zorev, 1963)

b) Johnson-Cook Material Model in **Eq. (2.27)**

Johnson-Cook material model has been commonly employed for various materials. Since plastic deformation is usually the main deformation at high deformation rate, no elastic range is considered. [14].

$$\sigma_{JC} = (A + B\varepsilon^{n})(1 + C \ln \dot{\varepsilon})\left(1 - T^{k^{m}}\right) \tag{2.27}$$

where, $T^{k} = (T - T_{room}) / (T_{melt} - T_{room})$,
(A, B, C, n and m are constants)

2.3 Contact mechanics and friction during cutting process

In gaining more understandings on chip formation during metal cutting with FEM, contact mechanic during cutting process is one of the essential elements needs to be taken into consideration. When chip is formed after being separated by blade/tool edge from workpiece, it will remain in contact with a certain length of the blade/tool surface from tool cutting edge, called tool-chip contact length, l_c, where it has direct relationship with the frictional condition. In the meantime, the heat generation is also affected by the size of contact length l_c, and this phenomenon is related to the wear generation during the metal-cutting process on tool-chip interface.

Table 2.1 Example of tool-chip contact length model

Eq.	**Model**	**Equation**	**Work material (cutting speed v_c m/min)**
(2.28)	Lee and Shaffer	$l_c = \frac{t\sqrt{2}}{\sin\theta \sin(\pi/2 + \theta - \alpha)}$	Mild Steel
(2.29)	Kato et al. Toropov & Ko	$l_c = 2t_c$	Al 6061 (1000) Copper (800) AISI 1045 (300) AISI 304 (140)
(2.30)	Tay et al.	$l_c = \frac{t \sin\vartheta}{\cos\alpha \sin\theta}$	AISI 1016 (300)

2.3.1 Tool-chip contact length

The tool-chip contact length during a cutting process is assumed equivalent to the sum of the lengths for sticking and sliding region during one cutting process (**Fig. 2.6)**. In the sticking region (region AB), it is assumed that contact shear stress is at maximum value and uniform. Meanwhile, in the sliding region (region BC), contact shear stress is decreasing down to zero until the chip is separated from the tool rake face in a power function.

This tool-chip contact length l_c is an important cutting parameter, as it is interrelated to the shear angle, slip-line characteristic, and stress distribution [11]. In most of the studies, tool-chip contact length is obtained based on empirical data, as shown in **Table 2.1**.

2.3.2 Contact Friction

The occurrence of friction during a metal-cutting process between the contact areas of cutting tool, removed chip and newly generated surface, is considered as complex, as cutting parameters (feed rate *f*, cutting speed v_c and rake angle *a*) have critical influence to the

interface between tool, workpiece and chip, due to high normal pressure on the contact surface [15]. There are two basic types of the friction model, as shown in the following:

a) Coulomb friction model

Previous researchers state that the frictional force has a direct relationship to the normal force acting on the object to a certain factor, as shown in **Eq. (2.31) (***F*: frictional force, μ: Coulomb friction coefficient, *N*: normal force).

$$F = \mu N \tag{2.31}$$

Previous researchers had developed one of the earliest models to explain the friction occurred during metal cutting with the application of Coulomb friction, based on the assumptions as following [1-8];

i) Workpiece shearing was largely contained within a plane with an inclination angle, β

ii) A constant friction coefficient works on the resulting chip sliding surface (rake face) (refer to **Fig. 2.3**) as described in **Eq. (2.32)**.

$$\mu = \frac{F}{N} = \frac{(F_c \sin\alpha + F_t \cos\alpha)}{(F_c \cos\alpha - F_t \sin\alpha)} = \frac{(F_t + F_c \tan\alpha)}{(F_c - F_t \tan\alpha)} = \tan\beta \tag{2.32}$$

b) Shear friction model

Subsequent work regarding to the friction during metal cutting had been reported by many researchers. Previous researchers justified that, the variable local friction coefficient *m* occurs over the tool-chip contact length l_c is variable (referring to **Fig. 2.6**), and discover that

constant shear stress exist partially over the tool-chip contact length l_c. Furthermore, normal stress decreases to zero from point A to point C, as shown in **Fig. 2.6**.

The region between point A to B is defined as sticking region, where normal stress σ_n is extremely high and the chip is deformed plastically, resulting the chip to stick on the tool rake face. The magnitude of the normal force *N* affected the friction coefficient, which is not constant

Additionally, the zone between point B to C is defined as sliding friction, where the area of contact does not approach unity to the total area ratio. Therefore, frictional coefficient is constant in this region, where the frictional force is directly proportional to the apparent area of contact and independent to the normal force *N*.

It is assumed that, the appearance of friction coefficient is an average value based on both regions, according to **Eq. (2.29)**. The lengths A-B and B-C will change according to the change of cutting conditions, subsequently change the value of the friction coefficients. In shear friction model, constant frictional stress is assumed on the rake face and the relationship of frictional stress, τ and shear flow stress, k is shown as **Eq. (2.33)** [15-19]. Here, m is constant friction factor.

$$\tau = mk \tag{2.33}$$

In the earlier metal-cutting process FEM models, constant friction coefficient is assumed for the entire chip-tool interface based on Coulomb's law. Usui and Shirakashi (1982) proposed a pioneer friction model, where frictional stress is estimated from a function of normal stress depicted by **Eq. (2.34)** ($\tau_{f:}$ frictional stress, σ_n: normal stress, $k_{primary:}$ shear flow stress, μ: friction coefficient [19-21].

$$\tau_f = k_{primary}\left[1 - e^{\left(\mu\frac{\sigma_n}{k_{primary}}\right)}\right] \tag{2.34}$$

Shih (1990) considered sticking-sliding regions in explaining the friction phenomenon during metal cutting. The friction force in sticking region is assumed constant, while the friction force is assumed varying in sliding region [19-21].

Ozel (2006) applied various combinations of the friction model to obtain precise machining results of the tool-chip interface and estimated shear friction coefficient m = 0.82 from the experimental data reported by Childs et al. (1997) [19-21].

2.4 Heat generation during cutting process

Cutting-edge temperature has a consequential effect onto the characteristic of the machining process, since it greatly influences the tool life, tool wear progress, surface integrity and dimensional accuracy of work materials. **Fig. 2.8** shows the main heat generated zones during a conventional cutting process. These temperatures influence surface integrity and machining accuracy, due to occurrence of thermal expansion during machining and metallurgical changes.

(i) Primary deformation zone

In the primary deformation zone, the plastic shearing process done at the shear plane is releasing heat and considered the main source of heat. The large amount of heat affects the mechanical properties of the work and tool materials.

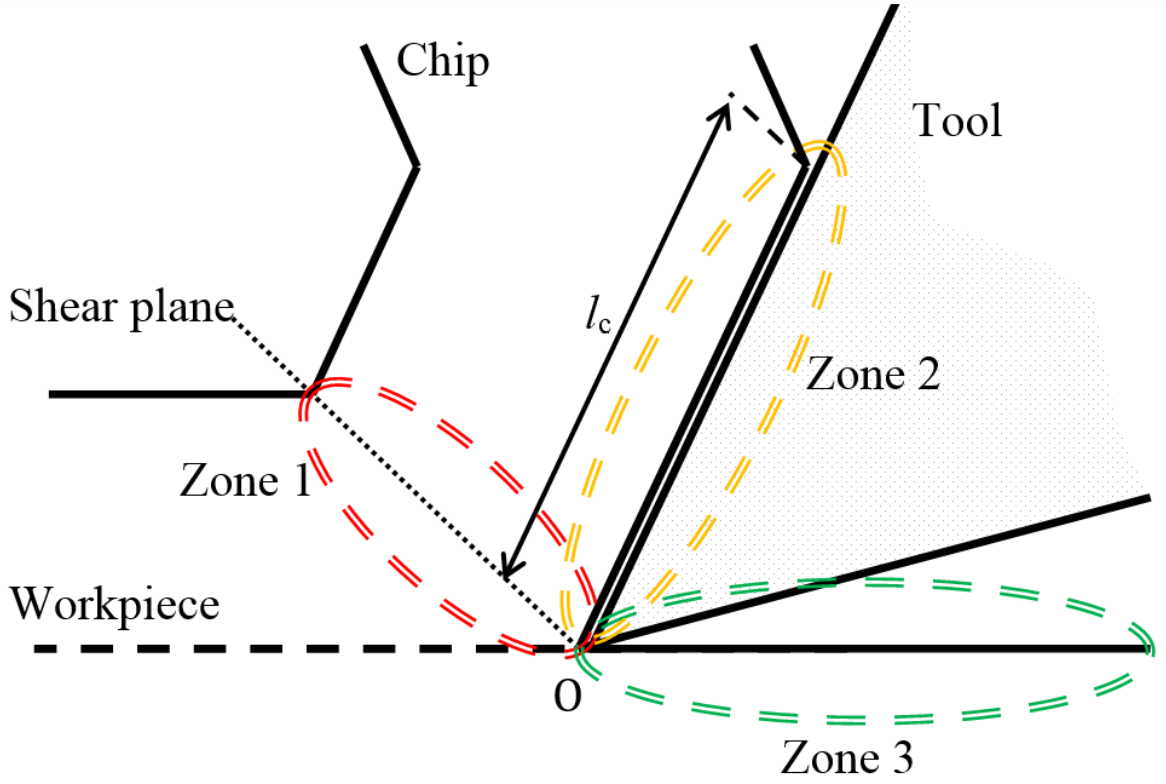

Fig 2.8: Main heat generation zones during cutting process

(ii) Secondary deformation zone

In the secondary deformation zone, the deformation of chip and frictional contact of tool-chip interface become the source of heat generation. The heat generation and magnitude of temperature are highly affected by cutting conditions.

(iii) Tertiary deformation zone

In tertiary deformation zone, frictional contact between tool edge and machined surface become the source of heat generation. The heat generation and magnitude of temperature are highly affected by tool wear and workpiece surface finish.

Numerous studies designed an orthogonal steady-state shear plane model in developing the method for determining the cutting temperature from the chip formation. Plastic deformation occurred in the shear plane generates heat (primary deformation zone),

and the heat flows inside the chip through conduction, into the tool through high-pressure frictional contact with chip and flows within the tool by conduction (secondary deformation zone). Additionally, from the moving chip and workpiece, the heat is also transferred into the environment through convection. Previous study made FEM model for temperature analysis according to following assumptions:

i) The machining process is steady.

ii) The tool, chip and work materials is continuous, homogeneous and isotropic as the crystalline of the work material is relatively small.

iii) The process is two dimensional.

iv) The tool is sharp.

Primary deformation zone shear energy is assumed distributed uniformly, where the rate of shear energy U_s is generated into heat in this zone is given by **Eqs. (2.35)** while F_s, v_s and ϕ are defined by **Eqs. (2.36) and (2.37) (**F_s: shear force along shear plane OA, v_s: relative shear velocity)**.**

$$U_s = F_s v_s \tag{2.35}$$

$$F_S = F_h \cos\phi - F_v \sin\phi \tag{2.36}$$

$$v_S = \frac{V\cos\alpha}{\cos(\phi-\alpha)}, \qquad \phi = tan^{-1}\frac{\frac{t}{t_c}\cos\alpha}{1-\frac{t}{t_c}\sin\alpha} \tag{2.37}$$

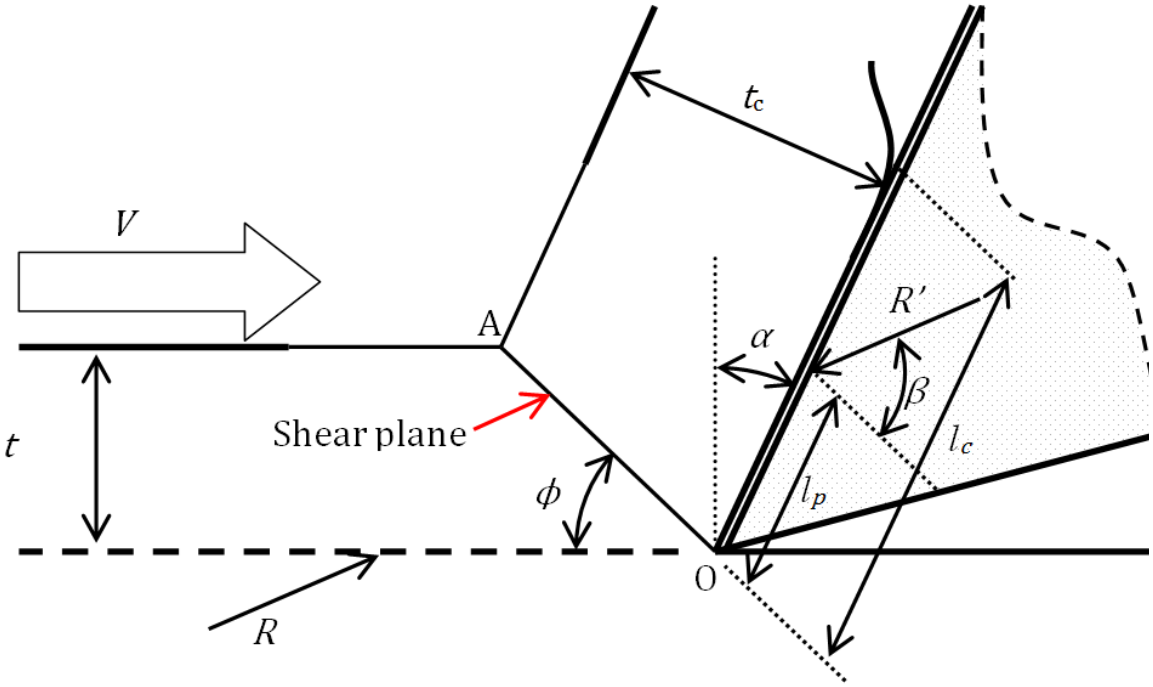

Fig. 2.9: Relationship of cutting parameters and heat generation

F_h and F_v are the horizontal and vertical component of force, respectively, which is determined experimentally. The rate of shear energy per unit area u_s, by assuming it is distributed uniformly, can be written as the **Eq. (2.38)** (b: width-of-cut, t: undeformed chip thickness). Meanwhile, heat flux is expressed as **Eq. (2.39)**, where it is assumed that all mechanical energy is transformed into heat (J = 1.00 N·m/J, mechanical equivalent of heat).

$$u_s = \frac{F_s v_s \sin \emptyset}{tb} \tag{2.38}$$

$$q_s = \frac{F_s V_s}{Jtb \csc \phi} \tag{2.39}$$

2.5 Wear Mechanism in Metal Cutting

Cutting tools' replacement cost is having a major fraction in the total operation cost. The cutting tool life span is estimated from its wear parameter. Capabilities of predicting tool life and understanding on tool wear mechanisms are important and necessary. This is due to economics and precision of machining operations effected by tool wear [27-37]. Wear in cutting tool occurs in many different ways [27], such as:

- Edge wear/flank wear

Edge wear and flank wear is normal, slow types of tool wear. However, these types of wear will accelerate when the work material is highly abrasive.

- Cratering or top wear

Cratering takes place behind the cutting edge, and occurs regularly in machining long chipping steels. If the crater increases large enough until reaching the cutting edge, the tool will fail instantly.

- Chipping

Chipping on a tool edge is a form of tool failure unable to be predicted. It is usually started when a high point on an edge breaks off. A stronger carbide grade, varied edge preparation, or lead angle modification may remove chipping.

- Deformation

Deformation of a tool or insert is due to heat build-up, difficult to be detected without the use of a microscope, although very detrimental to the machining process. Utilization of lower cutting speed or high heat-resistant tool often helps to prevent wear caused by deformations.

Numerous research works are done, trying to come out appropriate method to suppress the wear progress. In metal-cutting, there are four well known tool wear mechanisms [32], which are:

- Abrasive wear

Abrasive wear is caused by the tool material that is removed by hard particles (hard elements, unstable built-up edge etc.) existed in the tool-workpiece interface [32].

- Adhesive wear

Adhesive wear is caused by the removal or fracture of less wear resistance zone of cutting tool [32].

- Oxidation wear:

Oxidation wear is caused by the rapid formation of soft oxide layers, e.g. CO_3O_4, CoO, WO_3, TiO_2 etc. on tool face at high temperature, and then removed by chip and workpiece [32].

- Diffusion wear

Diffusion wear is caused by the movement of tool material's atom to the workpiece material due to concentration difference. The increases of temperature affected the rate of diffusion increment exponentially [28].

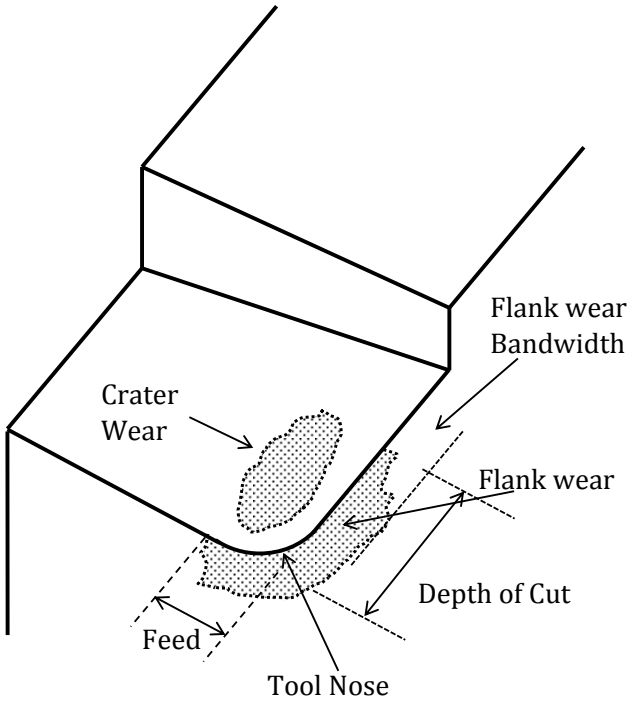

Fig. 2.10: Tool wear phenomenon in turning

During orthogonal and oblique cutting, severe friction phenomena occurred on the tool rake and flank face are mainly caused by the high frictional stress at the tool rake-face and the chip interface, where varieties of wear pattern and scars can be observed, as shown in **Fig. 2.10** [32]. Flank wear (the formation of a wear land on the flank face) is not uniform and the common cause of this flank wear is abrasive wear, which can be estimated by measuring the change of the tool size or by observing its appearance [29].

During a conventional cutting condition, three main typical stages of tool wear can be observed. **Fig. 2.11** shows the typical stages of the tool wear. The typical stages of wear are known as initial wear (pre-wear), steady wear, and severe wear [3].

Surface oxidation and micro-cracking, are mainly the cause of increasing size of the tool wear in the initial wear region. High contact pressure due to small contact area of a new cutting tool will also resulting in high initial wear rate. Hence, there will be a sudden spike at

the initial of the cutting processes until it gradually decreases, which means the metal-cutting processes approaching the steady wear state [3].

In the steady wear region, the wear rate increases linearly. Relatively constant wear rate is observed, where heat exchange rate is steady, and the cutting force is steady, which leads to a linear smooth line on the graph until it reaches a sudden spike, which indicates the metal-cutting processes approaching the severe wear region [3].

In the severe wear region, cutting force increase rapidly, and it is considered that the tool is unable to cut anymore, and the tool life already reaches its limit, resulting rapid temperature increment [3].

Previous studies had associate the tool wear generation with the cutting parameters in one cutting operations such as cutting speed v_c and feed rate f directly. There are two types of

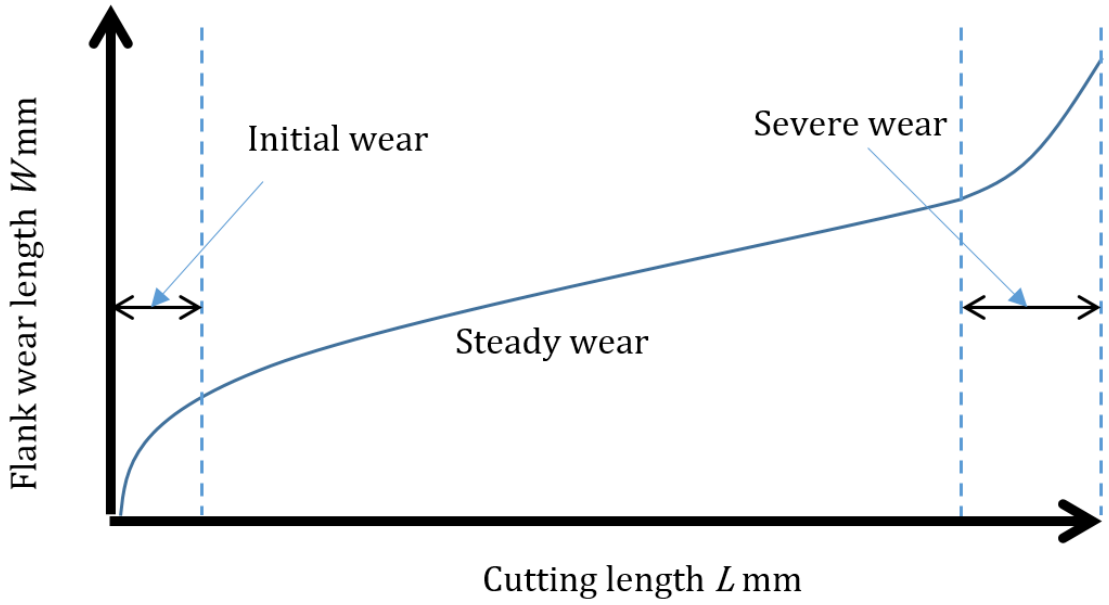

Fig 2.11: Typical Stages of Tool Wear in Cutting

wear models are available to express tool wear phenomenon, as shown in the following [38]:

a) Tool life models

Tool life models defines the relationship between cutting parameters and tool life, as shown in **Eq. (2.40)** [38] (v_c: cutting speed, L: tool life, C_1: constant). Taylor's tool life model appear frequently for variety of cutting conditions. Nowadays, updated tool life models is in demand due to rapid advancement of machining technologies and invention of new materials such as laser sintered in industry, where a lot of work needs to be done to gain more information about the tool life model for any specific cutting process.

$$v_c L^n = C_1 \tag{2.40}$$

b) Tool wear-rate models

The tool wear rate model defines the rate of local volume loss per unit area per unit time on the contact zone of rake or flank face of the tool. There are two main tool wear rate models being commonly utilized, Takeyama-Murata's wear model and Usui's wear model.

The Takeyama & Murata's wear model, as shown in **Eq. (2.41)**, considers the abrasive wear component and diffusive wear component of the cutting tool. Abrasive wear is highly affected by the cutting condition, while diffusive wear is related to cutting tool temperature [30] (dW/dt = wear rate, E: process activation energy, R: Universal gas constant, T: Cutting temperature).

$$\frac{dW}{dt} = G(v_c, f) + De^{-\frac{E}{RT}} \tag{2.41}$$

Meanwhile, the Usui's wear model, as shown in **Eq. (2.42)**, takes chip sliding velocity v_t, normal pressure N on the tool rake face, and cutting tool temperature T, which can be estimated through FEM or integrating analytical method with FDM [38].

$$\frac{dW}{dt} = A\sigma_n v_t e^{-\frac{B}{T}} \tag{2.42}$$

2.5 Numerical Formulation

There are many studies available in FEM evaluating the workpiece, cutting tool interaction using different finite-element formulations. Many of the formulations are applied in conjunction with each other to model various conditions of the material removal process. High precision in predicting and estimating the cutting process is one of the objectives. These formulations are Lagrangian/updated Lagrangian formulation, Eulerian and Arbitrary Lagrangian Eulerian [38-47], and explained as following:

a) Lagrangian formulation / Updated Lagrangian formulation

Lagrangian formulation is generally utilized in solving the mechanical's problems, where FE mesh element is made up by elements that covering the entire area of the body that is going to be analyzed and deformed as the workpiece material deformed during the simulation. The Lagrangian model is used to estimate the chip geometry from the beginning until the simulation reaches a steady state. The chip separation criteria must be provided in this model [43, 47].

The updated Lagrangian formulation is almost similar to the conventional Lagrangian formulations, but updated Lagrangian formulation is capable of starting the formulation at a given time, compared to the Lagrangian model, where it must begin at initial time zero [43].

b) Eulerian formulation

The Eulerian formulation was utilized for the steady-state condition, where the shape of the chip is known or modeled beforehand. The Eulerian formulation is preferable in fluid-flow problems where the mesh elements are fixed in a controlled volume. Constant tool-chip contact length l_c and chip thickness t_c are taken into consideration when Eulerian formulation is utilized [45-46].

c) Arbitrary Lagrangian Eulerian (ALE) Formulation

The ALE formulation is the combination of Lagrangian and Eulerian formulation. Where, material displacement in ALE formulation is solved by integration of Lagrangian and Eulerian step [21]. The ALE formulation is derived from two velocities, the material and the grid point. The model established mapping between velocities through time derivations. The Lagrangian formulation estimates the sum of mesh deformation to reduce the errors from mesh distortion, while the Eulerian formulation solves the relative displacement of the mesh, which is influenced by the deformation [21]. The Lagrangian formulation is utilized to predict the events of cutting from the beginning to the steady state, where the deformed chip and the temperature in the cutting zone are calculated. Once the steady state chip is archived, the Eulerian formulation will calculate the temperature within the tool [21].

2.6 Conclusion and summary

This chapter explains the fundamental understanding on mechanics, parameters, models, and formulations involved in the metal-cutting process, and previous researchers tried to determine the effective way to understand and to gain higher precision of cutting results with the application of FEM. Cutting process is considered as complex, whereas involvement a number of parameters. Several FEM models were proposed, from simplified 2D orthogonal cutting model to complex 3D cutting model in FEM. It is an invaluable effort, in improving the knowledge and understanding, as well as increasing the efficiency in production, manufacturing systems and industries.

References

[1] Vaughn, R. L. (1966). Modern Metals Machining Technology. *Journal of Engineering for Industry*, *88*(1), 65.

[2] Groover, M. P. (1996). *Fundamentals of modern manufacturing: materials, processes, and systems*. Upper Saddle River, NJ: Prentice Hall.

[3] Kalpakjian, S. (2001). *Manufacturing engineering and technology*. Upper Saddle River, NJ: Prentice Hall.

[4] Astakhov, V. P. (2005). On the inadequacy of the single-shear plane model of chip formation. *International Journal of Mechanical Sciences*, *47*(11), 1649-1672.

[5] Devries, W. R. (1992). Analysis of Material Removal Processes. *Springer-Verlag Publications*, New York.

[6] Oxley, P. (1961). A strain-hardening solution for the "shear angle" in orthogonal metal cutting. *International Journal of Mechanical Sciences*,*3*(1-2), 68-79

[7] Oxley, P. L., & Shaw, M. C. (1990). Mechanics of Machining: An Analytical Approach to Assessing Machinability. *Journal of Applied Mechanics*, *57*(1), 253.

[8] Palmer, W.B. and Oxley, P.L.B. (1959). Mechanics of Orthogonal Machining. *Proc. Inst. Mech. Engrs*. (173), 623.

[9] Sutter, G. (2005). Chip geometries during high-speed machining for orthogonal cutting conditions. *International Journal of Machine Tools and Manufacture*, *45*(6), 719-726.

[10] Merchant, M. E. (1945). Mechanics of the Metal Cutting Process. II. Plasticity Conditions in Orthogonal Cutting. *Journal of Applied Physics*,*16*(6), 318

[11] Okushima, K., & Hitomi, K. (1961). An Analysis of the Mechanism of Orthogonal Cutting and Its Application to Discontinuous Chip Formation. *Journal of Engineering for Industry, 83*(4), 545.

[12] Shirakashi, T., Maekawa, K. and Usui, E (1983), Flow stress of low carbon steel at high temperature and strain Rate (Part 1) – Propriety of incremental strain method in impact compression test with rapid heating and cooling systems, *Bulletin of the Japan Society of Precision Engineering 17 (3)*, 161-166.

[13] MacGregor, C. W., and Fisher, J. C., (1946). Tension tests at constant true strain-rates, *Journal of Applied Mechanics*, 12, TRANS. ASME, 67.

[14] Zhang, Y., Outeiro, J., & Mabrouki, T. (2015). On the Selection of Johnson-cook Constitutive Model Parameters for Ti-6Al-4V Using Three Types of Numerical Models of Orthogonal Cutting. *Procedia CIRP, 31*, 112-117.

[15] Choi, M. (1995). A study of shear angle relationships in shearing process on the shear plane and the rake face in orthogonal cutting. *KSME Journal*, *9*(3), 385-391.

[16] Filice, L., Micari, F., Rizzuti, S., & Umbrello, D. (2007). A critical analysis on the friction modelling in orthogonal machining. *International Journal of Machine Tools and Manufacture, 47*(3-4), 709-714.

[17] Filice, L., Micari, F., Rizzuti, S., & Umbrello, D. (2008). Dependence of Machining Simulation Effectiveness on Material and Friction Modelling. *Machining Science and Technology*, *12*(3).

[18] Iqbal, S., Mativenga, P., & Sheikh, M. (2008). Contact length prediction: mathematical models and effect of friction schemes on FEM simulation for conventional to HSM of AISI 1045 steel. *International Journal of Machining and Machinability of Materials, 3*(1/2), 18.

[19] Özel, T., & Altan, T. (2000). Process simulation using finite element method — prediction of cutting forces, tool stresses and temperatures in high-speed flat end milling. *International Journal of Machine Tools and Manufacture*, *40*(5), 713-738.

[20] Özel, T. (2006). The influence of friction models on finite element simulations of machining. *International Journal of Machine Tools and Manufacture*, *46*(5), 518-530.

[21] Özel, T., & Zeren, E. (2006). Finite element modeling the influence of edge roundness on the stress and temperature fields induced by high-speed machining. *The International Journal of Advanced Manufacturing Technology*, *35*(3-4), 255-267.

[22] Smith, J. M., & C., V. N. (1987). *Introduction to chemical engineering thermodynamics*. New York: McGraw-Hill.

[23] Abukhshim, N., Mativenga, P., & Sheikh, M. (2006). Heat generation and temperature prediction in metal cutting: A review and implications for high speed machining. *International Journal of Machine Tools and Manufacture*, *46*(7-8), 782-800.

[24] Burmeister, L. C. (1983). *Convective heat transfer*. New York: Wiley.

[25] Mahfudz al Huda (1999). Investigation of cutting tool temperature in turning, Phd Thesis, Kanazawa University

[26] Cengel, Y. A. (2012). *Thermodynamics: an engineering approach*. New York: Mcgraw-Hill.

[27] Yen, Y., Söhner, J., Lilly, B., & Altan, T. (2004). Estimation of tool wear in orthogonal cutting using the finite element analysis. *Journal of Materials Processing Technology*, *146*(1), 82-91.

[28] Calatoru, V., Balazinski, M., Mayer, J., Paris, H., & L'Espérance, G. (2008). Diffusion wear mechanism during high-speed machining of 7475-T7351 aluminum alloy with carbide end mills. *Wear*, *265*(11-12), 1793-1800.

[29] Hu, J., & Chou, Y. K. (2007). Characterizations of cutting tool flank wear-land contact. *Wear*, *263*(7-12), 1454-1458.

[30] Takeyama H., Murata T. (1963). Basic investigations on tool wear, Trans. *ASME J. Eng. Ind.* (*85,)* 33–38

[31] Venuvinod, P., Lau, W., & Rubenstein, C. (1983). The role of discrete contact at the flankwear land in determining cutting tool temperature in orthogonal cutting. *International Journal of Machine Tool Design and Research*, *23*(4), 245-261.

[32] Wright, P. K., & Bagchi, A. (1981). Wear mechanisms that dominate tool-life in machining. *Journal of Applied Metalworking*, *1*(4), 15-23.

[33] Xie, L. (2004). *Estimation of two-dimension tool wear based on finite element method*. Karlsruhe: Wbk, Inst. für Produktionstechnik.

[34] Xie, L., Schmidt, J., Schmidt, C., & Biesinger, F. (2005). 2D FEM estimate of tool wear in turning operation. *Wear*, *258*(10), 1479-1490.

[35] Zhang, C., Liu, X., Fang, J., & Zhou, L. (2010). A new tool wear estimation method based on shape mapping in the milling process. *The International Journal of Advanced Manufacturing Technology*, *53*(1-4), 121-130.

[36] Filice, L., Micari, F., Settineri, L., & Umbrello, D. (2007). Wear modelling in mild steel orthogonal cutting when using uncoated carbide tools. *Wear*, *262*(5-6), 545-554.

[37] Attanasio, A., Ceretti, E., Fiorentino, A., Cappellini, C., & Giardini, C. (2010). Investigation and FEM-based simulation of tool wear in turning operations with uncoated carbide tools. *Wear*, *269*(5-6), 344-350.

[38] Yen, Y., Jain, A., & Altan, T. (2004). A finite element analysis of orthogonal machining using different tool edge geometries. *Journal of Materials Processing Technology*, *146*(1), 72-81.

[39] Gupta, K. K., & Meek, J. L. (1996). A Brief History of the Beginning of the Finite Element Method. *International Journal for Numerical Methods in Engineering, 39*(22), 3761-3774.

[40] Adibi-Sedeh, A. H., Madhavan, V., & Bahr, B. (2003). Extension of Oxley's Analysis of Machining to Use Different Material Models. *Journal of Manufacturing Science and Engineering, 125*(4), 656.

[41] Cao, Y., Chen, H., & Zhao, H. X. (2011). Turning Process Modeling and Cutting Force Investigation Based on Finite Element Analysis and Cutting Experiments. *Advanced Materials Research, 314-316*, 900-903.

[42] Davim, J., & Maranhão, C. (2009). A study of plastic strain and plastic strain rate in machining of steel AISI 1045 using FEM analysis. *Materials & Design, 30*(1), 160-165.

[43] Shet, C., & Deng, X. (2000). Finite element analysis of the orthogonal metal cutting process. *Journal of Materials Processing Technology, 105*(1-2), 95-109.

[44] Strenkowski, J. S., & Carroll, J. T. (1985). A Finite Element Model of Orthogonal Metal Cutting. *Journal of Engineering for Industry, 107*(4), 349.

[45] Carroll, J. T., & Strenkowski, J. S. (1988). Finite element models of orthogonal cutting with application to single point diamond turning. *International Journal of Mechanical Sciences, 30*(12), 899-920.

[46] Strenkowski, J. S., & Athavale, S. M. (1997). A Partially Constrained Eulerian Orthogonal Cutting Model for Chip Control Tools. *Journal of Manufacturing Science and Engineering, 119*(4B), 681.

[47] Zhang, L. (1999). On the separation criteria in the simulation of orthogonal metal cutting using the finite element method. *Journal of Materials Processing Technology, 89-90*, 273-278.

CHAPTER 3

EVALUATION ON THE INFLUENCE OF MINIMUM QUANTITY LUBRICATION DURING CUTTING PROCESS BY FINITE ELEMENT METHOD – (LUBRICATION EFFECT)

3.1 Introduction

Conventional wet cutting method has tended to shift to dry or semi-dry cutting due to a large amount of cutting fluid leads to the increment of power consumption and processing cost. In addition, the cutting fluid by-product obtained from the process pollutes the working environment that affected the health of the machine operators. Therefore, the development of Minimum Quantity Lubrication (MQL) machining is emphasized in solving and containing these matters [1].

In MQL cutting, a very small amount of cutting fluid is turned into fine oil mist, and supplied to the cutting point as semi-dry processing, expecting the promotion of the cutting performance of tools in terms of tool integrity, product finish and power consumption. Approximately only 1/10000 fluid volume of that in the ordinary wet cutting is consumed during MQL, which leads to cleaning the working environment and reduction of waste liquid

that lessen the overall processing cost [1]. Several researchers have been done in identifying the effect of Minimum Quantity Lubrication (MQL) during cutting process [1]. It is proven that MQL method can reduce the cutting force and cutting temperature, which leads to improvement of the surface finish and increment of tool life. However, it is still yet hard to be understood on how lubrication works during the cutting process because the frictional contact mechanism between cutting tool, and workpiece/chip is considered as complex [1].

Previous researchers have done several studies in order to identify the parameters involved during one cutting process and their relationships between cutting performances [2-7]. The finite element method (FEM) is an important research tool in improving manufacturing and industrial capability, especially in mold making. However, it is considered difficult to design a perfect simulation model as the actual cutting process because of its complexity.

This chapter aims to design appropriate Finite-Element Method (FEM) models to analyze the cutting parameters related to the effect of Minimum Quantity Lubrication and validated by equivalent experimental procedure. In the present study, parameters such as cutting force F, frictional coefficient μ, chip thickness t_c, tool-chip contact length l_c are observed under various cutting conditions to study the influence of MQL in terms of lubrication during one cutting process.

3.2 Finite element method (FEM) models

In recent years, application of finite-element method (FEM) has become renowned in simulating high speed machining. Finite-element method (FEM) is a numerical method that

separates a problem into smaller regions. It is proven useful in saving the research cost and time. In addition, it is capable of forecasting effects of cutting parameter such as cutting force and tool edge temperature [8][19]. In machining, estimated cutting forces and temperature, are applied in tool wear studies to obtain the optimum cutting parameters such as cutting speed, cutting depth, and others. With these conditions, cutting tool is optimized for its productivity, less experimental trial and expensive costs on tooling can be reduced [19].

FEM models in machining processes have been widely developed by many researchers. The simplest model for these analyses is the 2D orthogonal cutting. In this model, cutting-edge moves perpendicular to the relative motion between cutting tool and workpiece to remove the unnecessary material from the workpiece with a constant uncut chip thickness [23-25].

3.2.1 Parameters influence on cutting process

Fig. 3.1 shows the overview of the main process in estimating the influence of MQL on cutting process by FEM. The process involves FEM model to estimate chip thickness to resemble the lubrication phenomenon of MQL. After the reliable chip thickness had been estimated, MQL influenced cutting process simulation will be executed with a practical FEM model. The accuracy of material deformation estimation is important, whereas the mechanical behavior of material is significantly related to the thermal behavior in the cutting process. The FEM model from the process in this chapter will later be applied in the following chapter, whereas the temperature generation during cutting process and cooling phenomenon of MQL will be studied, and new MQL method will be surveyed.

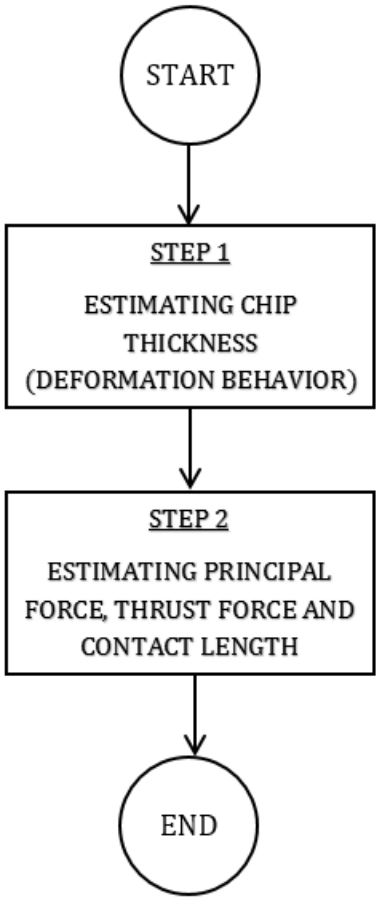

Fig. 3.1 Overview of main process in evaluating influence of MQL by FEM

In this study, FEM simulation models in orthogonal cutting of mild steel, JIS-S45C is designed on the application software DEFORM™-3D, whereby the workpiece and cutting tool geometries are designed and simplified by the application of Computer-Aided Design (CAD), as shown in **Fig. 3.2**. DEFORM™ is a well-known commercially available FEM tool, with one of the best in graphical-user-interface (GUI), specialized in simulating metal forming.

Additionally, the FEM tool employs Lagrangian formulation, which is suitable for large deformation, as well as capable of generating specific mesh density for severe deformation zone on the workpiece. In the simulation, the FEM cutting tool is designed to resemble the actual orthogonal cutting-tool geometry at the cutting point, with 0° rake angle and 10° clearance angle. The effect of tool edge radius is neglected, as the cutting depth is

more than 10 times larger than the tool edge radius in the equivalent experimental procedure.

In the analysis, workpiece is designed to deform plastically, while the cutting tool is designed as rigid where elastic deformation of cutting tool is neglected due to the large ratio of Young Modulus, *E* between the tool and workpiece materials. In the analysis, denser mesh is designed at the tool-workpiece contact where significant plastic deformation occurred. Adaptive meshing, ability to re-mesh whenever tool and workpiece's mesh overlapping occurred, is applied. The initial maximum number of elements in the tool is 10,000 elements, and 50,000 elements for the workpiece. **Fig. 3.3** shows example of mesh structure in FEM model. All elements are constraints from distorting on Z-axis to limit the workpiece deformation in two-dimensional directions (X and Y-axes) only. The cutting condition and material properties for FEM application are shown in **Table 3.1** and **Table 3.2,** respectively.

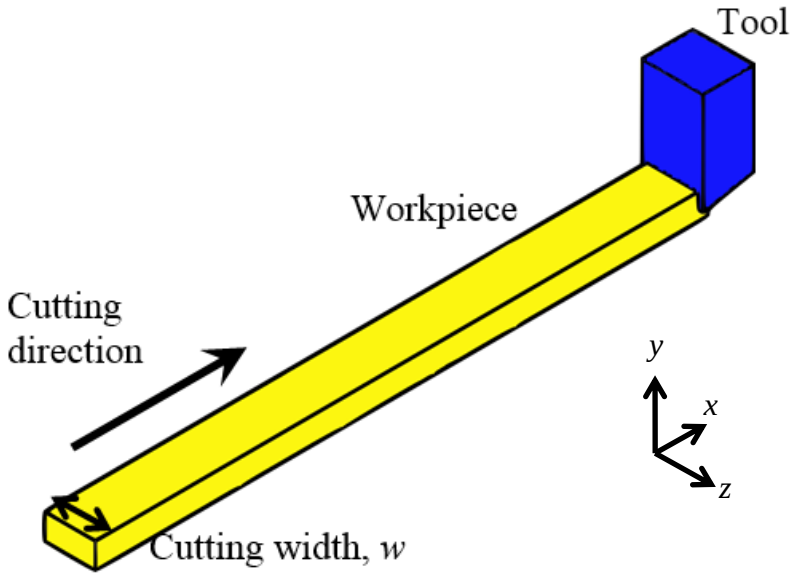

Fig. 3.2 Simplified geometry of orthogonal cutting process by CAD program

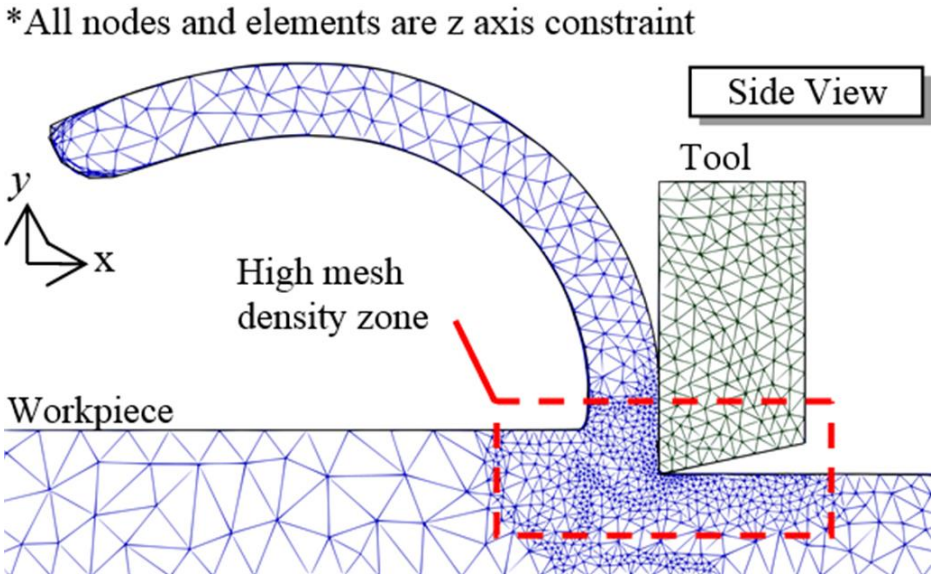

Fig. 3.3 Mesh structure in FEM model

Table 3.1 Cutting condition for FEM application

Cutting Tool	TiCN-coated Cermet
Workpiece	JIS-S45C
Cutting width w [mm]	1.0
Depth-of-cut a [mm]	0.3
Cutting speed v_c [m/min]	50 ~ 200

Table 3.2 Properties of workpiece materials for FEM application

Material	JIS-S45C
Young modulus E [GPa]	212
Density ρ [kg/m^3]	7850
Vickers hardness HV0.3	1.96

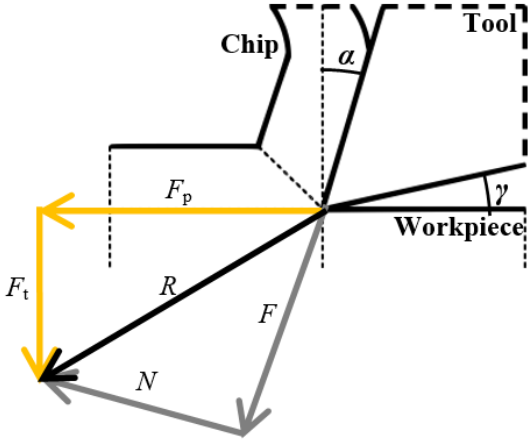

Fig. 3.4 (a) Typical simplified model of orthogonal cutting

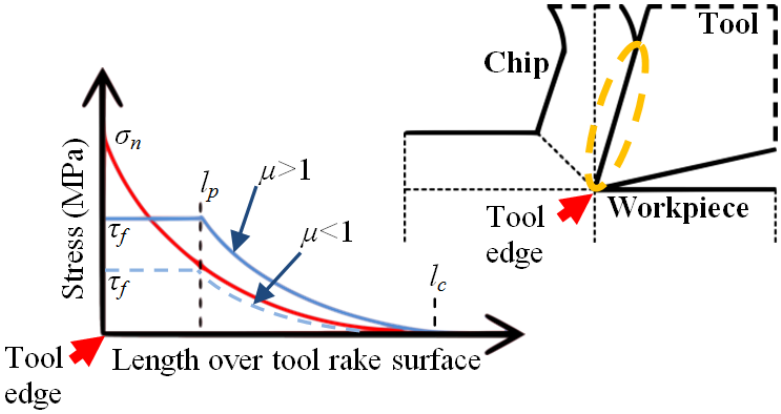

Fig. 3.4 (b) Zorev's stress distribution curves on tool rake.

In designing the FEM models that resemble the actual cutting behavior, previous researchers applied average frictional coefficients μ_{avg}, based on Coulomb's law of friction, calculated by **Eq. (3.1)**, as shown in **Fig. 3.4(a)**. It is assumed that, the friction coefficient μ_{avg} has a direct relationship to the actual friction phenomenon on the contact zone during the cutting process [14].

$$\mu_{\text{avg}} = \frac{F}{N} = \left(\frac{F_{\text{t}} + F_p \tan\alpha}{F_p - F_{\text{t}} \tan\alpha}\right) \tag{3.1}$$

Additionally, earlier researchers justified that the normal stress, σ_n along the rake face is not constant, referring to **Fig. 3.4 (b)**, while frictional stress τ_f is distinguished into two zones; sticking zone and sliding zone; as shown in **Eq. (3.2)**. Here, *k* is the shear flow stress of

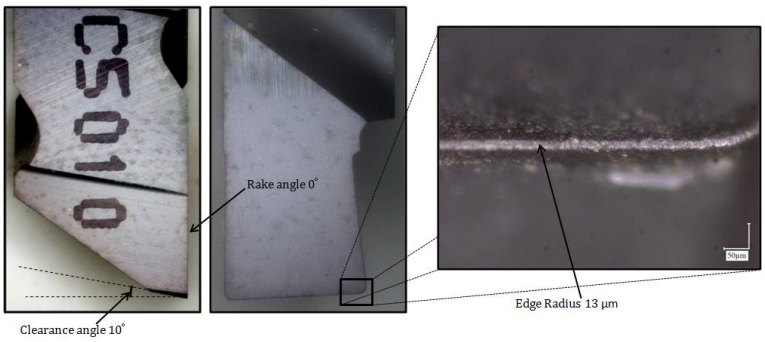

Fig. 3.5 Zero rake angle orthogonal cutting tool

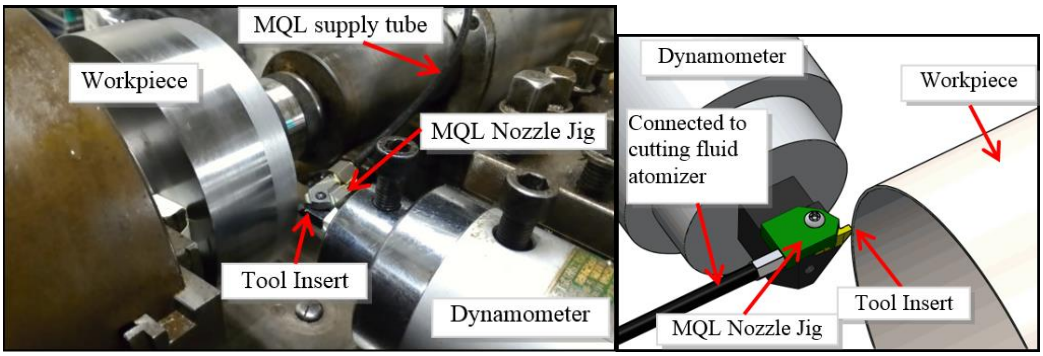

Fig. 3.6 Orthogonal cutting setup

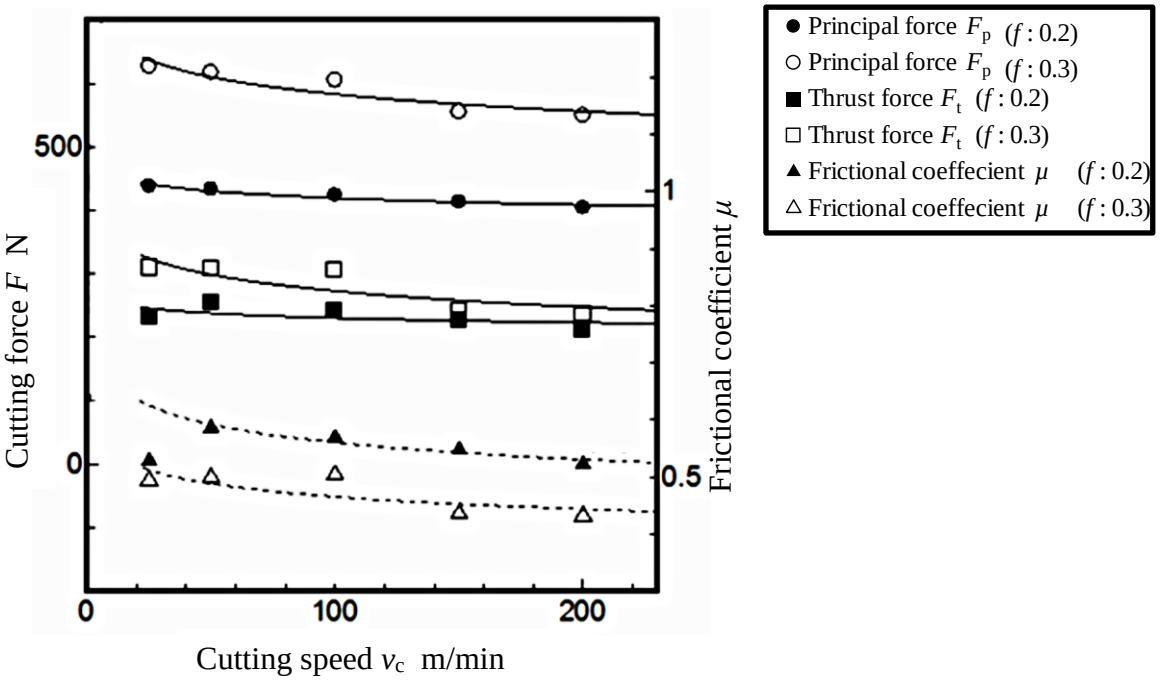

Fig. 3.7 Relationship between cutting speed v_c and cutting force F, for various feed rate f

the local work material [15-16].

$$\begin{cases} \mu\sigma_n(x) \geq k & 0 \leq x \leq l_p, \tau_f(x) = k \\ \mu\sigma_n(x) \leq \tau_p l_p \leq x \leq l_c, & \tau_f(x) = \mu\sigma_n(x) \end{cases} \quad (3.2)$$

3.2.2 Orthogonal cutting test

In order to validate the effective MQL parameters, a pseudo-orthogonal cutting test is carried out with 0° rake angle cutting tool. The orthogonal cutting workpiece is specially designed with cutting width w = 1 mm, as shown in **Figs. 3.5** and **3.6**. Here, the orthogonal cutting tool that has no groove or chip breaker is chosen to reduce geometry complexity.

Fig. 3.7 shows the relationship between cutting speed v_c and cutting force F for orthogonal cutting in dry condition. It is observed that, cutting force F for feed rate f 0.3

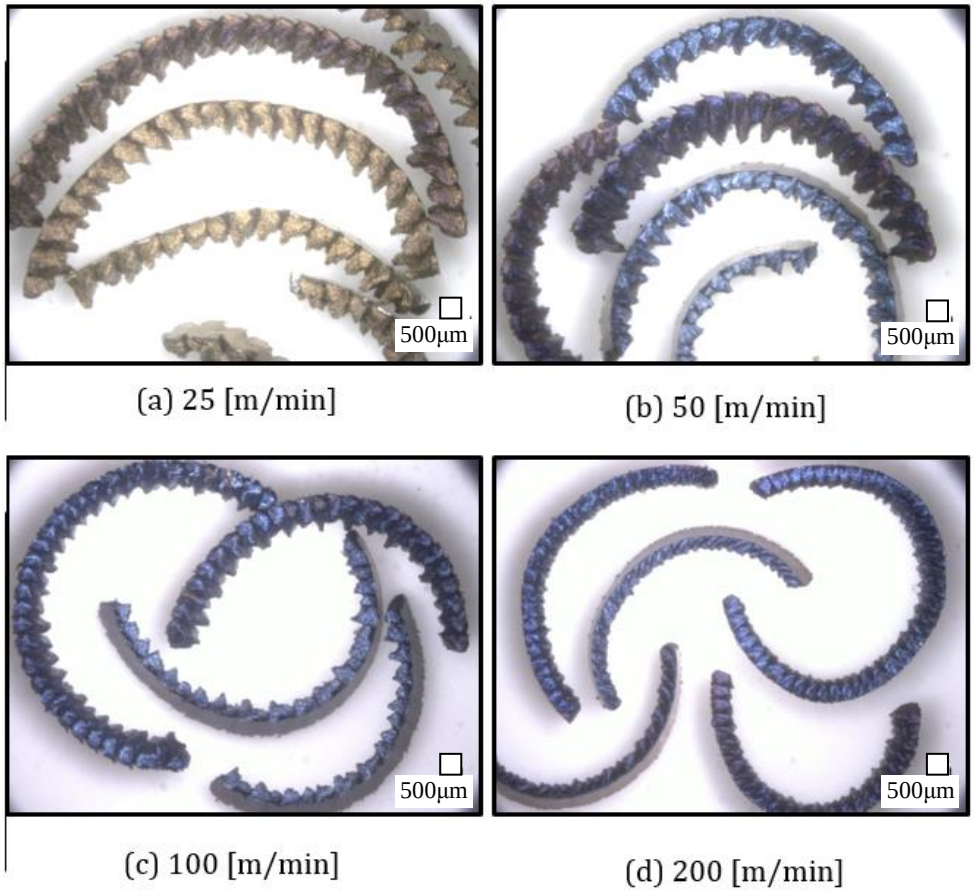

Fig. 3.8 Chip morphology for orthogonal cutting S45C with feed 0.3 mm/rev

mm/rev is higher than that for feed rate *f* 0.2 mm/rev, due to larger cutting load.

Additionally, it is observed that, cutting force F decreases with the increasing of cutting speed v_c. Cutting chip resulted from each cutting condition is observed and chip thickness t_c is measured, as shown in **Fig. 3.8**, to ensure the chip formed in orthogonal shape. It is observed that, the size of saw-tooth shape of the chip is getting smaller as the cutting speed increases. Chip thickness t_c is measured with a micrometer for each cutting speed v_c condition and cutting ratio r is calculated, as shown in **Fig. 3.9**. Frictional coefficient μ is then being estimated through **Eqs. (3.3)** and **(3.4)**, according to Merchant Force Diagram and Minimum Energy Principal, and the result is plot in **Fig. 3.9**.

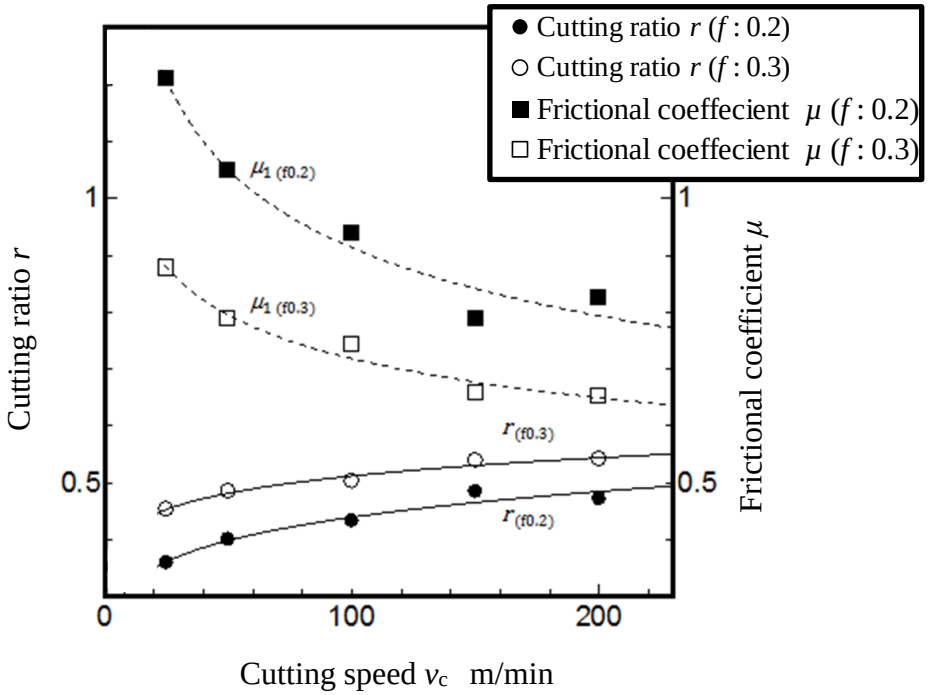

Fig. 3.9 Relationship between cutting speed cutting speed v_c and cutting force F, for various feed rate f

$$\begin{cases} \dfrac{t}{t_c} = r = \tan\theta \\ \beta_1 = \dfrac{\pi}{2} - 2\theta \end{cases} \tag{3.3}$$

$$\mu_1 = \tan\beta_1 \tag{3.4}$$

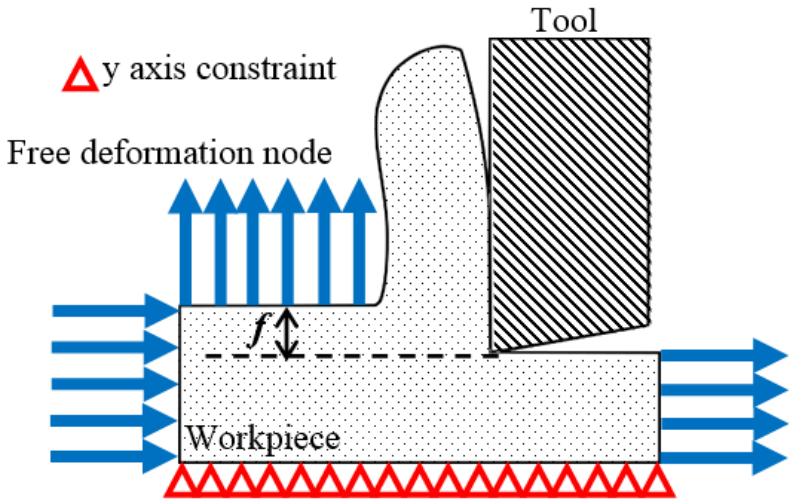

Fig. 3.10 Simplified FEM model (Model A)

It is observed that, cutting ratio r increases and friction coefficient μ decreases as cutting speed v_c increases. However, the validity of estimated frictional coefficients μ is questionable, as the frictional coefficient μ for the low cutting speed $v_c < 100$ m/min and low feed rate $f < 0.3$ mm/rev is larger than 1.0 ($\mu > 1.0$). Thus, Minimum Energy Principal is assumed to be irrational, and it is decided that average friction coefficient μ_{avg} obtained by **Eq. (3.1)**, is applied as the MQL friction coefficient μ_{MQL} for the study.

3.2.3 Effective FEM models

In modeling an accurate material deformation, several FEM models are proposed, where experimentally estimated friction coefficient μ_{MQL} is utilized into each model for each cutting condition.

$$\mu_{\text{cal}} = \mu_{\text{MQL}} \frac{F_{p(\text{exp})} - F_{p(\mu_n=0)}}{F_{p(\mu_n=\mu_{\text{exp}})} - F_{p(\mu_n=0)}} \tag{3.5}$$

(a) Simplified FEM model (Model A)

The *Simplified FEM model (Model A)* is designed, as shown in **Fig. 3.10**, where the MQL friction coefficient μ_{MQL} estimated by **Eq. (3.1),** will be input into the model [15-19]. In this model, it is assumed that constant friction occurred on the whole tool rake face, regardless the length of sticking and sliding zones. The tool-chip contact length l_c will be estimated by the FEM itself. In the meantime, *Simplified FEM model (Model A)* with μ = 0 are executed along with the MQL friction coefficient μ_{MQL} FEM model. The friction coefficients are chosen to reduce arbitrary speculation. The output characteristic will be analyzed and if a necessary, friction coefficient μ_{cal} is calculated by **Eq. (3.5)**, and the simulation will be repeated with the similar FEM model.

(b) Chip thickness constraint FEM model (Model B)

The *Chip thickness constraint FEM model (Model B)* is designed with additional Eulerian deformation constraint to optimize chip thickness formation (**Fig. 3.11**) [20-21]. In this model, arbitrary Lagrangian-Eulerian formulation is applied, where the gap size between the deformation boundary and the tool is equivalent to the measured/estimated value of the chip thickness, t_c for each cutting speed. Simulation is executed with the exact MQL friction coefficient μ_{MQL} to study the relationship of the parameters during the cutting process.

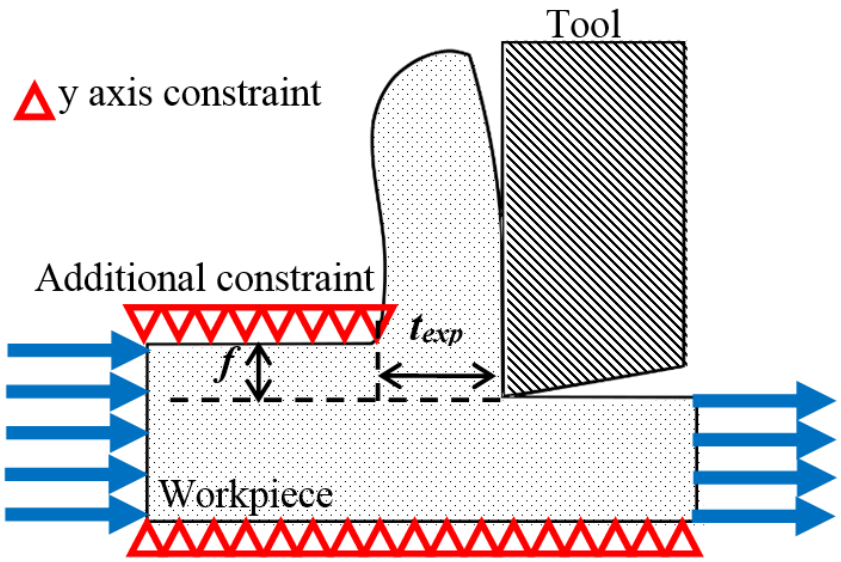

Fig. 3.11 MQL estimation FEM model (Model B)

3.3 Minimum quantity lubrication (MQL) for orthogonal cutting

In the study, the effect of minimum quantity lubrication (MQL) onto cutting performance is analyzed. Until now, application of MQL in orthogonal cutting is not well discussed and done, due to the limited application in the industry. However, in studying the effect of MQL during cutting process, orthogonal cutting is suggested, whereas the complex geometry of the conventional cutting tool is neglected, and the effect of MQL can be focused on. In the study, two MQL supplying methods are designed; external and internal MQL methods. Effectiveness of both methods is compared, and the method with the highest efficiency will be chosen as the main MQL supplying method throughout the study.

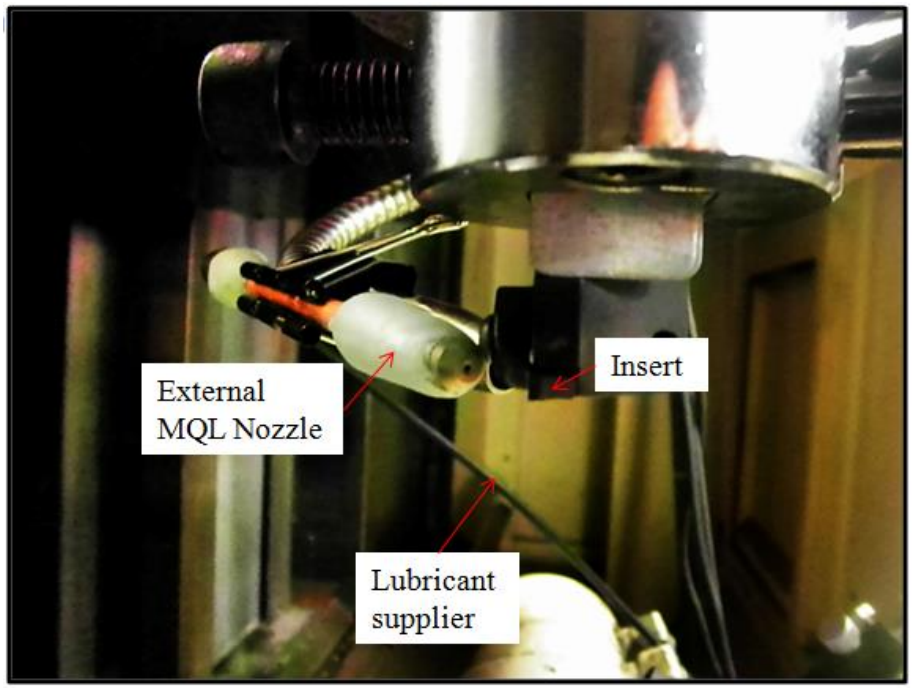

Fig. 3.14 External MQL supplying method

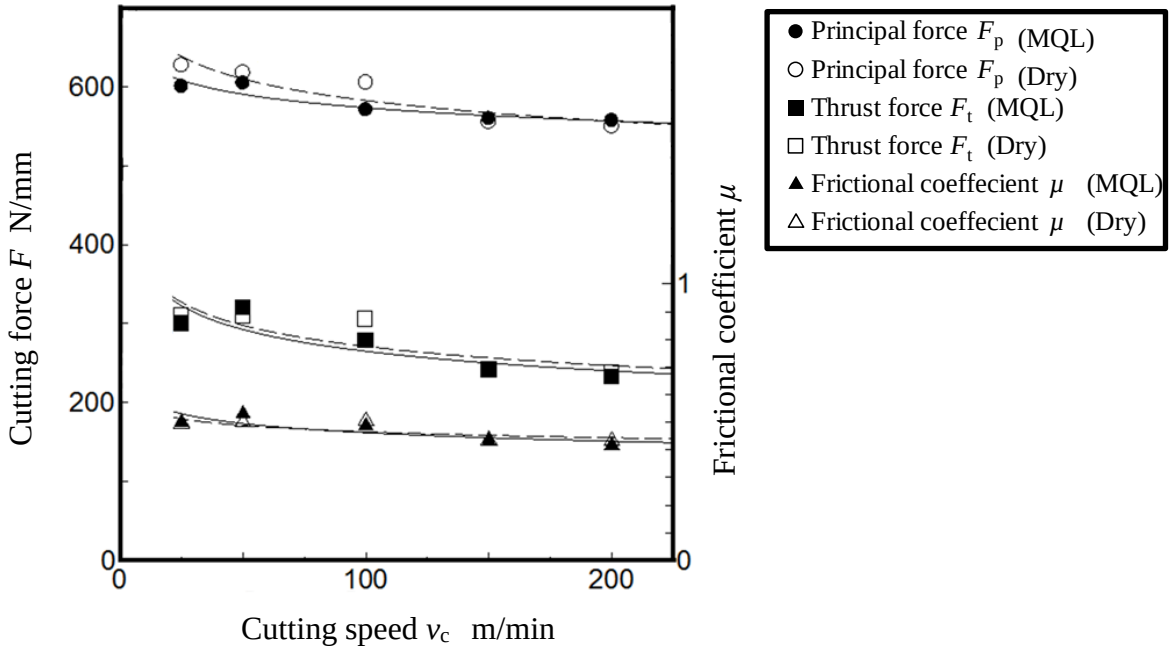

Fig. 3.15 Cutting speed v_c-cutting force F relationship comparison between dry cutting and external MQL supplying method

Table 3.3 Characteristic of cutting fluid for external MQL supplying method

Oil Type	Vegetable oil (LB-1)
Viscosity [mm^2/s]	S45C
Oil Contents [%]	99
Supplied Rate [mL/h]	18
Supplied Zone	Rake face

3.3.1 External MQL supplying method

In the beginning stage of the MQL application during the orthogonal cutting, an external type of MQL nozzle is designed to supply oil mist to the cutting point, as shown in **Fig. 3.14**. The experiment is done with the similar cutting conditions for dry cutting process to analyze its effectiveness, and the result is shown in **Fig. 3.15**. The characteristics of cutting fluid supplied are shown in **Table 3.3**. It is observed that, cutting force *F* generated from the cutting process with the external MQL method shows slight decrement compared to cutting process with dry, whereas the efficiency is about 5%. It is assumed that this efficiency is low as it is assumed that MQL mist is unable to penetrate the contact area between tools and chip effectively. It is also assumed that, distance from the nozzle outlet to the cutting the zone must be taken into consideration in designing the MQL supplying method. Due to this low efficiency, internal MQL nozzle supplying method is designed.

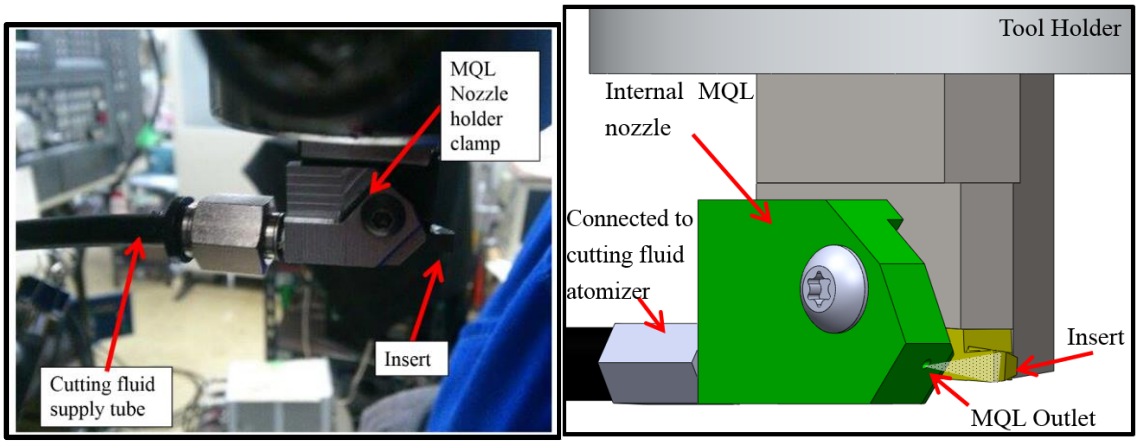

Fig. 3.16 Internal MQL supplying method

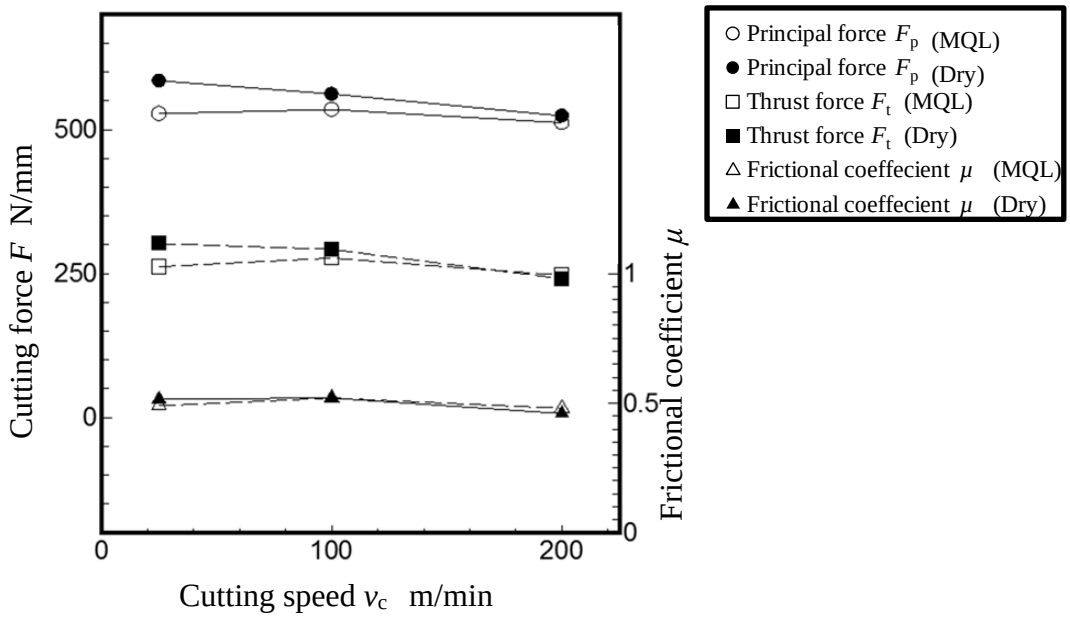

Fig. 3.17 Cutting speed v_c-cutting force F relationship comparison between dry cutting and internal MQL supplying method

3.3.2 Internal MQL supplying method

Internal MQL supplying method is proposed by redesigning an insert clamp to have MQL inlet and outlet capable of supplying oil mist to the cutting zone, as shown in **Fig. 3.16**. The MQL supplying method in orthogonal cutting is different compared with MQL supplying method in conventional one, whereas the MQL inlet and outlet are designed on the tool holder. Maximum tool-chip contact length l_c generated from cutting process in dry cutting is taken into consideration, and the position of the nozzle outlet from the contact zone is estimated. Cutting process is done with similar cutting condition to external MQL supplying method. The experimental results are shown in the **Fig. 3.17**, and effectiveness comparison is done.

It is observed that, the effectiveness of MQL increases up to 15% with the updated designed internal MQL supplying method. It is justified that, the nozzle positioning and the distance of the outlet from the cutting zone are important MQL nozzle characteristics in obtaining higher effectiveness MQL system.

From the finding, it is decided that, the internal MQL supplying method will be utilized throughout the study. There are two types of cutting fluid, Oil-A and Oil-B, which are utilized based on the variable composition between nontoxic vegetable oil and water. The composition of Oil-A is 99% vegetable oil and 1% water, while the composition of Oil-B is 30% vegetable oil and 70% water. Oil-A is supplied at 30 mL/h, while Oil-B is supplied 100 mL/h onto the tool rake face during the cutting process. It is to ensure equivalent lubrication property for both types of cutting fluid. Additionally, Oil-B has further coolant property. The characteristics of cutting fluid for internal MQL supplying method in the study are summarized in **Table 3.4**.

Table 3.4 Characteristic of cutting fluid for internal MQL supplying method

Oil Type	Vegetable oil
Viscosity [mm^2/s]	37
Oil Contents [%]	
Oil-A	99
Oil-B	30
Supplied Rate [mL/h]	
Oil-A	30
Oil-B	100
Oil Pressure [Mpa]	0.6

3.4 Experimental and FEM results and discussions

3.4.1 Influence of MQL onto cutting force, chip thickness and contact length behavior in orthogonal cutting

Fig. 3.18 shows the relationship between cutting speed v_c and cutting force F in various MQL methods, while **Fig. 3.19** shows the relations of cutting speed v_c, tool-chip contact length l_c and chip thickness t_c for Dry, Oil-A and Oil-B condition. It is observed that, the magnitude of principal F_p and thrust force F_t decrease as the cutting speed v_c increases in general. Similar trend is observed for tool-chip contact length l_c and chip thickness t_c, where both l_c and t_c decrease as the cutting speed v_c increases for dry and both MQL cutting conditions.

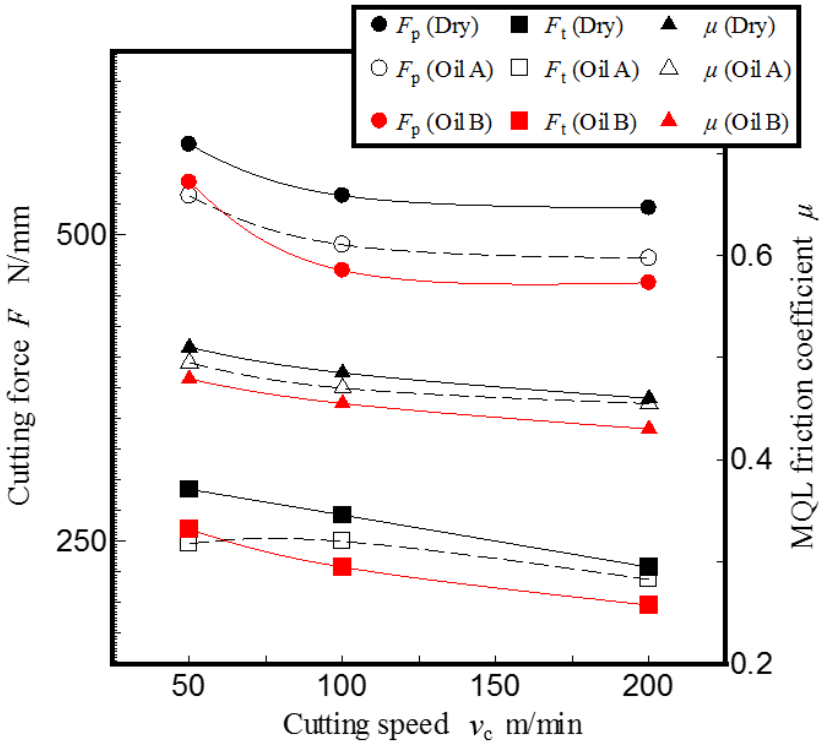

Fig. 3.18 Relationship between cutting speed v_c and cutting force F in various MQL methods

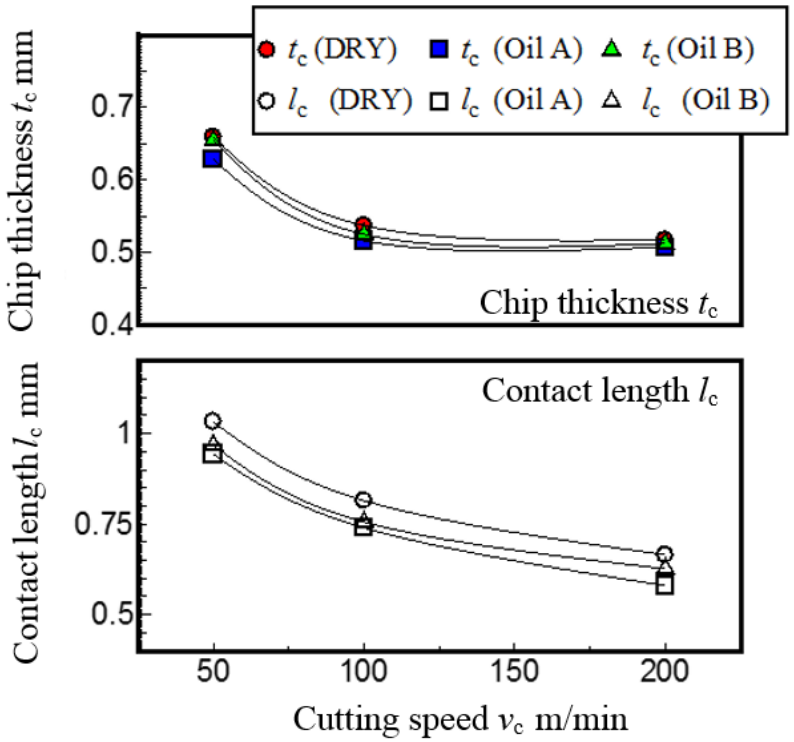

Fig. 3.19 Relationship between cutting speed v_c, chip thickness t_c and tool-chip contact length l_c in various MQL methods

It is understood that, the magnitude of cutting forces F have a direct relationship to the cutting load and the tool-chip contact characteristic, whereas lower magnitude of cutting forces F, size of contact length l_c and chip thickness t_c are observed during the application of MQL onto the cutting process. It is assumed that, the existence of MQL molecule on the tool-chip contact zones is capable of reducing the frictional stress, whereas the MQL molecule is assumed to act as a roller or spring like element.

3.4.2 Finite Element Method (FEM) model in material deformation analysis

(a) Simplified FEM model (Model-A)

MQL friction coefficient μ_{MQL} obtained from **Eq. (3.1)** is adopted into the *Simplified FEM model (Model A),* and its capability of imitating the cutting process is analyzed in terms of cutting force F, chip thickness t_c and tool-chip contact length l_c. It is observed that, the *Simplified FEM model (Model A)* is capable of estimating the cutting force F with a similar trend with experimental results. However, only thrust force F_t is estimated accurately, while principal force F_p is estimated with large error when validated with the experimental data **(Fig. 3.20).**

Simultaneously, it is also observed that, tool-chip contact length l_c is estimated with high accuracy, while chip thickness t_c is estimated with large error (**Fig. 3.21**). It is assumed that, there are possible relationship between the chip thickness t_c and the principal force F_p, as well as the tool-chip contact length l_c and the thrust force F_t.

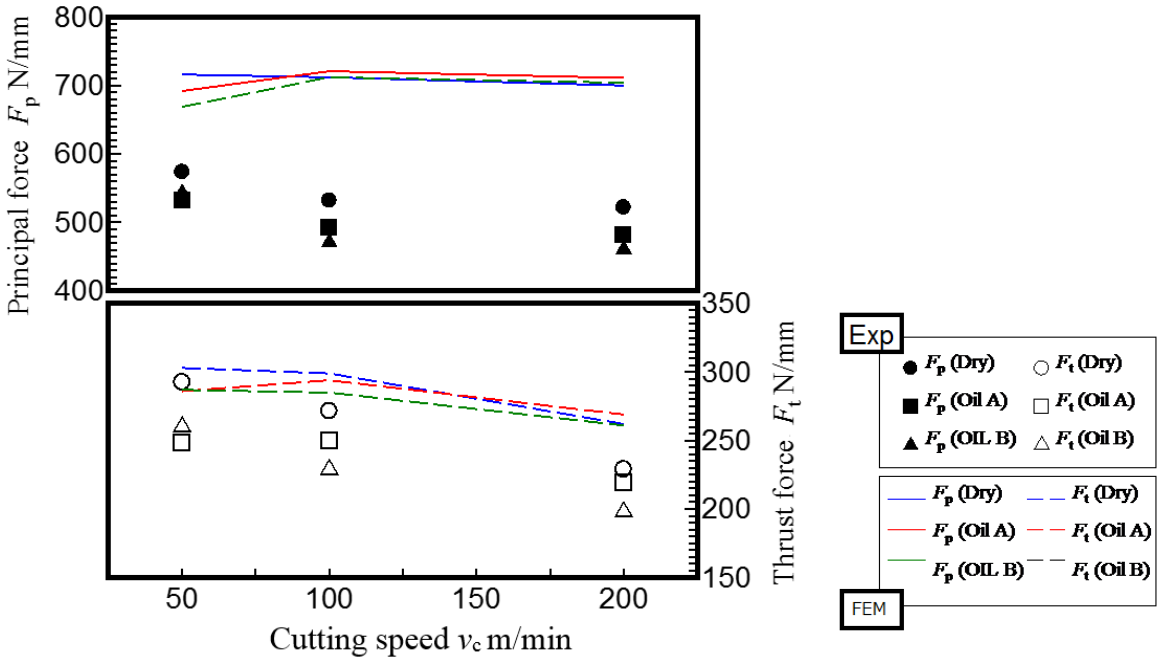

Fig. 3.20 Relationship between cutting speed and principal force and thrust force estimated by Simplified FEM Model A

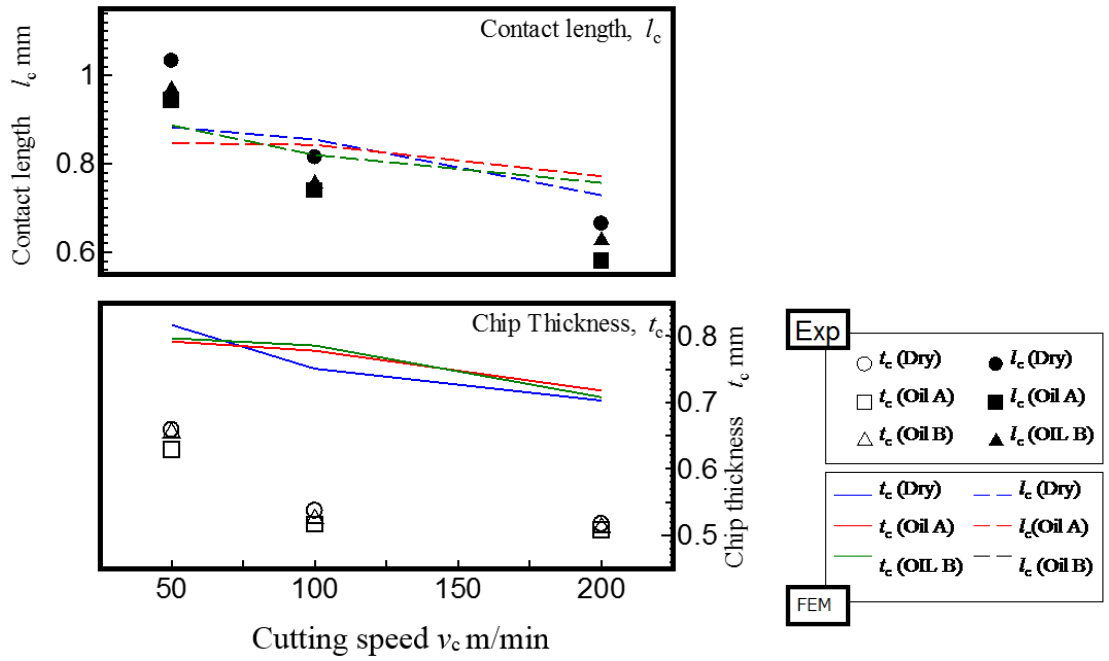

Fig. 3.21 Relationship between cutting speed and contact length and chip thickness estimated by Simplified FEM Model A

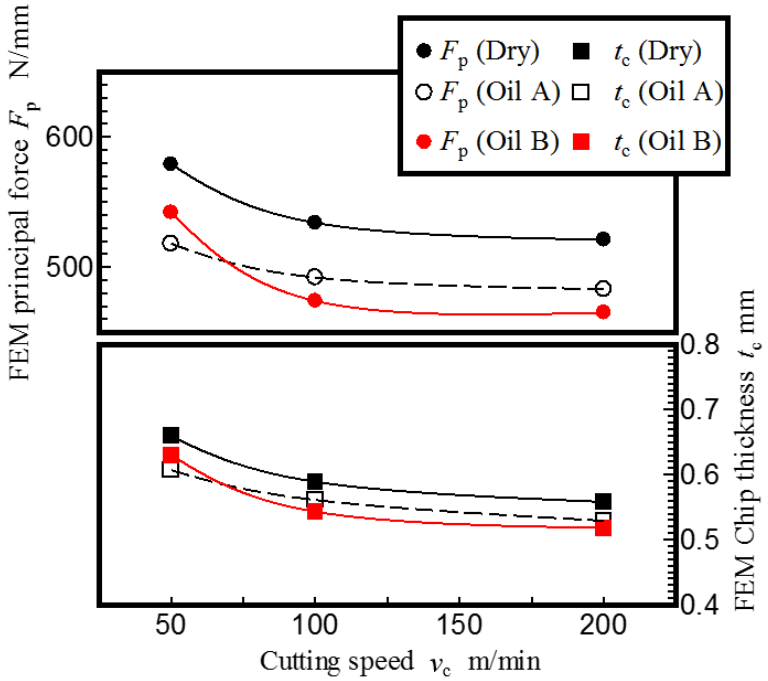

Fig. 3.23 (a) Estimated principal force F and chip thickness t_c by calculated friction coefficient, μ_{cal} input

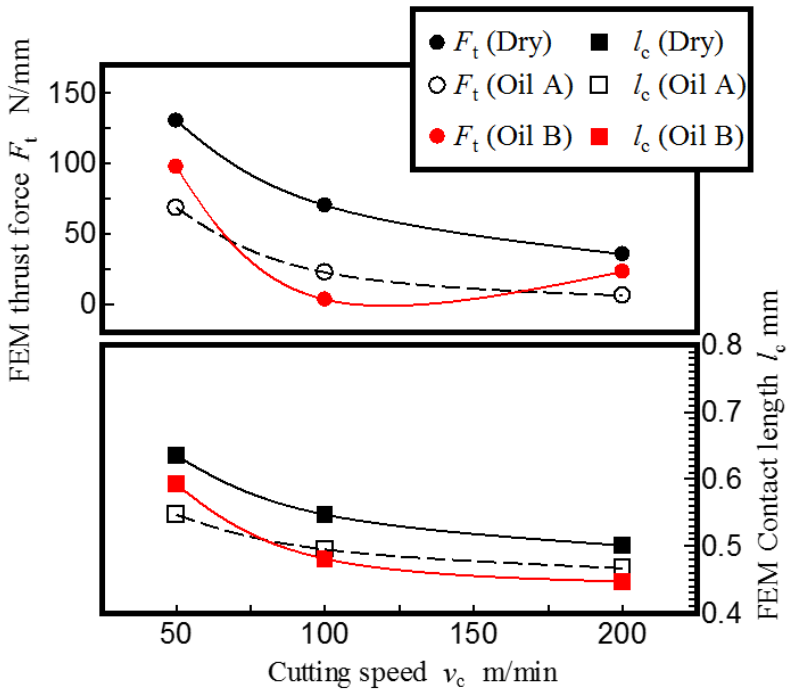

Fig. 3.23 (b) Estimated thrust force F and contact length l_c by calculated friction coefficient, μ_{cal} input

In gaining more understanding, the FEM input fictional coefficient, μ_{cal} is calculated mathematically through **Eq. (3.4)**, to obtain reliable chip thickness t_c. The *Simplified FEM model (Model A)* is re-executed with calculated frictional coefficient, μ_{cal}, and the estimated results are shown in **Fig. 3.23 (a)**.

It is observed that, chip thickness t_c is estimated with a good agreement with the experimental data, as well as accuracy of principal force F_p is significantly increased. Vice versa, thrust force F_t is estimated with large error, as the tool-chip contact length l_c is also estimated with large error. Hence, it can be concluded that chip thickness t_c and MQL friction coefficient μ_{MQL} input are really important parameters for the FEM to estimate principal force F_p and thrust force F_t.

(b) Chip thickness constraint FEM model (Model B)

Based on the information obtained from the *Simplified FEM model (Model A)*, the *Chip thickness constraint FEM model (Model B)* is utilized; where an additional Eulerian deformation constraint is added with the gap between the deformation-constraints to the cutting tool surface is equivalent to the size of MQL chip thickness, t_c ($\approx t_{exp}$). Additional to the deformation constraint, the *Chip thickness constraint FEM model (Model B)* is executed with MQL friction coefficient μ_{MQL} input.

As the result, it is observed that, the *Chip thickness constraint FEM model (Model B)*, estimates principal force F_p, thrust force F_t and tool-chip contact length l_c with a good degree of accuracy, as shown in **Figs 3.24** and **3.25**. It can be concluded that, behavior of MQL can be estimated by the FEM in terms of lubrication effect, from MQL friction coefficient μ_{MQL} and chip thickness t_c.

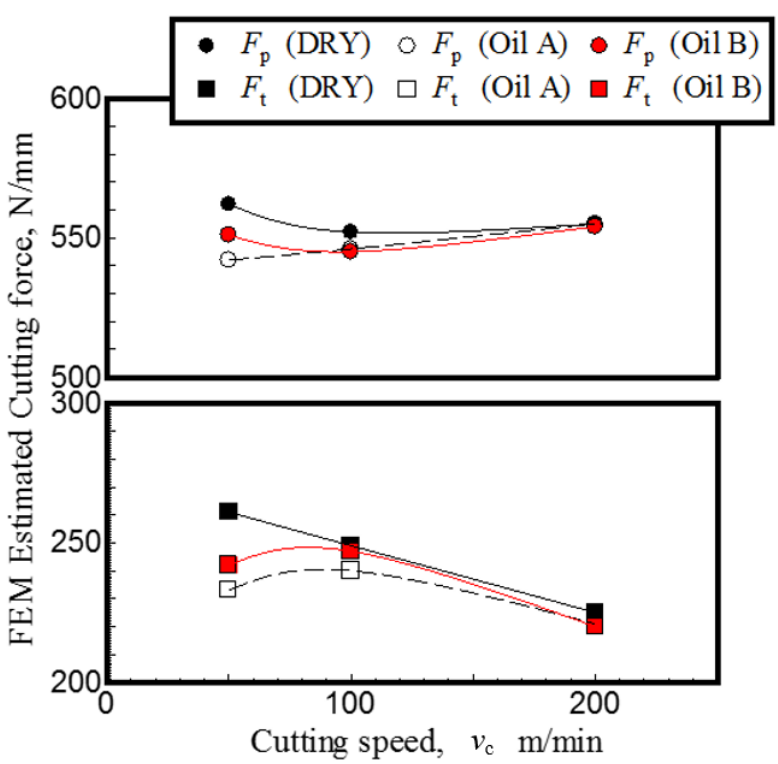

Fig. 3.24 Relationship between cutting speed v_c and cutting force F estimated by MQL estimation FEM Model B

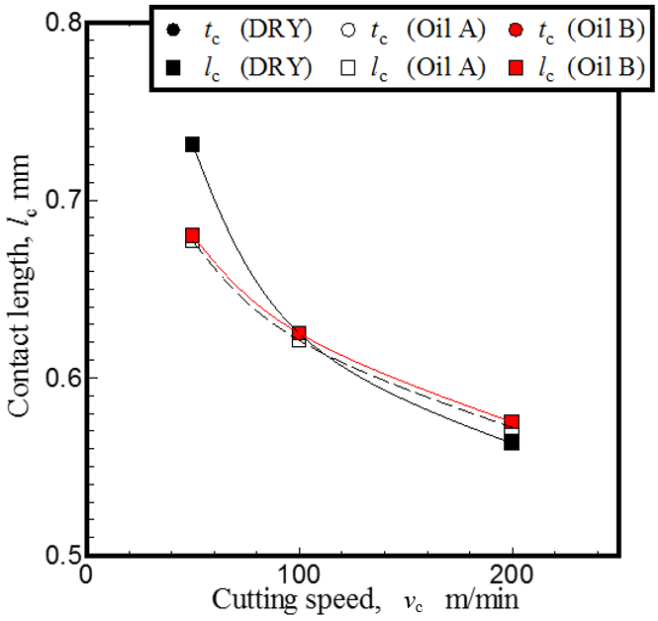

Fig. 3.25 Relationship between cutting speed v_c and contact length l_c estimated by FEM Model B

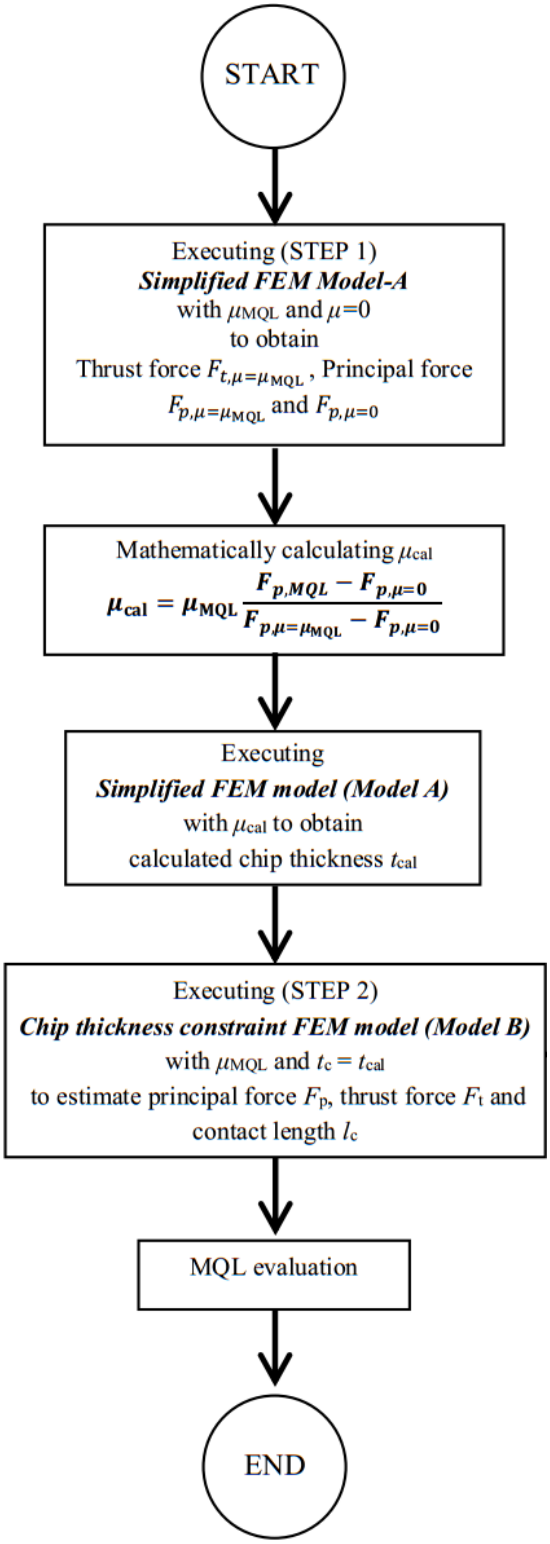

Fig. 3.26 FEM MQL evaluation process

(c) FEM MQL evaluation process

It can be summarized from the finding that, it is capable of arranging the *Simplified FEM model (Model A)* and the *Chip thickness constraint FEM model (Model B)* to evaluate MQL assisted cutting process. The process flow is shown in FEM MQL Estimation Process in **Fig. 3.26**.

At the beginning of the process, in STEP 1, FEM model-A estimates the chip thickness mathematically from the input MQL friction coefficient μ_{MQL}. Next, in STEP 2, FEM model B estimates the principal force F_p, thrust force F_t and tool-chip contact length l_c with the input MQL friction coefficient μ_{MQL} and calculated chip thickness t_{cal} by FEM model-A. Finally, MQL evaluation is executed.

It is needed to be taken into consideration that the presented FEM MQL evaluation process is limited under the conditions applied throughout the study, such as, tool and workpiece geometry, material properties and coating type. It is needed to further the study in utilizing the *FEM MQL Estimation Process* for different cutting condition, material and MQL systems.

3.5 Conclusions

In order to evaluate MQL assisted cutting process in terms of lubrication effect by FEM, two FEM models have been proposed, and several conclusions can be made as following:

1. Both FEM models work in a serial manner, and the validity of the models is verified by equivalent experimental procedure of dry and MQL cutting tests.
2. Experimentally obtained data such as the cutting force *F*; MQL friction

coefficient μ_{MQL}, tool-chip contact length l_c and chip thickness t_c are utilized in validating the FEM model accuracy.

3. The FEM models applied Lagrangian and Arbitrary Lagrangian-Eulerian (ALE) formulations in estimating the chip thickness. This chip thickness will then be input into FEM model with the Arbitrary Lagrangian-Eulerian (ALE) formulation to estimate principal force F_p, thrust force F_t and tool-chip contact length l_c.
4. It is found that cutting force F has a direct relationship with MQL friction coefficient μ_{MQL} and chip thickness t_c. This phenomenon is evaluated by FEM, where various MQL friction coefficient μ_{MQL} inputs for various types of MQL obtained from the equivalent experimental procedure.
5. The FEM shows good agreement with the experimental results. The study shows that FEM is able to evaluate and to aid in understanding the influence of MQL during the cutting process.
6. Further study can be done in various types of MQL such as high-pressure coolant and cryogenic cutting process and cutting process of difficult-to-cut material.

It is hope that the reliable FEM model in simulating and estimating the influence of MQL onto cutting process behavior applied in the study can be utilized in real life situation in improving the understanding on the MQL process.

References

[1] Debnath, S., Reddy, M. M., & Yi, Q. S. (2014). Environmental friendly cutting fluids and cooling techniques in machining: a review. *Journal of Cleaner Production, 83*, 33-47.

[2] Kopalinsky, E., & Oxley, P. (1984). An Investigation of the Influence of Feed and Rake Angle on the Ratio of Feed Force to Cutting Force when Machining with Negative Rake Angle Tools. CIRP Annals - Manufacturing Technology, 33(1), 43-46.

[3] Sutter, G. (2005). Chip geometries during high-speed machining for orthogonal cutting conditions. International Journal of Machine Tools and Manufacture, 45(6), 719-726.

[4] Childs, T. (2006). Friction modelling in metal cutting. *Wear, 260*(3), 310-318.

[5] Rao, C., Rao, D. N., & Srihari, P. (2013). Influence of Cutting Parameters on Cutting Force and Surface Finish in Turning Operation. Procedia Engineering, 64, 1405-1415.

[6] Agustina, B. D., Bernal, C., Camacho, A., & Rubio, E. (2013). Experimental Analysis of the Cutting Forces Obtained in Dry Turning Processes of UNS A97075 Aluminium Alloys. Procedia Engineering, 63, 694-699.

[7] Denkena, B., & Meyer, R. (2009). An approach to reduce the influence of tool wear on workpiece properties during hard turning. International Journal of Microstructure and Materials Properties, 4(5/6), 605.

[8] Abukhshim, N., Mativenga, P., & Sheikh, M. (2006). Heat generation and temperature prediction in metal cutting: A review and implications for high speed machining. International Journal of Machine Tools and Manufacture, 46(7-8), 782-800.

[9] Inamura, T. (2010) “On the role and potential of engineering simulation,” Int. J. Automation Technol., Vol. 4 No. 3, pp. 214-220.

[10] Matsumura, T., Shirakashi, T., and Usui, E. (2010) Adaptive cutting force prediction in

milling processes, Int. J. Automation Technol., Vol. 4 No. 3, pp. 221-228 (2010).

[11] Ye, G. G., Xue, S. F., Tong, X. H., & Dai, L. H. (2011). Influence of Cutting Conditions on the Cutting Performance of TiAl6V4. Advanced Materials Research, 337, 387-391.

[12] Zhang, G., & Guo, C. (2015). Modeling of Cutting Force Distribution on Tool Edge in Turning Process. Procedia Manufacturing, 1, 454-465.

[13] Zhang, L. (1999). On the separation criteria in the simulation of orthogonal metal cutting using the finite element method. Journal of Materials Processing Technology, 89-90, 273-278.

[14] Abouridouane, M., Klocke, F., Lung, D., & Veselovac, D. (2015). The Mechanics of Cutting: In-situ Measurement and Modelling. *Procedia CIRP, 31*, 246-251.

[15] Arrazola, P. J., & Özel, T. (2010). Investigations on the effects of friction modeling in finite element simulation of machining. International Journal of Mechanical Sciences, 52(1), 31-42.

[16] Ozlu, E., Budak, E., & Molinari, A. (2009). Analytical and experimental investigation of rake contact and friction behavior in metal cutting. International Journal of Machine Tools and Manufacture, 49(11), 865-875.

[17] Ceretti, E., Fallböhmer, P., Wu, W., & Altan, T. (1996). Application of 2D FEM to chip formation in orthogonal cutting. Journal of Materials Processing Technology, 59(1-2), 169-180.

[18] Özel, T. (2006). The influence of friction models on finite element simulations of machining. International Journal of Machine Tools and Manufacture, 46(5), 518-530.

[19] Filice, L., Micari, F., Rizzuti, S., & Umbrello, D. (2007). A critical analysis on the friction modelling in orthogonal machining. International Journal of Machine Tools

and Manufacture, 47(3-4), 709-714.

[20] Bonnet, C., Valiorgue, F., Rech, J., & Hamdi, H. (2008). Improvement of the numerical modeling in orthogonal dry cutting of an AISI 316L stainless steel by the introduction of a new friction model. CIRP Journal of Manufacturing Science and Technology, 1(2), 114-118.

[21] Molinari, A., Cheriguene, R., & Miguelez, H. (2012). Contact variables and thermal effects at the tool–chip interface in orthogonal cutting. *International Journal of Solids and Structures*, *49*(26), 3774-3796.

[22] DEFORM™-3D V10.2, (2011) Scientific Forming Technologies Corporation.

[23] Shirakashi, T., Maekawa, K. and Usui, E, (1983). Flow stress of low carbon steel at high temperature and strain Rate (Part 1) – Propriety of incremental strain method in impact compression test with rapid heating and cooling systems, Bulletin of the Japan Society of Precision Engineering 17 (3), pp. 161-166.

[24] Strenkowski, J. S., & Carroll, J. T. (1985). A Finite Element Model of Orthogonal Metal Cutting," Journal of Engineering for Industry, 107(4), 349.

[25] Davim J.P., and Maranhao, C. (2009). A Study of Plastic Strain and Plastic Strain Rate in Machining of Steel AISI 1045 Using FEM Analysis, Materials and Design 30: 160-165.

CHAPTER 4

EVALUATION ON THE INFLUENCE OF MINIMUM QUANTITY LUBRICATION DURING CUTTING PROCESS BY FINITE ELEMENT METHOD – (COOLING EFFECT)

4.1 Introduction

During a machining process, cutting fluid is applied to reduce the friction levels and suppress the significant increment of cutting temperature [1]. However, the main role of cutting fluid application is to remove heat at the contact zone between tool and chip thickness, and between tool and finished surface. The efficiency of cutting fluid to act as a coolant is measured by defining the temperature and its distribution in the cutting zone [2, 3].

Various temperature measurement techniques are applied through experimental methods in characterizing cutting temperature such as, thermocouple methods [4], infrared imaging [5] and micro structural change [6]. Several numerical models are established to predict the temperature at the shear plane based on mechanical energy, and relationship between the characteristic of resistance at the tool-chip interface, to increase the understanding on temperature distribution during the cutting process. Among these models, finite-element analysis is applied by predicting the effect of cutting fluid on the temperature

distribution in machining by comparing with experimental data [7]

Recently, Minimum Quantity Lubrication (MQL) has been extensively utilized during the machining process, where it is aims to be able to improve the process by combining the positive characteristic of wet and dry machining. It is proven that MQL can decrease manufacturing costs, as well as improvement of working environment [8]. Previous researchers examined the effect of MQL on temperature, surface roughness and machining process, along with the influence of other parameters such as cutting speed v_c, depth-of-cut a, feed rate f and nozzle position [9]. It is found that lower cutting force and temperature obtained from MQL assisted cutting compared to dry and wet machining. It is thought that lesser wear and better surface roughness were obtained during the process [9].

It is found that application of FEM is rarely done in analyzing MQL, due to limited understanding on the behavior of inhomogeneous physical property of MQL mist [7]. Previous study modeled the cutting fluid simulation with the application of computational-fluid-dynamic (CFD) approach. However, heat transfer characteristic between chip and tool is not taken into account, where it is hard to estimate the influence of cooling and lubricating effects with cutting temperature [10-12].

This chapter aims to study the influence of MQL during cutting process with means of FEM in terms of cutting temperature and cooling effect. Previous chapter has discussed the parameter requirement to study MQL influence in terms of chip deformation and cutting force. In this chapter, investigation is done by adding further process in FEM, temperature boundary condition. The Updated FEM MQL Estimation Process Flow is shown as **Fig. 4.1**, where STEP 3 is added for estimating cutting temperature.

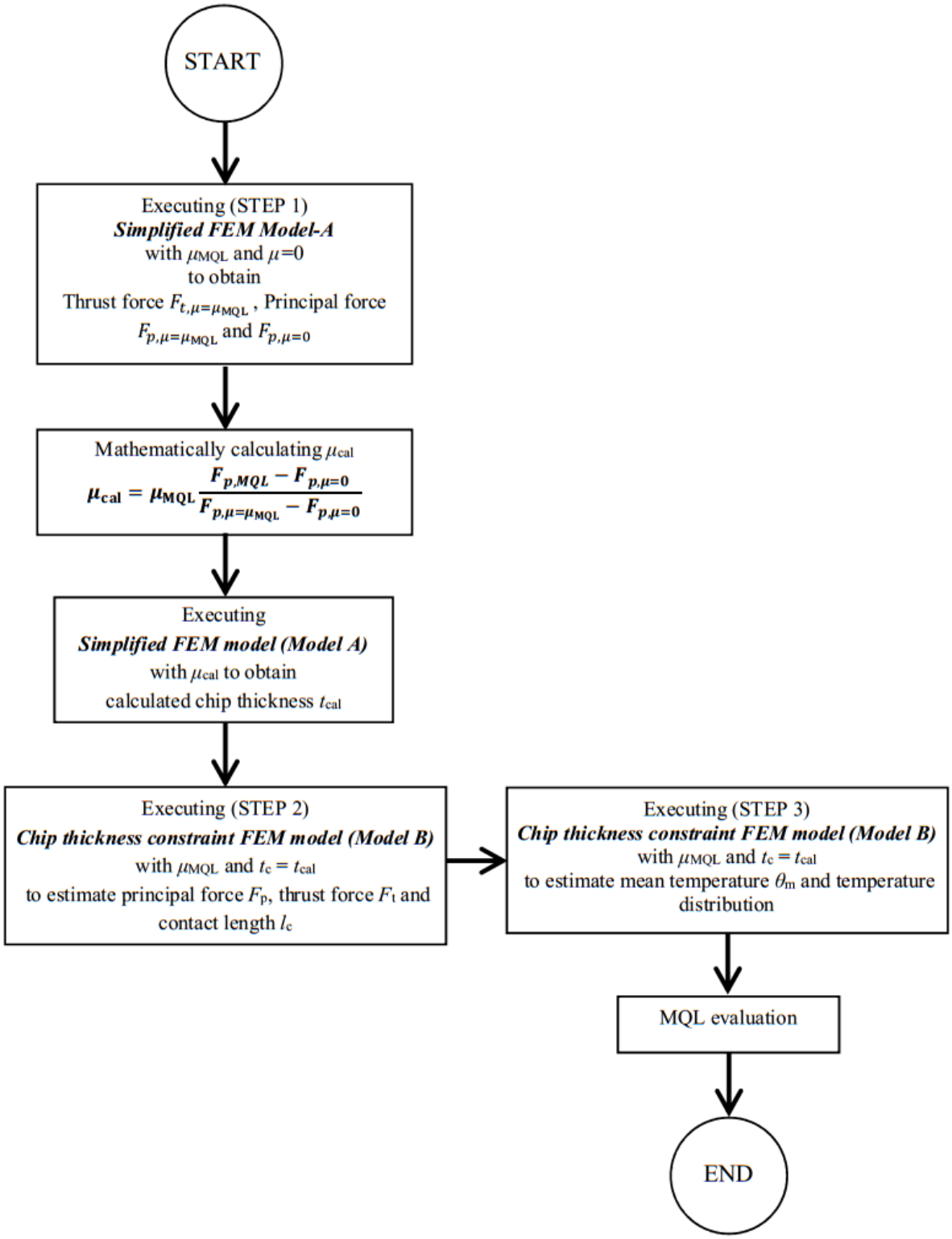

Fig. 4.1 Updated FEM MQL evaluation process for estimating cutting temperature

The FEM model built for STEP 1 and STEP 2 were explained in Chapter 3, while this chapter will discuss specifically on cutting temperature estimation by FEM method in STEP 3. It is assumed that in obtaining precise estimation of cutting temperature affected by MQL, it is important to obtain reliable MQL influence deformation beforehand. This matter was discussed in Chapter 3, and it is concluded that, it is possible to obtain accurate MQL influenced material deformation by FEM.

In this chapter, there are several types of cutting fluids applied during the MQL process, in which oil-based cutting fluid purposely as a lubricant, water-soluble or emulsion-based fluids as a coolant is used. It is revealed that water-based MQL system can reduce cutting temperature, whereas water is effectively exchanged with the environment through conduction due to its higher specific heat capacity compared to oil based cutting fluid [12].

4.2 Experimental procedure

In this study, a pseudo orthogonal cutting test of medium carbon steel, JIS-S45C with a TiCN-coated cermet-cutting tool is carried out by an OKUMA turning center, as shown in **Fig. 4.2**. The insert has 0° rake angle and 10° clearance angle. In the orthogonal cutting tests, cutting speed v_c range of 50, 100 and 200 m/min and depth-of cut a = 0.3 mm (feed rate f in y-direction is 0.3 mm/rev) are applied. The depth-of-cut a (feed rate f) is chosen to be 10 times larger than the tool edge radius of 0.013 mm, which is assumed enough to neglect the effect of tool edge radius. The orthogonal cutting conditions and material properties are shown in **Tables 4.1** and **4.2**.

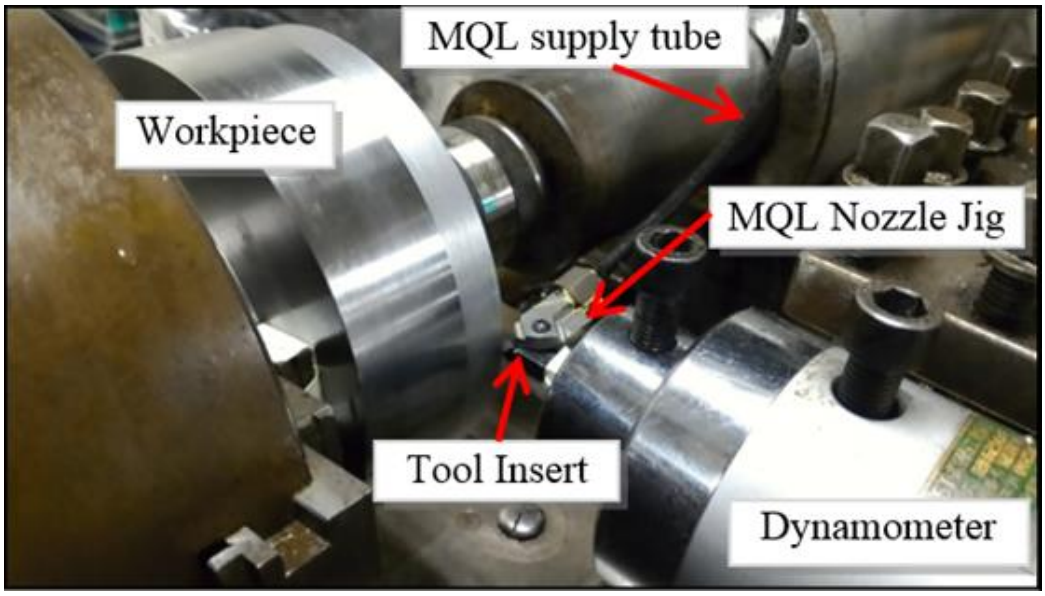

Fig. 4.2 Experimental setup for MQL assisted orthogonal cutting

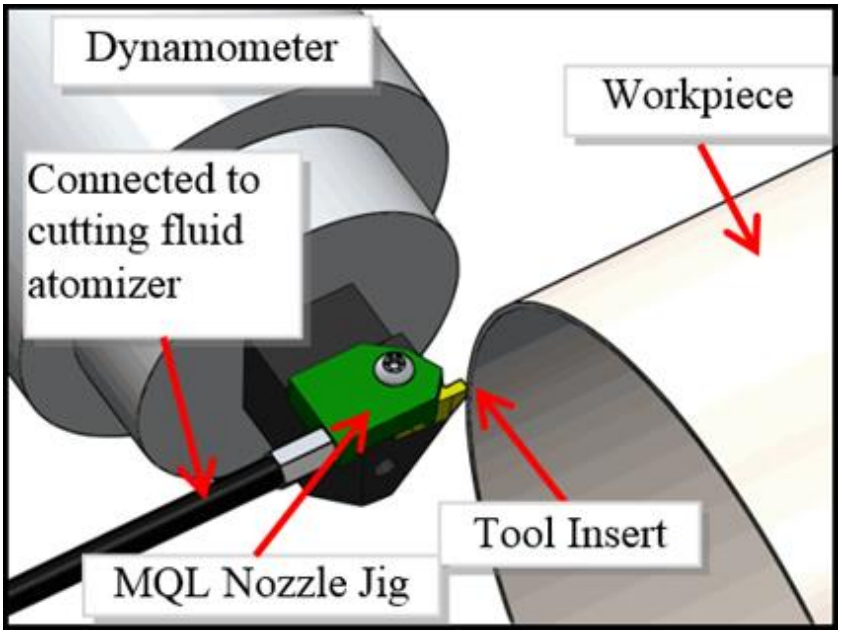

Fig. 4.3 Nozzle outlet to supply oil mist onto the cutting edge

Table 4.1 Orthogonal Cutting Conditions

Cuting tool			TiCN-coated Cermet
Workpiece			JIS S45C
Cutting width	w	[mm]	1.0
Depth of cut	a	[mm]	0.5
Cutting speed	v_c	[m/min]	50, 100, 200

Table 4.2 Material Properties of work material [26]

Material			JIS S45C
Young Modulus	E	[GPa]	212
Density	P	[kg/m^3]	7850
Vickers hardness	HV0.3	[GPa]	1.96
Volumetric heat capacity	c	[10^{6}J/(m^3·K)]	3.54
Thermal conductivity	k	[W/(m·K)]	41.7

Table 4.3 Properties of Oil Mist

Cuting oil			A	B
Type			Vegetable oil	
Viscosity	v	[mm^2/s]	37	
Oil content		[%]	99	30
Flow rate	q	[cc/h]	30	100
Oil pressure	p	[MPa]	0.6	

In the experiments, both dry and MQL assisted cutting tests are executed, where the MQL outlet nozzle for orthogonal cutting is designed to supply oil mist onto the cutting edge accurately through the rake face as shown in **Fig. 4.3**. Two types of oil mist are used, based on the variable composition between non-toxic vegetable oil and water. The composition of Oil-A is 99% vegetable oil and 1% water, while the composition of Oil-B is 30% vegetable oil and 70% water. Oil-A is supplied at 30 mL/h, while Oil-B is supplied 100 mL/h onto the tool rake face during the cutting process, to ensure equivalent lubrication property with Oil-A with additional cooling property. The properties of the oil mist applied throughout this study are summarized in **Table 4.3**.

In the study, mean cutting temperature θ_m for each cutting condition is measured by the application of tool-work thermocouple method, as shown in **Figs. 4.4 (a)**. **Figs. 4.4 (b), (c)** and **(d)** show the thermocouple calibration procedure, where pulse heating method by a pulse heater is utilized. Pairing connections between coated cutting tool material (TiCN-coated cermet) or workpiece material, mild steel (S45C) with Chromel and Alumel-Chromel is heated in the pulse heater chamber by heating element in short period of time **(Fig 4.4 (b))**. During the heating and cooling period, output voltage is recorded by an electronic oscilloscope, as shown in **Fig. 4.4 (c)**. The relationship between output voltage V and mean temperature θ_m between tool and workpiece material is shown in **Fig. 4.4 (d)**.

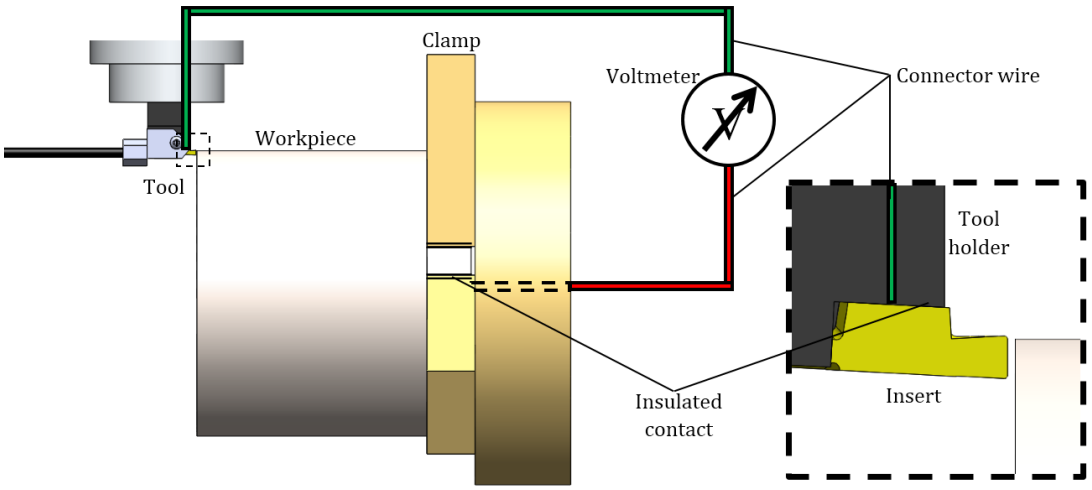

Fig. 4.4 (a) Thermocouple method

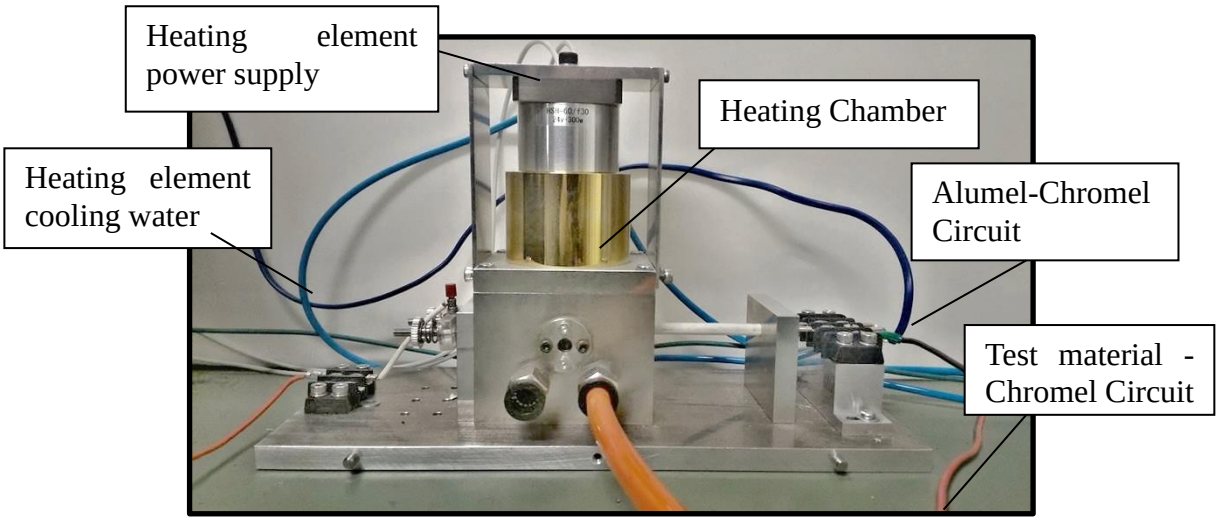

Fig. 4.4 (b) Pulse heater apparatus for thermocouple calibration

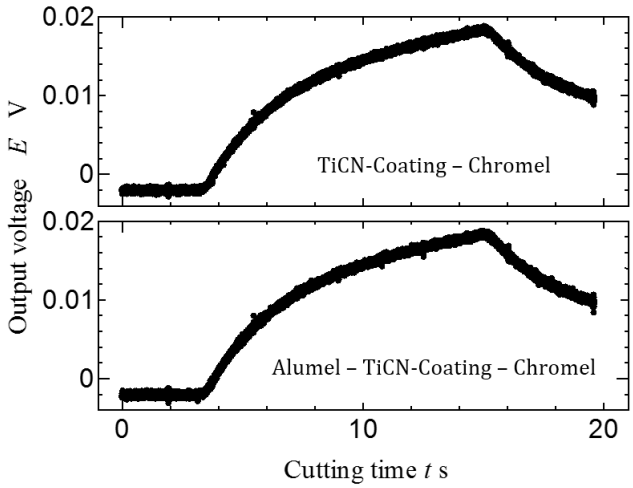

Fig. 4.4 (c) Typical output profile by the pulse heating method

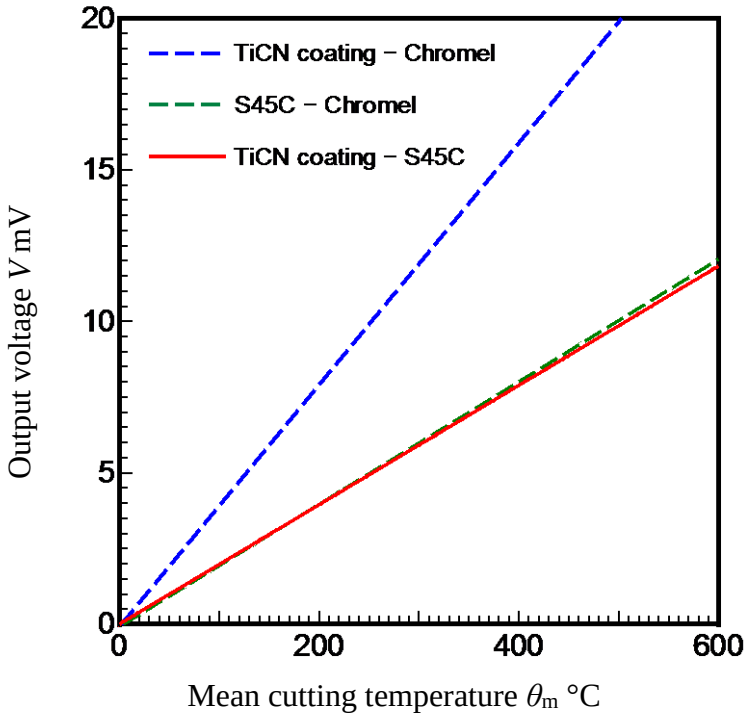

Fig. 4.4 (d) Temperature calibration between Ti-CN coating and mild steel, S45C

4.3 FEM Model Design for Temperature Analysis in MQL

In this study, hybrid thermo-mechanical FEM model, which capable of estimating mechanical deformation along with heat generation and temperature distribution, is employed. Orthogonal cutting FEM simulation model is designed into the application of DEFORM™-3D, whereby the workpiece and cutting tool geometries are designed and simplified by the application of Computer-Aided Design (CAD) software, as shown in **Fig. 4.5** [13-21]. In the simulation, the FEM cutting tool is designed to resemble the actual geometry of the cutting-tool at the cutting zone, with 0° rake angle and 10° clearance angle. The tool edge radius is designed shard as the orthogonal cutting depth is more than 10 times larger than the tool edge radius, similarly to the equivalent experimental procedure.

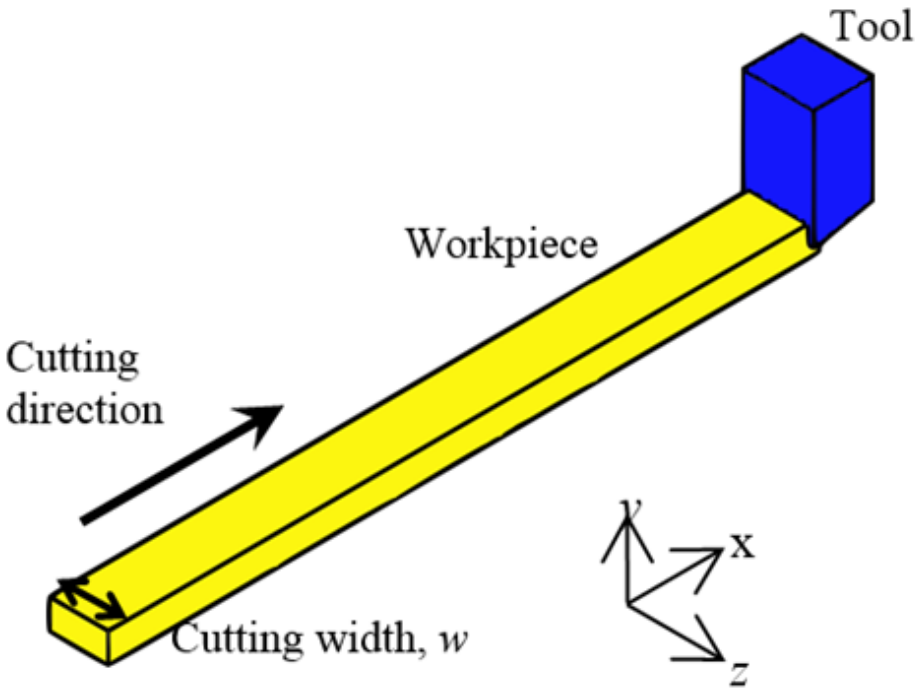

Fig. 4.5 Simplified FEM orthogonal cutting model in DEFORM-3D™

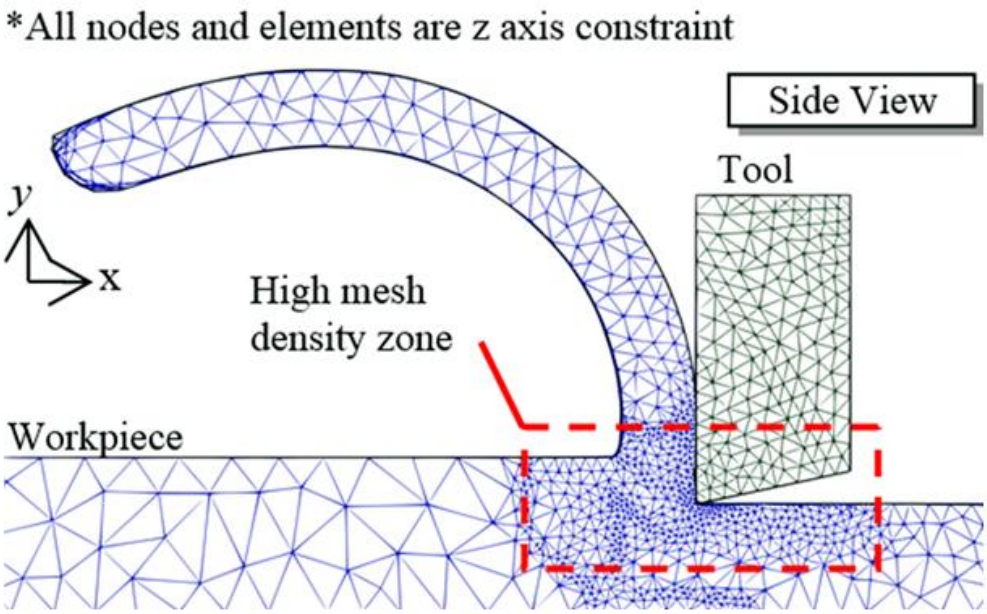

Fig. 4.6 Mesh structure in FEM model

Fig. 4.6 shows the initial overall model meshing, where higher mesh density is designed around the tool-workpiece contact region where large plastic deformation occurs. All workpiece elements are fixed to deform in two-dimensional (x and y axes) similarly to the experimental approach. Adaptive meshing, ability to re-mesh whenever tool and workpiece's mesh overlapping occurred is also applied, and the initial maximum number of elements in the tool is 10,000 elements, 50,000 elements for the workpiece. Here, arbitrary Lagrangian-Eulerian (ALE) method is employed in terms of workpiece material formation [13-24]. Similar model in STEP 2 is utilized, where the gap size between the Eulerian boundary and the tool is equivalent to STEP 1 calculated chip thickness t_{cal} for each cutting condition (cutting speed and type of MQL supplied) (**Fig. 4.7**). Continuous chip is assumed throughout the simulation process, and similar MQL friction coefficient for each cutting conditions.

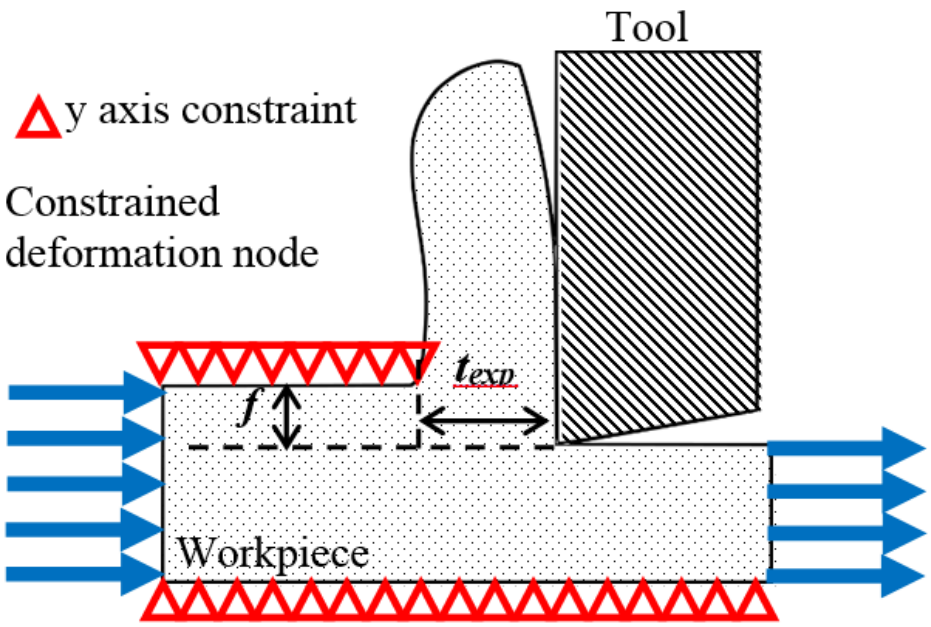

Fig. 4.7 MQL Estimation FEM model (Model B)

In the current study, two out of three zones of heat source are taken into consideration, which is primary zone (shearing deformation) and secondary zone (frictional contact between tool rake face and chip), as shown in **Fig. 4.8** [24].

As the ratio between tool edge and cutting depth is significantly large, the heat generation on tertiary zone (frictional contact between tool flank face and machined surface) is neglected. Although the mechanism of MQL during the cutting process is not yet fully understood, and it is still incapable of simulating the inhomogeneous physical characteristic of MQL mist, following assumptions is made in order to evaluate the influence of MQL during the cutting process:

1. Oil mist completely covers the open surface of tool, chip and workpiece to the environment.
2. MQL affects convective heat transfer coefficient, h properties during the cutting process.
3. The contacts between tool and chip and tool and workpiece are thermally perfect, having a large thermal contact conductance coefficient, h_c (1000 kW/ (m^2•K)).
4. Thermal softening, hardening, and phase transformation of chip and workpiece are neglected in the FEM analysis.
5. The mean temperature θ_m estimated from the contact zone, l_c between tool and chip is calculated and compared to the experimental results.

The boundary conditions and involved coefficients for temperature analysis are summarized in **Fig. 4.9** and **Table 4.4**, respectively.

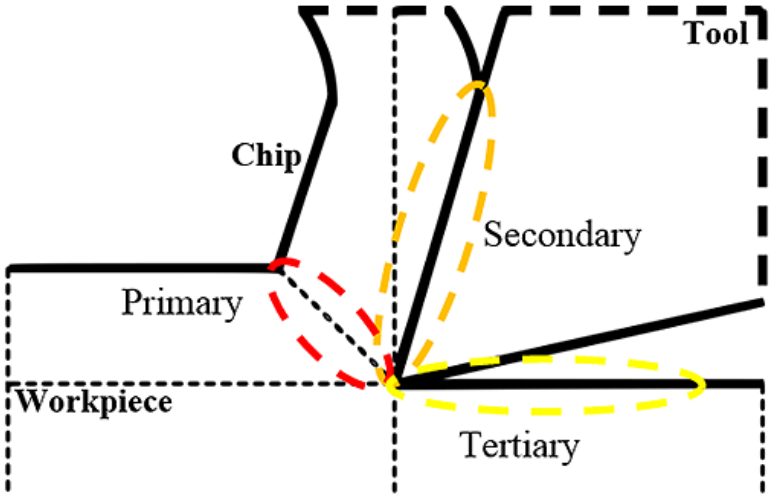

Fig. 4.8 Main sources of heat generation during orthogonal cutting

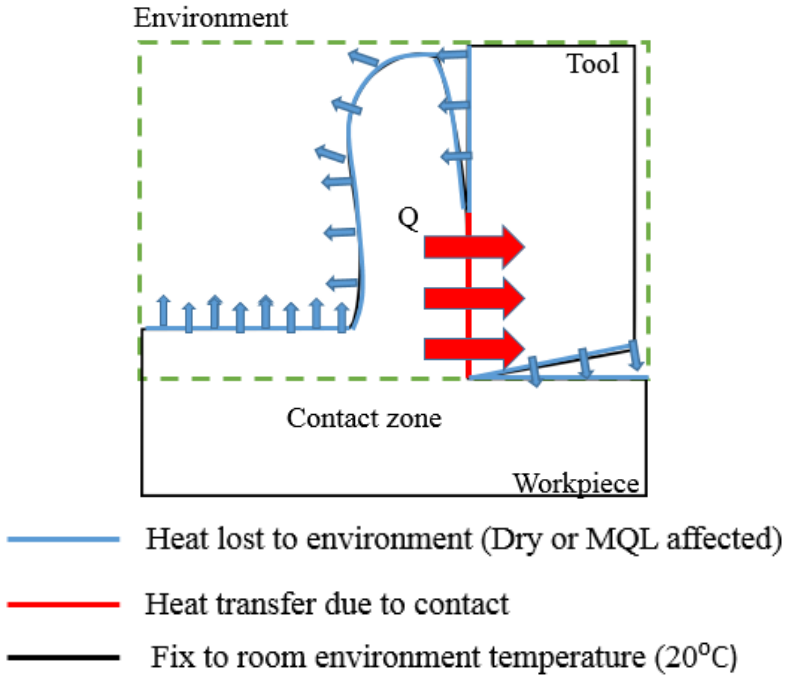

Fig. 4.9 Boundary condition for temperature analysis on MQL influence

Table 4.4 Heat transfer coefficients in FEM analysis

Heat Transfer Coefficient			Dry	Oil-A (Vegetable Oil)	Oil-B (Hydroscopic Oil)
Tool-Chip Boundary	h_c	[kW/(m².K)]	1000	1000	1000
Environment	h	[kW/(m².K)]	0.02	0.35	30

4.4 Experimental and FEM Results and Discussions

4.4.1 Mean cutting temperature of orthogonal cutting of mild steel, S45C

Fig. 4.10 shows the relationship between cutting speed and mean cutting temperature measured by the tool-work thermocouple method during dry and MQL conditions. It is observed that, the mean cutting temperature increases with the increasing of cutting speed, due to increasing cutting energy, regardless the decreasing cutting force. Meanwhile, mean cutting temperature in MQL assisted cutting (Oil-A and Oil-B) is lower than that in the dry cutting. It is assumed that, the existence of foreign substance (oil or water molecule) between chip and tool surface is capable of absorbing or conducting the heat away from the cutting zone. Additionally, MQL assisted cutting with Oil-B shows significantly lower cutting temperature than Oil-A due to its water composition as coolant. The experimental results will be utilized to verify the FEM model later in this study.

4.4.2 FEM evaluation on cutting temperature during MQL application

In the previous chapter, it is proven that FEM model is capable of estimating cutting force F and tool-chip contact length l_c with a good degree of accuracy (~12%). By utilizing the FEM estimated model and cutting force data, influence of MQL in terms of cutting temperature is evaluated.

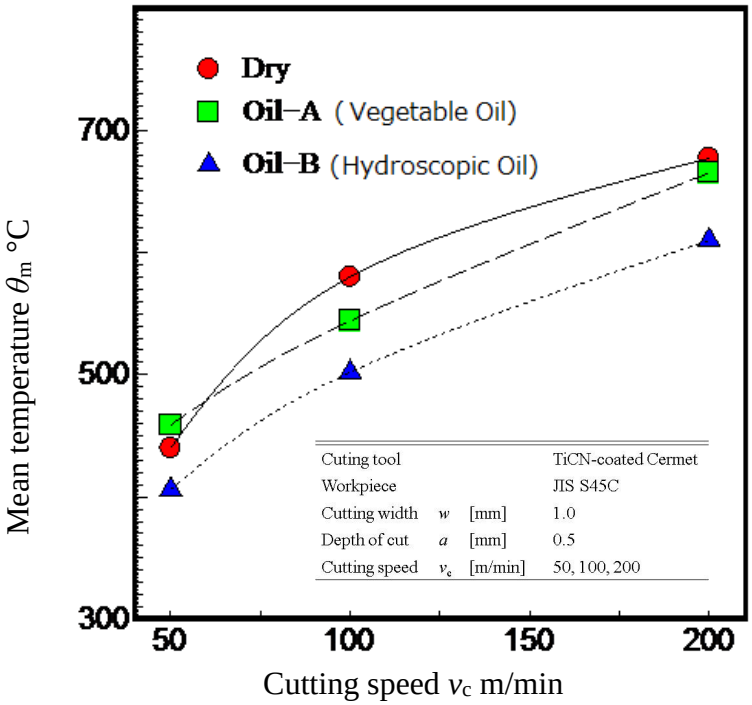

Fig. 4.10 Relationship between cutting speed and experimentally measured mean cutting temperature

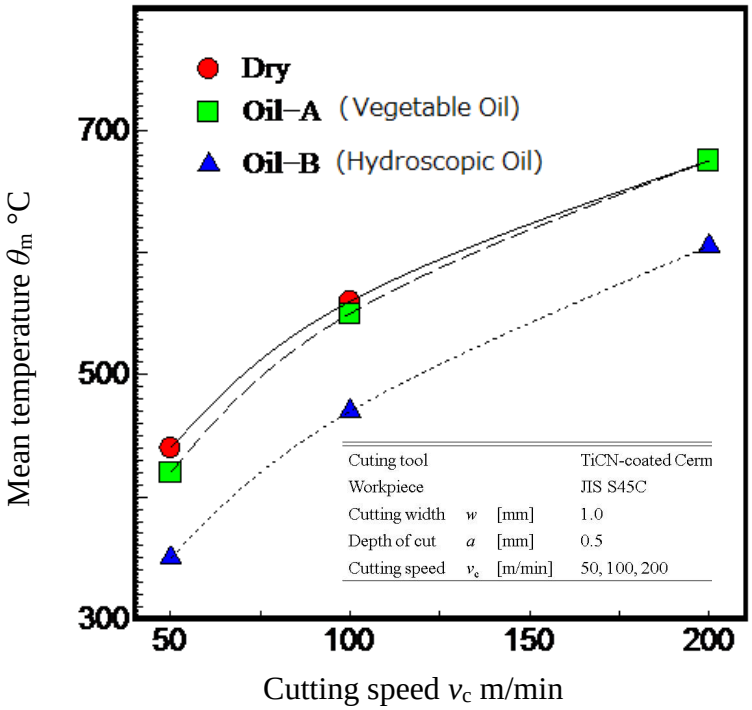

Fig. 4.11 Relationship between cutting speed and mean cutting temperature estimated by FEM with μ_{exp} and chip thickness t_c input.

Fig. 4.11 shows the relationship between cutting speed v_c and mean temperature θ_m at tool-chip contact zone estimated by the FEM analysis. It is observed that, mean temperature θ_m increases as the cutting speed v_c increases, which has similar tendency to the experimental results. It is justified that, the FEM is capable of estimating the mean temperature θ_m in the orthogonal cutting process with a good degree of accuracy, when the appropriate convective heat transfer coefficient, h with respect to the type of mist is considered as a MQL cooling parameter. For more understandings on the effect of MQL during cutting process, temperature distribution comparison on cutting tool and chip estimated by FEM between dry and Oil-B is analyzed for cutting speed of 100 m/min, as shown in **Fig. 4.12 (a), (b) and (c).**

It is observed that, estimated temperature distribution for orthogonal cutting process supplied with Oil-B is smaller than that in the dry process. It is also observed that lesser size of the highest temperature zone (red color zone) is estimated in the middle of tool-chip contact zone. Furthermore, the tool edge temperature T is reduced than that in the dry orthogonal cutting. It is observed that, the MQL is taken into effect instantaneously as the chip separated from the tool rake surface.

It is assumed that, MQL is capable of enhancing the tool life by suppressing the size of the thermal affected zone (distribution zone) in the tool body during the cutting process. Additionally, coolant type MQL is capable of reducing the magnitude of temperature of the tool edge during the MQL assisted cutting process. Thus, the application of coolant type MQL during cutting process is heavily recommended.

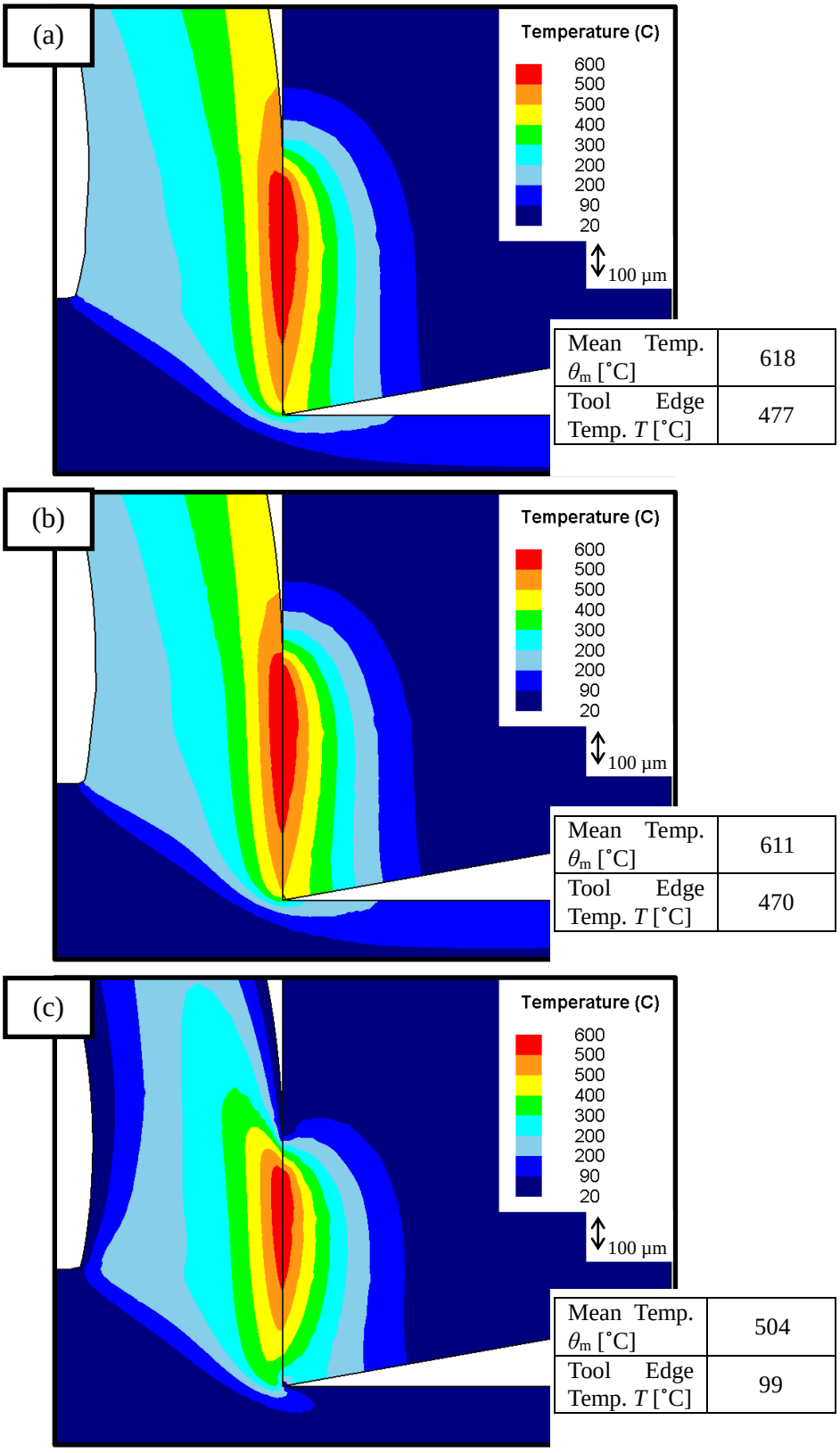

Fig. 4.12 Temperature distribution on tool and chip for cutting speed v_c=100 m/min for (a) dry and (b) Oil A (c) Oil B MQL conditions at saturated temperature

4.4.3 Surveying for new MQL system (Extreme Cold Mist) by FEM

A survey has been made for a new MQL system based on lubrication and coolant effect of MQL, evaluated by FEM in Chapter 3 and current chapter, respectively. It can be summarized that, a good MQL system must have higher lubrication property, and higher convective heat transfer coefficient, *h*. **Table 4.5** shows the types of surveyed MQL properties that are going to be tested through the application of FEM, which are Type I and Type II. Type I is the characteristic of the MQL system with Oil B supplied in extreme low temperature (-13.6°C), while Type II is the characteristic of the MQL system with dry air supplied in extreme low temperature (-13.6°C).

Figs. 4.13 (a) and **(b)** shows the temperature distribution and mean temperature at saturation point for each type of surveyed MQL; Type I, and Type II, respectively.

Table 4.5: Properties of surveyed MQL

Heat Transfer Coefficient			Dry	Oil-B	**Type I**	Type II
Contact heat transfer coefficient	h_c	[kW/(m².K)]	1000	1000	**1000**	1000
Convective heat transfer coefficient	h	[kW/(m².K)]	0.02	30	**30**	0.02
Environment temperature	T_0	[°C]	20	20	**-13.6**	-13.6

Type I: Target MQL properties (Extreme cold mist)

Type II: Extreme cold air

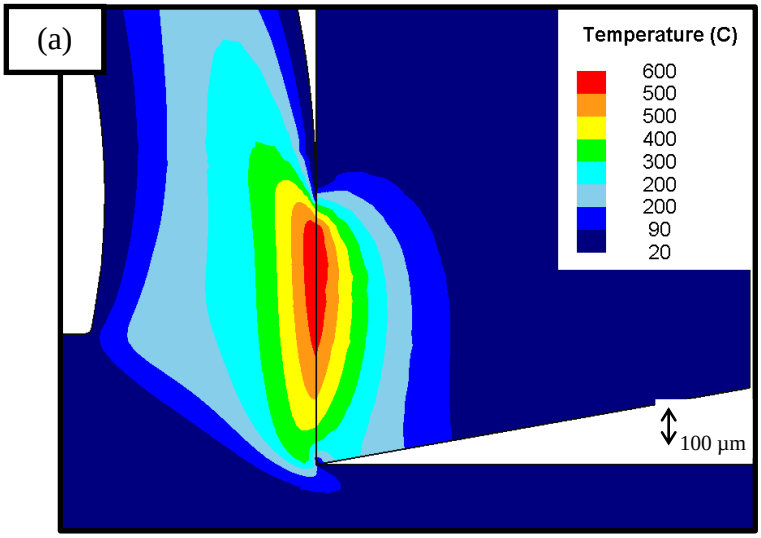

Mean Temp. θ_m [˚C]	483
Tool Edge Temp. T [˚C]	65

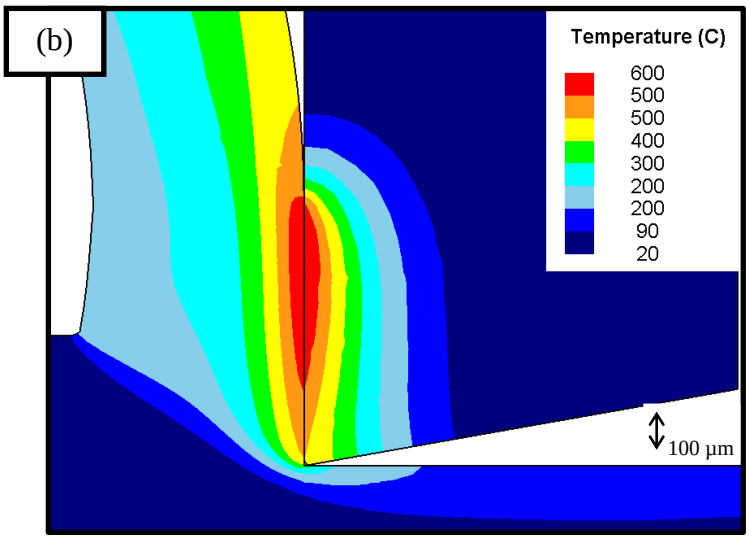

Mean Temp. θ_m [˚C]	603
Tool Edge Temp. T [˚C]	465

Fig. 4.13 Temperature distribution on tool and chip for cutting speed v_c=100 m/min for surveyed MQL (a) Type I and (b) Type II conditions at saturated temperature

It is estimated by FEM that, the temperature distribution inside tool when saturated is smaller when higher convective heat transfer coefficient, *h* is applied (Oil B, Type I). This characteristic can be improved further by supplying extreme cold air -13.6 ˚C (Type I). It is estimated that, the new MQL system (Type I) is capable of reducing the tool edge temperature *T* up to 30% compared to conventional Oil-B supplied MQL system. This new MQL system is called Extreme Cold Mist and will be applied on the turning process difficult to cut material, which will be discussed in Chapter 6.

4.4 Conclusions

This chapter discussed about evaluating the effectiveness of MQL by simulating the cutting process through the application of FEM. The FEM model implemented Arbitrary Lagrangian-Eulerian (ALE), where chip thickness is pre-estimated along with the MQL friction coefficients. Convective heat transfer coefficient is taken into consideration in simulating the effect of MQL as coolant. Several conclusions can be made as following:

1. The FEM analysis shows significant accuracy with the experimental results. The study shows that FEM can aid in understanding the influence of MQL during the cutting process.
2. It is estimated from the survey; the new MQL systems (Extreme Cold Mist) have higher effectiveness in reducing the temperature, thus this new system is suggested to further the study onto cutting process of difficult-to-cut material.
3. Additionally, further study can also be done on various types of MQL through FEM such as high pressure coolant and cryogenic MQL assisted cutting process in the future.

References

[1] Sales, W. F., Diniz, A. E., & Machado, Á R. (2001). Application of cutting fluids in machining processes. Journal of the Brazilian Society of Mechanical Sciences, 23(2).

[2] Brinksmeier, E., Meyer, D., Huesmann-Cordes, A. G., Herrmann, C., (2015). Metalworking fluids—Mechanisms and performance, CIRP Annals - Manufacturing Technology, Volume 64, Issue 2, 605-628

[3] Debnath, S., Reddy, M. M., & Yi, Q. S. (2014). Environmental friendly cutting fluids and cooling techniques in machining: a review. *Journal of Cleaner Production, 83*, 33-47.

[4] Leshock, C. E., & Shin, Y. C. (1997). Investigation on Cutting Temperature in Turning by a Tool-Work Thermocouple Technique. Journal of Manufacturing Science and Engineering, 119(4A), 502.

[5] Artozoul, J., Lescalier, C., Bomont, O., & Dudzinski, D. (2014). Extended infrared thermography applied to orthogonal cutting: Mechanical and thermal aspects. Applied Thermal Engineering, 64(1-2), 441-452.

[6] Yan, L., Yang, W., Jin, H., & Wang, Z. (2011). Analytical modelling of microstructure changes in the machining of 304 stainless steel. The International Journal of Advanced Manufacturing Technology, 58(1-4), 45-55.

[7] Bollig P., Faltin C., Schießl R., Schneider J., Maas U., Schulze V. (2015). Considering the Influence of Minimum Quantity Lubrication for Modelling Changes in Temperature, Forces and Phase Transformations during Machining. Procedia CIRP, Volume 31, 2015, Pages 142-147

[8] Braga, D. U., Diniz, A. E., Miranda, G. W., &Coppini, N. L. (2002). Using a minimum quantity of lubricant (MQL) and a diamond coated tool in the drilling of aluminum–

silicon alloys. Journal of Materials Processing Technology, 122(1), 127-138.

[9] Hadad, M. and Sadeghi, B. (2013). Minimum quantity lubrication-MQL turning of AISI 4140 steel alloy. Journal of Cleaner Production, 54, 332-343.

[10] Chen, M., Jiang, L., Shi, B. W., Liu, Z. Q., & An, Q. L. (2012). CFD Analysis on the Flow Field of Minimum Quantity Lubrication during External Thread Turning. Materials Science Forum, 723, 113-118.

[11] Obikawa, T., Asano, Y., & Kamata, Y. (2009). Computer fluid dynamics analysis for efficient spraying of oil mist in finish-turning of Inconel 718. International Journal of Machine Tools and Manufacture, 49(12-13), 971-978.

[12] Lacalle, L. N. L., Angulo, C., Lamikiz, A., & Sánchez, J. (2006). Experimental and numerical investigation of the effect of spray cutting fluids in high speed milling. Journal of Materials Processing Technology, 172(1), 11-15.

[13] Agustina, B. D., Bernal, C., Camacho, A., & Rubio, E. (2013). Experimental Analysis of the Cutting Forces Obtained in Dry Turning Processes of UNS A97075 Aluminium Alloys. Procedia Engineering, 63, 694-699.

[14] Ye, G. G., Xue, S. F., Tong, X. H., & Dai, L. H. (2011). Influence of Cutting Conditions on the Cutting Performance of TiAl6V4. Advanced Materials Research, 337, 387-391.

[15] Molinari, A., Cheriguene, R., & Miguelez, H. (2012). Contact variables and thermal effects at the tool–chip interface in orthogonal cutting. International Journal of Solids and Structures, 49(26), 3774-3796.

[16] Zhang, L. (1999). On the separation criteria in the simulation of orthogonal metal cutting using the finite element method. Journal of Materials Processing Technology, 89-90, 273-278.

[17] Abouridouane, M., Klocke, F., Lung, D., & Veselovac, D. (2015). The Mechanics of Cutting: In-situ Measurement and Modelling. *Procedia CIRP, 31*, 246-251.

[18] Arrazola, P. J., & Özel, T. (2010). Investigations on the effects of friction modeling in finite element simulation of machining. International Journal of Mechanical Sciences, 52(1), 31-42.

[19] Ozlu, E., Budak, E., & Molinari, A. (2009). Analytical and experimental investigation of rake contact and friction behavior in metal cutting. International Journal of Machine Tools and Manufacture, 49(11), 865-875.

[20] Ceretti, E., Fallböhmer, P., Wu, W., & Altan, T. (1996). Application of 2D FEM to chip formation in orthogonal cutting. Journal of Materials Processing Technology, 59(1-2), 169-180.

[21] Özel, T. (2006). The influence of friction models on finite element simulations of machining. International Journal of Machine Tools and Manufacture, 46(5), 518-530.

[22] Filice, L., Micari, F., Rizzuti, S., & Umbrello, D. (2007). A critical analysis on the friction modelling in orthogonal machining. International Journal of Machine Tools and Manufacture, 47(3-4), 709-714.

[23] Bonnet, C., Valiorgue, F., Rech, J., & Hamdi, H. (2008). Improvement of the numerical modeling in orthogonal dry cutting of an AISI 316L stainless steel by the introduction of a new friction model. CIRP Journal of Manufacturing Science and Technology, 1(2), 114-118.

[24] Abukhshim, N., Mativenga, P., & Sheikh, M. (2006). Heat generation and temperature prediction in metal cutting: A review and implications for high speed machining. International Journal of Machine Tools and Manufacture, 46(7-8), 782-800.

[25] DEFORM™-3D V10.2, (2011) Scientific Forming Technologies Corporation.

CHAPTER 5

TEMPERATURE MEASUREMENT DURING MACHINING PROCESS –APPLICATION OF PYROMETER

5.1 Introduction

Cutting temperature is one of the most important parameters indicating the heat produced during cutting process, due to shearing deformation and frictional contact between the tool/chip and also the tool–workpiece interface, respectively. The higher the energy generated/needed in the cutting, the higher the cutting temperature will be; this relationship depends on the cutting depth, feed rate and cutting speed. Cutting temperature is also influenced by several other factors, including thermal conductivity, tool/workpiece hardness, ductility, coolant, and lubrication [1].

Temperature – especially high-temperature – is very important in cutting due to its effects. Excessive thermal energy generated during cutting is one possible factor in lowering the strength, hardness, stiffness and wear resistance to the cutting tool, which in turn can lead to plastic deformation that changes the tool's geometry. Such immoderate energy also influences accuracy and dimension on the workpiece during cutting. At a very high cutting temperature, thermal damage and metallurgical changes usually occurs and induces undesired properties on the machined surface [2].

Materials are continuously emitting electromagnetic radiation as atoms and molecules detach due to internal energy. Electromagnetic radiation wavelengths can be tens of meters

(the length of a radio wave) or as small as 1.μm or below (the wavelength of cosmic rays). This study only considers thermal radiation, which is emitted by all elements or substances in the universe.

Fig. 5.1 shows the wavelength and frequency domains of thermal radiation, showing the respective positions on the electromagnetic spectrum. The thermal radiation domain is positioned approximately between 0.1 and 100 mm. The visible range is situated roughly between the wavelengths of 0.4 and 0.7 mm. As wavelengths increase, the thermal radiation domain can be divided into three consecutive sub domains: the ultraviolet range, the visible range, and the infrared range.

The intensity of thermal radiation, *I*, is defined as the radiant energy per unit of time per unit of solid angle per unit of area of the emitter, projected normally to the line of view of the receiver from the radiation element [6]. Quantum arguments of Planck [7], verified experimentally, have shown that for a blackbody, the spectral distributions of hemispherical emissive power and radiant intensity in a vacuum are given as a function of wavelength l and the blackbody's absolute temperature *T*. The monochromatic intensity of blackbody radiation, $I_{b\lambda}$, has been identified as:

$$I_{b\lambda}(\lambda, T) = \frac{2hc^2}{\lambda^5\{\exp(hc/k\lambda) - 1\}} \tag{5.1}$$

where:

k =1.3805 × 10^{-23} J/K is the Boltzmann constant,

h =6.6256 × 10^{-34} J·s is the Planck constant,

c =3×10^8 m/s is the speed of light in a vacuum.

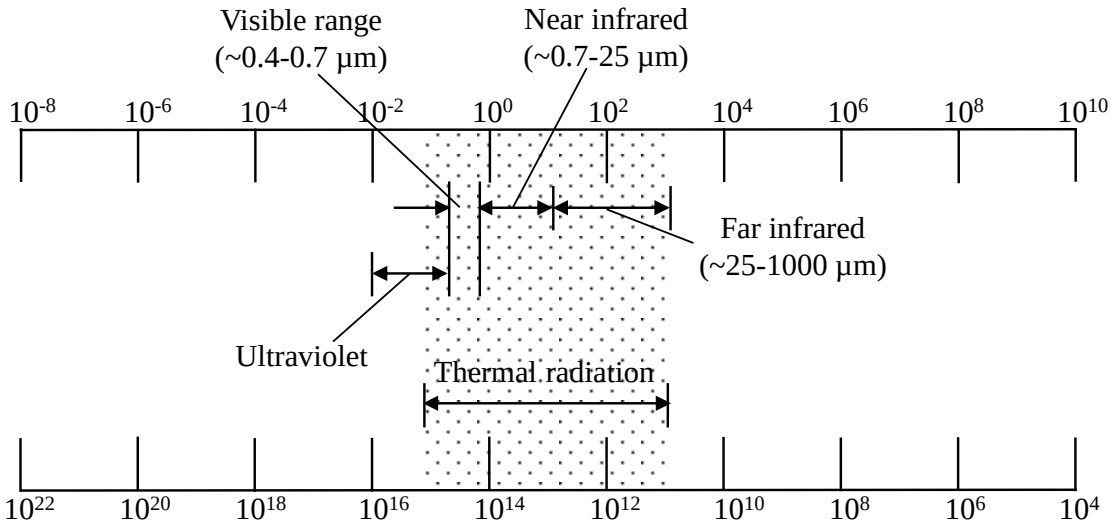

Fig. 5.1 Wavelength and frequency domains of thermal radiation and positions on the electromagnetic spectrum

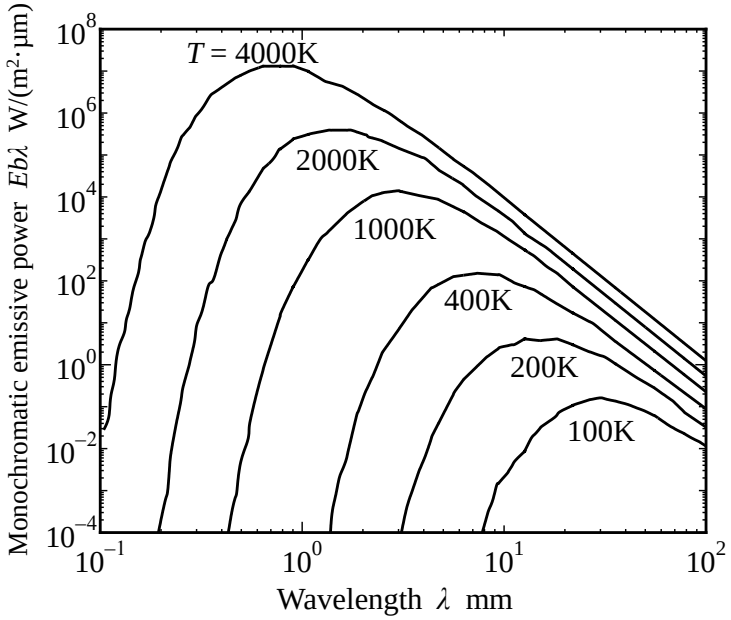

Fig. 5.2 Radiant energy of a black body

The unit of $I_{b\lambda}$ is W/(m^3·sr), the number of Watts per unit of wavelength (W); the unit of the area normal to the ray is m^2, and the unit of the solid angle is sr, steradian. The total intensity of blackbody radiation, I_b, is acquired by integrating the monochromatic intensity, $I_{b\lambda}$, over the entire radiation spectrum:

$$I_b(T) = \int_{\lambda} I_{b\lambda}(\lambda, T) d\lambda \tag{5.2}$$

The total intensity represents the energy conveyed by the ray (in a certain direction) per unit of time, solid angle, and area normal to the direction of the ray. By multiplying π by $I_{b\lambda}$, the monochromatic hemispherical emissive power of the black surface, $E_{b\lambda}$, can be obtained as:

$$E_{b\lambda}(\lambda, T) = \pi I_{b\lambda}(\lambda, T) = \frac{C_1}{\lambda^5 \{\exp(C_2/\lambda T) - 1\}} \tag{5.3}$$

For which the values of the constants C_1 and C_2 can be deducted from equation (5.1):

$$C_1 = 2\pi hc^2 = 3.742 \text{x} 10^{-16} \text{ W.m}^2 \tag{5.4}$$

$$C_2 = hc/k = 1.439 \text{x} 10^{-2} \text{ m.K} \tag{5.5}$$

The unit of $E_{b\lambda}$ is W/m^3, which is the energy per unit of time, wavelength, and surface area.**Fig.5.2** shows the $E_{b\lambda}(\lambda,T)$ function for several temperatures. The monochromatic emissive power is shown to intensely increase with the absolute temperature. A maximum

$E_{b\lambda}$value is registered at a characteristic wavelength for each temperature by solving $\partial E_{b\lambda} / \partial \lambda = 0$ in conjunction with **Eq. (5.8)**:

$$\lambda T = 2.898 \text{ x } 10^{-3} \text{m·K} \tag{5.6}$$

This is known as Wien's displacement law [8], and describes the locus of the $E_{b\lambda}$ maximum, represented by a straight line in the logarithmic field, as shown in **Fig. 5.2**. As seen here, the wavelength of maximum $E_{b\lambda}$ varies inversely with the absolute temperature, leading to the conclusion that the bulk of the energy emitted by a blackbody, shifts to gradually shorter wavelengths.

In conclusion, the monochromatic emissive power $E_{b\lambda}$ represents the heat flux emitted from a surface area along all the rays intersected by the hemisphere per unit of wavelength interval. The total hemispherical emissive power of blackbody E_b is calculated by integrating **Eq. (5.2)** over all the wavelengths of the radiation spectrum:

$$E_b(T) = \int_{\lambda} E_{b\lambda}(\lambda, T) d\lambda \tag{5.7}$$

$$E_b(T) = \sigma T^4 \tag{5.8}$$

Here, σ = 5.6697 × 10^{-8}W/(m^2·K^4) is the Stefan–Boltzmann constant. From equations (5.3) and (5.8), it is clear that the total energy radiated from a surface depends on the temperature of the surface; therefore, the temperature of an object can be determined by measuring the total energy radiated. The infrared radiation pyrometer is based on this phenomenon. A blackbody has both an ideal surface and an 'actual' surface; the actual object

has a total emissive power that is less than the emissive power radiating from the blackbody. The emissive power of this 'real' surface is highly affected by the emissivity of the surface. The emissivity is defined as a ratio of the total emissive power of the surface to that of a blackbody at the same temperature. This problem led to the development of the two-color pyrometer that will be used in this study.

5.2 Basic principles of two-color pyrometer

The diagram of the pyrometer is shown in **Fig. 5.3**. The pyrometer consists of optical fibers, sensors and operational amplifiers that have been arranged to collect channel and change the thermal radiation (on the infrared spectrum) to an electrical signal that is recorded with an oscilloscope. Two infrared sensors/detectors are used to detect different spectra of wavelength.

In cutting, thermal energy is emitted by the tool. In this study, the target area is the flank face near to the cutting edge. The thermal energy is emitted on the infrared spectrum and is collected by the end of the chalcogenide fiber. This infrared ray will be transmitted through the fiber to the two-color detector. The detector consists of two types of detector assembled in a sandwich configuration, which convert the infrared ray to electrical signals. These signals are recorded by an oscilloscope.

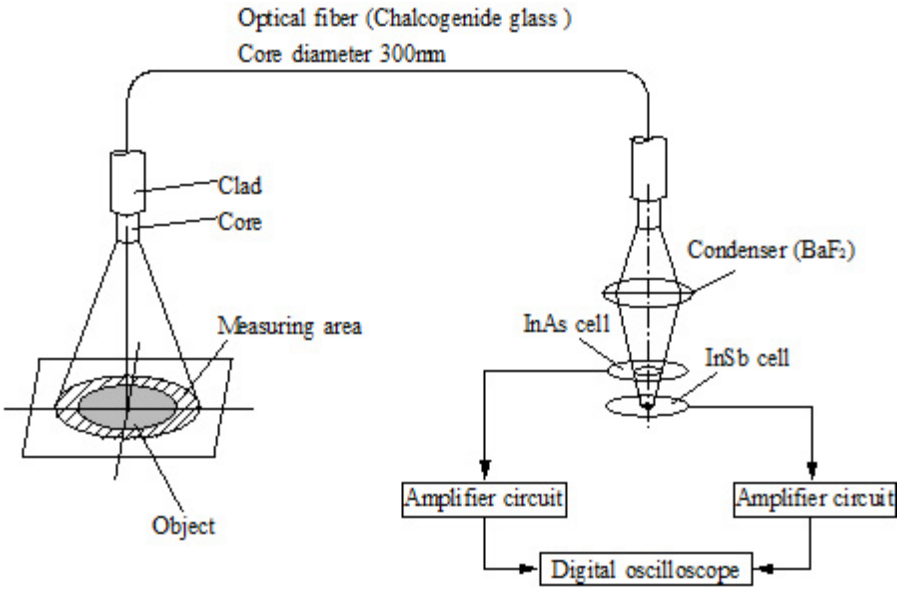

Fig. 5.3 Fundamental diagram of two-color pyrometer with optical fiber

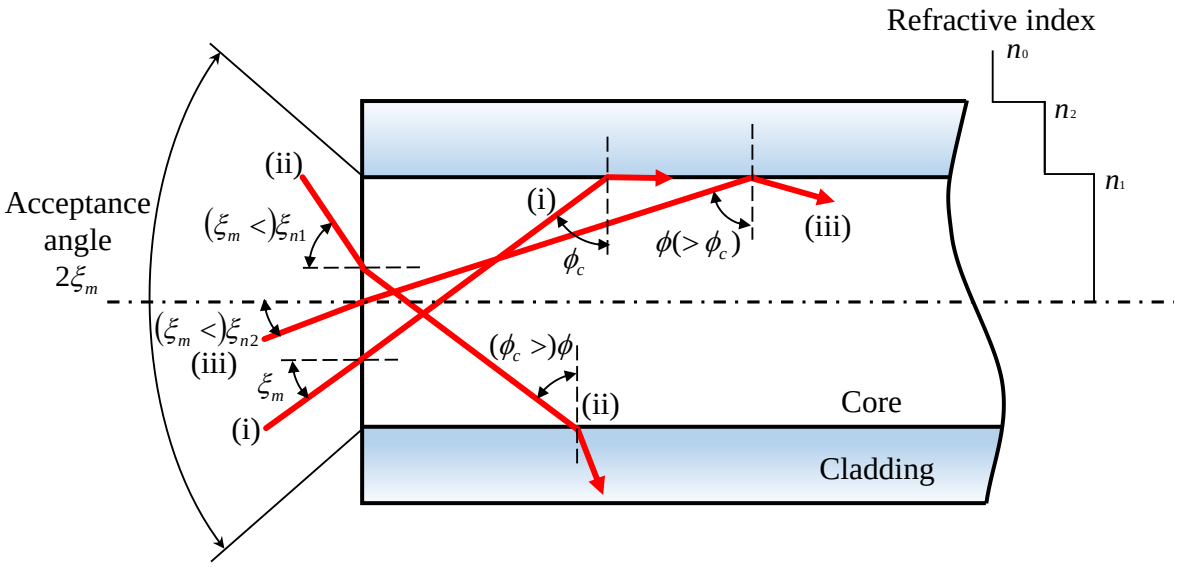

Fig. 5.4 Structure of the step-index optical fiber

5.2.1 Components of two-color pyrometer

It is essential to perform proper selection of optical fiber, infrared detector and other important components of the pyrometer in order to ensure the accuracy and functionality of the built pyrometer. In this section, the main components of the two-color pyrometer will therefore be discussed in detail.

5.2.2 Optical fiber

There are two major groups in the production of optical fiber: multimode and single-mode. Multi-mode fiber is categorized into two further types: step-index and graded-index. In graded-index fiber, the core refractive index is differentiated by the radial distance originating from the center of the fiber in the form of a function.

In this study, step-index NSG chalcogenide optical fiber is used to build the pyrometer [14]. **Fig. 5.4** illustrates the structure of the step-index optical fiber. Since the core's refraction index, n_1, is higher than the index of the cladding's refraction, n_2, the ray that enters the core at a smaller angle than the critical angle is guided along the fiber. The critical angle (minimum angle for total internal reflection) is regulated by the index of the refraction variance of the core and cladding materials as follows:

$$\sin \phi_c = \frac{n_2}{n_1} \tag{5.9}$$

$$n_0 \sin \xi_m = n_1 \sin\left(\frac{\pi}{2} - \phi_c\right) \tag{5.10}$$

The rays that reach the boundary at a low angle are diverted from the core into the cladding, and there is no light transfer along the fiber. The acceptance angle of the fiber is influenced by the critical angle, described as a numerical aperture (NA). The NA is defined as follows, deriving from **Eqs. (5.9)** and **(5.10)**:

$$n_0 \sin \xi_m = n_1 \left\{ 1 - \left(\frac{n_2}{n_1} \right)^2 \right\}^{1/2} = \sqrt{n_1^{\,2} - n_2^{\,2}} = NA \tag{5.11}$$

A high value of NA will allow the light to transmit through the fiber near to the axis and at numerous angles, permitting efficient coupling of light transmitted into the fiber. On the other hand, it will also prompt increased dispersion of rays at different angles, which acquire different path lengths and different times of transmission through the fiber. The ratio of the change in the refractive index of the core and cladding is called a relative refractive index difference, and is described as follows:

$$\Delta = \left(\frac{n_1 - n_2}{n_1} \right) \tag{5.12}$$

As the refractive index for the atmosphere is n_0=1, the maximum acceptance angle ξ_m of the optical fiber can be found as follows:

$$\xi_m = \sin^{-1}(NA) \tag{5.13}$$

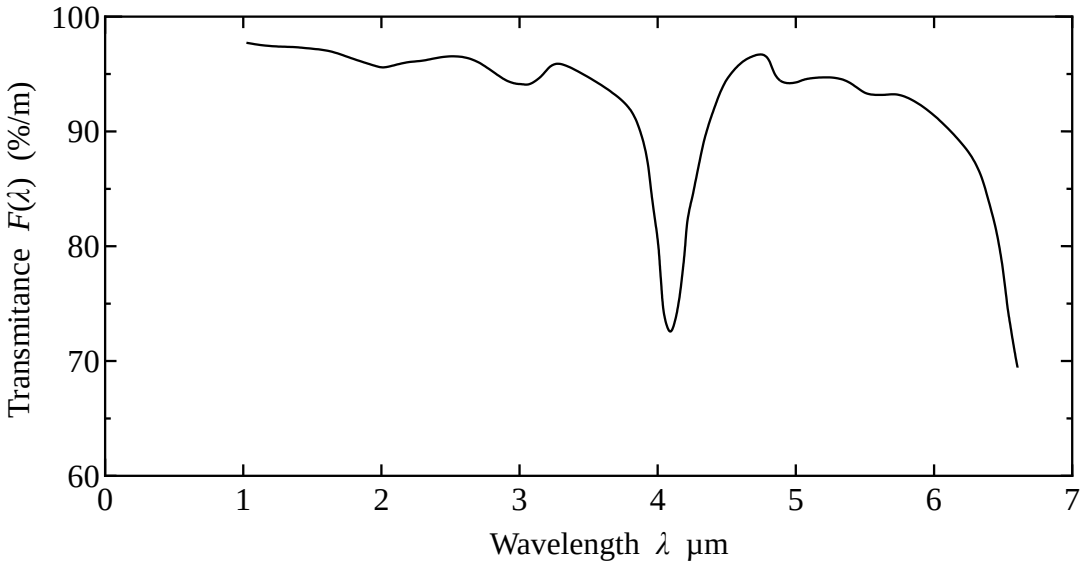

Fig. 5.5 Spectral transmittance of chalcogenide glass fiber

5.2.3 Characteristics of optical fiber

Within a continuous fiber, structural and chemical imperfections affecting absorption and scattering contribute to transmission loss. Absorption loss due to elements such as Cr, Mn, Co, Fe, Ni, Cu, and V inside the fiber material has been detected previously [11]. These elements, especially Cr and V, affect loss at $\lambda > 0.8$ μm. In this study, this type of absorption loss is insignificant due to the satisfactory reduction of the impurity. Meanwhile, density fluctuation in the fiber may also cause transmission loss, as all transparent materials have intrinsic spatial density fluctuation [11]. This fluctuation affects the refractive index fluctuation and subsequently the Rayleigh scattering. Curvature of the fiber routes allows an acceptable level of radiation loss in some modes. Geometrical non-uniformity at the core–cladding boundary also contributes to transmission loss. The surfaces at both ends of the optical fiber have to be smooth in order to inhibit this; these surfaces are therefore polished.

The NSG chalcogenide optical-fiber wavelength is shown in **Fig. 5.5**. It can be seen that it is possible to measure temperatures as low as 300°C using this optical fiber. **Table 5.1** shows the detailed characteristics of the NSG chalcogenide glass fiber [16].

5.2.4 Measuring area of the optical fiber

Fig. 5.6 (a) shows the schematic illustration of measuring area at the incidence face of the optical fiber. The fiber is placed perpendicular to and at a distance of *t* from the object.d_s is the diameter of the target area. **Fig. 5.6 (b)** shows the relationship between measuring distance, *t* and diameter of the target area, d_s. It can be seen that by increasing the measurement distance, the target diameter can also be increased. It has been shown previously that the measuring distance does not influence the output of the two-color pyrometer [5]. In this study, the measuring distances were fixed at 0.5 mm, yielding a target-area diameter of 0.74 mm.

Table 5.1 Specifications of chalcogenide glass fiber

Core diameter	d_c	400, 600	mm
Numerical aperture	NA	0.4	
Refrective index distribution		Step type	
Acceptance angle	ξ_m	23.58	deg

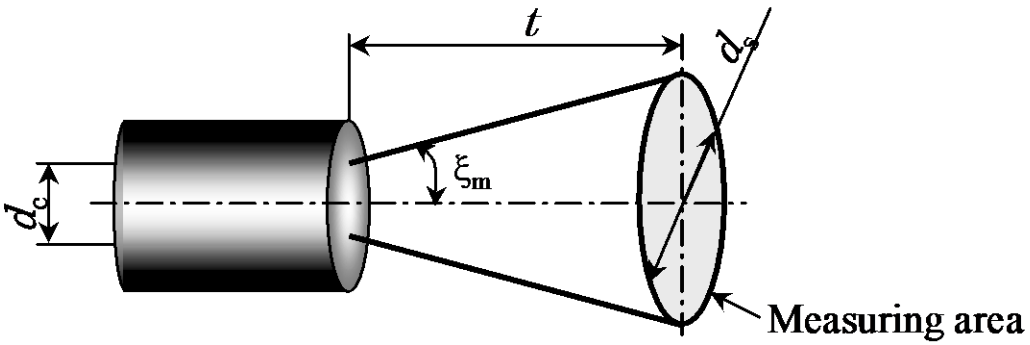

Fig. 5.6 (a) Schematic diagram of measurement area;

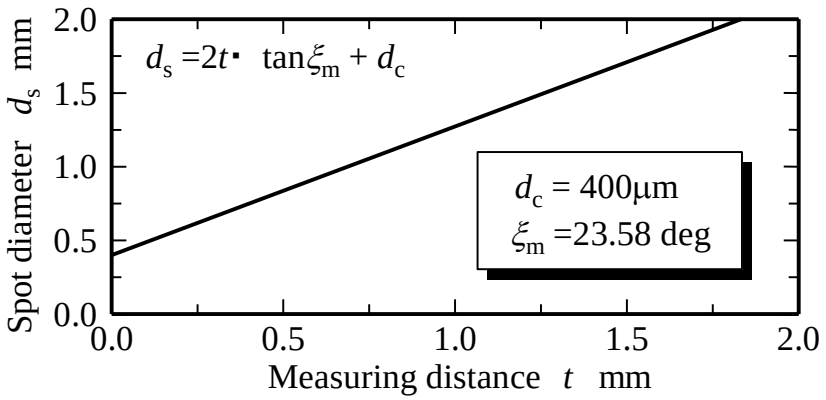

Fig. 5.7 (b) Relationship between measurement area and measurement distance

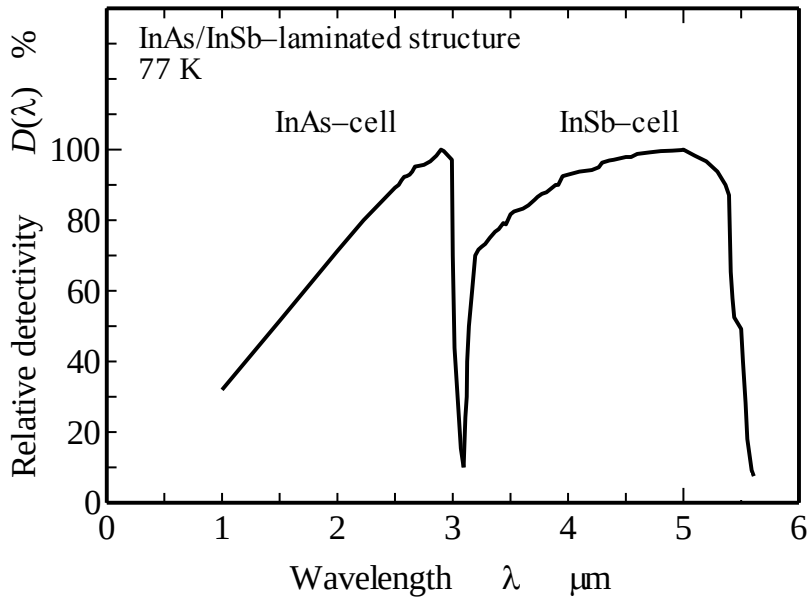

Fig. 5.7 Spectral transmittance of InAs and InSb detectors

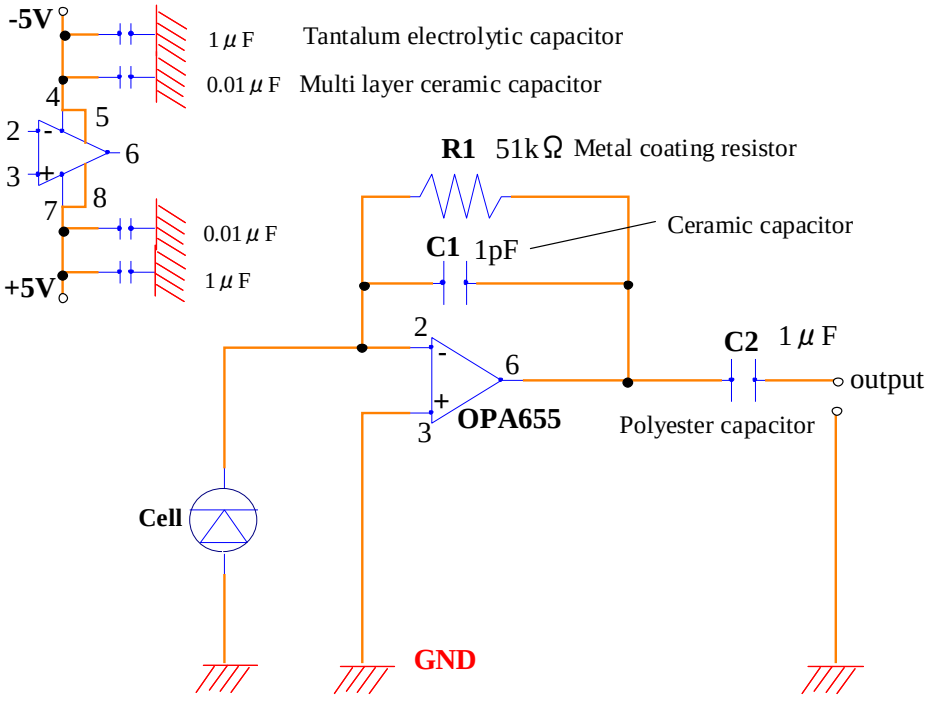

Fig. 5.8 Amplifier circuits of (a) InAs and (b) InSb detectors

5.3 Construction of pyrometer

Two types of infrared detector are available: thermal, and photon. Thermal detectors convert radiated power from infrared rays into measured parameters without any conversion. The bolometer [12], Gollay cell [13] and thermopile [14] are categorized as thermal detectors. On the other hand, photon detectors respond to incident radiation electronically. These types of detector respond much faster, as the radiation does not need to come from an object that is only being heated.

Photon detectors are subdivided into two distinct types: photoconductive and photovoltaic. These detectors differ in their construction. As suggested in the name, photoconductors are fundamentally poor conductors, whose conductivity is improved with the presence of photon-generated carriers; meanwhile, photovoltaic detectors are diodes that generate an electromotive force when photons are detected. The advantages of photovoltaic detectors over photoconductive detectors are improved theoretical limit to signal-to-noise ratio, modest biasing and more accurately predictable responsivity. Photovoltaic detectors are more delicate in comparison to photoconductors, however, as they are more vulnerable to electrical discharge and physical damage during handling.

In this study, Indium Arsenide (InAs) and Indium Antimony (InSb), are used as infrared detectors. The characteristic of InAs and InSb detectors are shown in **Table 5.2.** These detectors are mounted in a sandwich formation with InAs positioned in front of InSb. The range of detectable wavelength for the sensors' configuration is 1 μm to 5.5 μm; the range of InAs is from 1 μm to 3 μm, with the rest of the wavelength covered by InSb. **Fig. 5.7** visually explains the spectral transmittance of pyrometer sensors. It is crucial that these sensors are kept at a low operational temperature of 77K using liquid nitrogen.

Table 5.2 Characteristics of InAs and InSb detectors

Detector		InAs	InSb
Spectral respons range	[μm]	1.0~3.7	1.5~5.6
Peak sensitivity wave lngth	[μm]	3.1	5.1
Specific detectivity	D^* [cm·Hz$^{0.5}$/W]	4×10^{11}	7×10^{11}
Response time	[μs]	1	1
Operating temperature	[K]	77	77

The configuration of the chalcogenide fibers and detectors used in in the experiment is used to measure the temperature from the desired area. Due to the range covered by the chalcogenide fiber and the InAs/InSb detectors, the pyrometer range is between 1 and 5.5 μm. This set-up, which gives a flat response from 10 Hz to 400 Hz, is suitable for use in turning, with a good degree of accuracy. This pyrometer assembly has been successfully implemented in cutting and milling.

5.3.1 Amplifier

The infrared detectors built into the two-color pyrometer used in this study have a desired response time that is suitable for internal cutting at low and high speed. For this purpose, the response performance of the conversion amplification circuit is required to be higher than the response speed of the infrared detectors. **Fig. 5.8** shows the schematic diagram of the amplifier for the InAs and InSb cells. In this circuit, the output current from the infrared detecting element is amplified by converting it into a voltage by the amplifying circuit, and both the InAs element and the InSb element are placed in the same circuit. The frequency characteristic of the entire thermometer including this circuit is about 400 kHz (1 dB attenuation) and it has sufficient performance.

5.3.2 Pyrometer calibration

In measuring temperature using infrared signals, emissivity is encountered as a problem. To address this, two types of infrared sensor are used to measure the temperature from the infrared radiation, rather than just one. In this study, the oscilloscope records two signals. As mentioned above, the two-color detector comprises two distinct sensors: InAs positioned in front of InSb, both acts as a photovoltaic sensor. These detectors produce two electrical signals in millivolts that will be used to calculate the tool flank-face temperature. This avoids the emissivity problem.

In theory, this type of pyrometer is capable of measuring the total energy radiated from the surface of the target object. Here, the object is presumed to have a blackbody surface at uniform temperature with no losses to the surroundings. The calibration curve is based on the

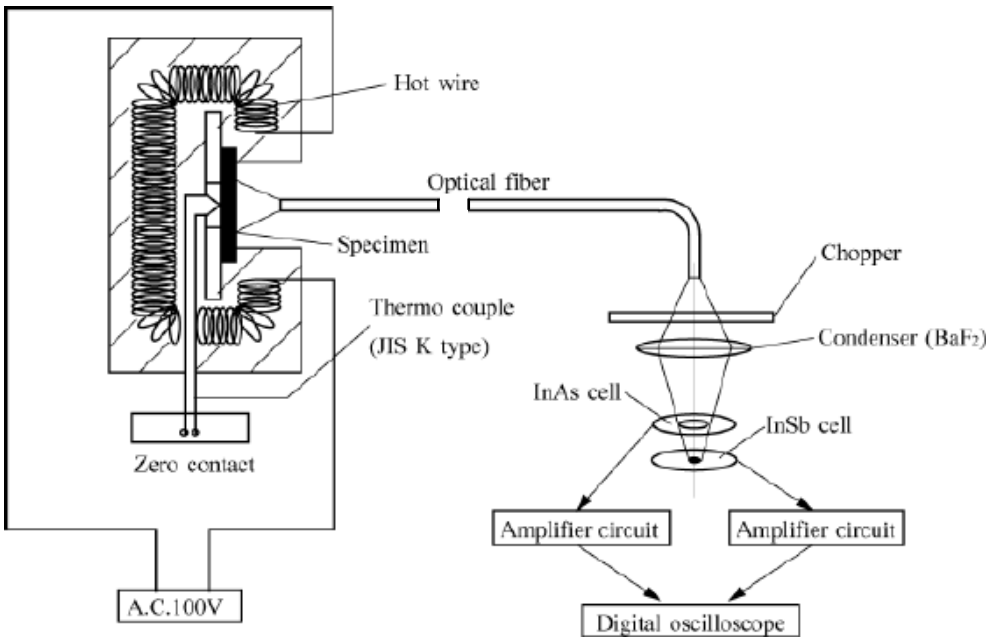

Fig. 5.9 Schematic set-up of pyrometer calibration

relative sensitivity of the pyrometer. This calibration curve is formulated based on the following formula:

$$\Lambda_{InAs/InSb} = \frac{\Lambda_{InAs}}{\Lambda_{InSb}} = \frac{\int_{\lambda_1}^{\lambda_2} \omega_1 \varepsilon_1(\lambda,T) E_{b\lambda}(\lambda,T) F(\lambda) D_{InAs}(\lambda) d\lambda}{\int_{\lambda_4}^{\lambda_3} \omega_2 \varepsilon_2(\lambda,T) E_{b\lambda}(\lambda,T) F(\lambda) D_{InSb}(\lambda) d\lambda} \tag{5.14}$$

where:

$E_{b\lambda}(\lambda,T)$: the spectral emissive power of a blackbody

$\varepsilon_1(\lambda,T)$, $\varepsilon_2(l,T)$: emissivity of the object

ω_1, ω_2 : constant

$F(\lambda)$: spectral transmittance of optical fiber

$D_{InAs}(\lambda)$, $D_{InSb}(\lambda)$: spectral transmittance of detector cell.

This calibration curve is then verified experimentally and compared to the theoretical curve.

In relating the voltage ratio to the temperature value, it is important to calibrate the detectors. This is done by using the heating element (TiN-TiCN-TiN), which is treated as a heating blackbody. **Fig. 5.9** shows the set-up for pyrometer calibration. This set-up calibrates the output voltage from the InAs/InSb detector and tests it against the theoretical curve obtained from the theoretical equation.

The temperature readings from the thermocouple are then plotted against the ratio from both detectors' output signals as shown in **Figs. 5.10**.

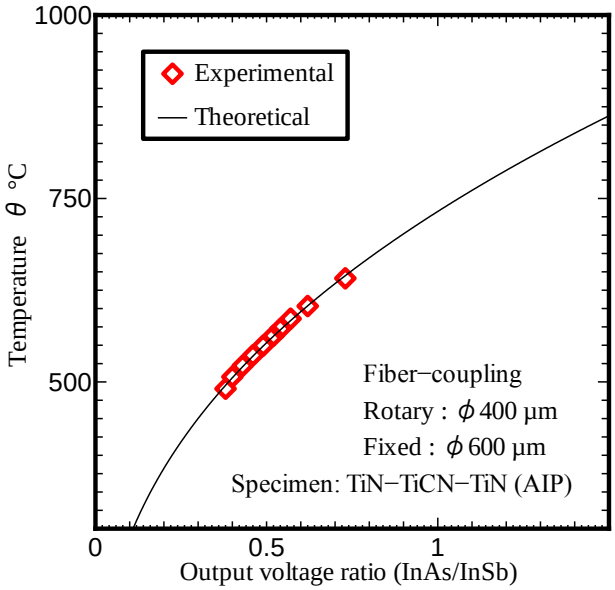

Fig. 5.10 Relationship between InAs/InSb output voltage ratio and object temperature (KT315)

5.4 Conclusions

This chapter has explained the temperature measurement technique that has been used in this study. The pyrometer set-up has been designed and proven to be able to measure temperature, even in MQL conditions. The conclusions of this chapter are as follows.

1. Temperature measurement is obtained using the voltage ratio of the InAs and InSb outputs. Emissivity is not a problem here and can be ignored.
2. A pyrometer assembly consisting of chalcogenide fiber and InAs and InSb detectors can be used for this study. Based on previous research, this pyrometer has a minimum detectible temperature of 350°C.

References

[1] Childs, T., Maekawa, K., & Obikawa, T. (2000). Metal machining theory and applications. London: Arnold.

[2] Ueda, T., Sato, M., Hosokawa, A. and Ozawa, M. (2008). Development of infrared radiation pyrometer with optical fibers – Two-color pyrometer with non-contact fiber coupler, CIRP Annals Manufacturing Technology, Vol. 57, No. 1, pp.69–72.

[3] Al Huda, M. Yamada, K. Hosokawa, A. and Ueda, T. (2002). Investigation of Temperature at Tool-Chip Interface in Turning Using Two-Color Pyrometer, Journal of Manufacturing Science and Engineering, Vol. 124, No. 2, pp.200

[4] Ueda, T. Al Huda, M., Yamada, K., and Nakayama, K., (1999). Temperature measurement of CBN tool in turning of high hardness steel CIRP Ann. – Manuf. Technol., Vol. 48, No. 1, pp.63–66.

[5] Ueda, T., Hosokawa, A., Oda, K., and Yamada, K., (2001). Temperature on Flank Face of Cutting Tool in High Speed Milling," CIRP Annals – Manufacturing Technology, Vol. 50, No. 1, pp.37–40.

[6] Chyssoloris, G., (1991). Heat Transfer and Fluid Mechanics for Laser Machining, in Laser Machining; Theory and Practice, New York, Springer, pp.92–195.

[7] Planck, M., (1901). Distribution of energy in the spectrum, Ann. Phys., 4(3), pp.553–563.

[8] Wien, W., (1984). Temperatur und Entropie der Strahlung, Ann. Phys., 52(2), pp.132–165.

[9] Boltzmann, L., (1884). Ableitung des stefan'schenGesetzesbetreffend der Abhangigkeit der Waermestrahlung von der Temperaturaus der electromagnetischenLichttheorie," Ann. Phys., 22(3), pp.291–294.

[10] Stefan, J., (1879). Ueber die Beziehungzwischen der Waermestrahlung und der Temperatur, Sitz-Ber.Akad. Wiss. Wien, 79, pp.391–428.

[11] Okoshi, T., (1982) Optical fiber, New York, Academic Press.

[12] Strong, J. and Lawrence. Jr., P.W., (1968). Bolometer theory, Appl. Opt., 7, pp.49.

[13] Golay, M.J.E., (1947). A pneumatic infrared detector, Review of Scientific Instruments, 18, pp.357.

[14] Stevens, N.B., (1987). Radiation thermopiles, Vol. 5, New York, Academic Press, pp. 287.

[15] Nishimoto, H., Tanaka, R., Hosokawa, A., Ueda, T., and Furumoto, T., (2012). Development of Tool Edge Temperature Measurement Method in Wet Cutting, Journal of Advanced Mechanical Design, Systems, and Manufacturing, Vol. 6, No. 6, pp.916–922.

[16] "Infrared Transmitting Filters." Infrared Transmitting Filters from HOYA OPTICS: Leading Supplier of Advanced Optical Materials & Components. N.p., n.d. Web. 03 Jan. 2017.

CHAPTER 6

INFLUENCE OF EXTREME COLD MIST ON MACHINABILITY OF STAINLESS STEEL (SUS316)

6.1 Introduction

During the cutting process of difficult-to-cut material, excessive heat generation is one of the main problems related to the severe tool wear occurrences and surface finish deterioration. This is due to a large amount of energy is needed to overcome the mechanical and chemical properties of difficult-to-cut material during the process [1]. Several approaches are taken into consideration to enhance the tool performance [1-4]. Previous studies showed that, the dry machining is the optimum solution in most of the cutting process of soft and mild material [5]. However, the method is less effective in machining difficult-to-cut material. A near-dry cutting condition is proposed where Minimum Quantity Lubrication (MQL) is implemented into the cutting process. In MQL, tool-chip interface (cutting zone) is supplied with a small amount of cutting in the form of micro scale droplets [4]. There are several types of MQL cutting fluids; oil-based cutting fluid in terms of lubrication and emulsion-based (made of soluble oil in water), water-based or air-based cutting fluids in terms of coolant [4].

During the lubrication process, MQL system is capable of reducing the friction on the contact between tool, chip and workpiece, while during the cooling process; MQL system is capable of providing efficient heat exchange through conduction. As for the example, water based MQL has higher specific heat capacity compared to oil based cutting fluid [4]. Thus, it

is proven that, the MQL is able to improve the tribological characteristic of the interfaces, along with conducting away the excessive heat from the cutting zone [1-4].

In this study, the application various types of MQL methods are tested in turning process of difficult-to-machine materials, stainless steel SUS316. The efficiency of each MQL system in improving the machinability of stainless steel SUS316 is analyzed in terms of cutting force F and cutting temperature T with relative assessment with dry cutting, along with finish surface roughness.

6.1.1 Difficult to cut material, stainless steel SUS316

Stainless steel, SUS316 is an austenitic chromium nickel stainless steel consisting of molybdenum, as shown in **Table 6.1**, which increases resistance to corrosion. The molybdenum element enhances the resistance to chloride ion solutions, and provides extended strength at high temperatures. Stainless steel SUS 316 is applied generally in the industrial sector that involves processing chemicals, as well as deep-sea environment, such as coastal regions, and outdoor areas where applications of de-icing salts are routine [6].

Table 6.1 Stainless Steel SUS 316 Material composition

Element (%) / Material	**Cr**	**Ni**	**C**	**Mn**	**Si**	**P**	**S**	**N**	**Mo**
SUS316	16–18	10–14	0.08	2	0.75	0.045	0.03	0.10	**2.0 –3.0**

6.1.2 Application of pyrometer for temperature measurement

Fig. 6.1 shows schematic diagram of the two-color pyrometer applied in the experiment. During the cutting process, fiber-coupling method is applied. In this method, a small-diameter optical fiber-A (400μm) is fixed into the workpiece, sighting on the infrared radiated from the heat source (cutting tool edge). The fiber is rotated together with the workpiece, accepting the radiation energy, and transmitting it to the large diameter optical fiber-B (600μm), and then to the two-color pyrometer.

The pyrometer is constructed from a sequence arrangement of photovoltaic InAs and InSb sensors, where InSb sensor is placed at the back surface of InAs sensor **(Fig. 6.1 (b))**. Temperature measured by the pyrometer is estimated from the output ratio of both sensors. The pyrometer is highly responsive, and a stable output is obtainable with respect to the input up to 100 kHz input from a minuscule size of measurement area. Previous studies have successfully measured the temperature from various machining processes, and it is proven that it is possible to measure cutting temperature under the supply of oil mist by the pyrometer [6].

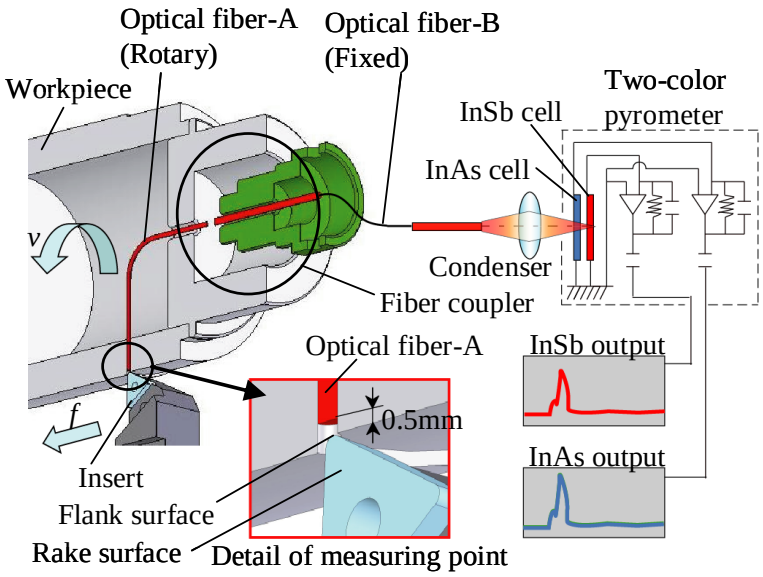

Fig. 6.1 Detail of measuring point of tool edge temperature

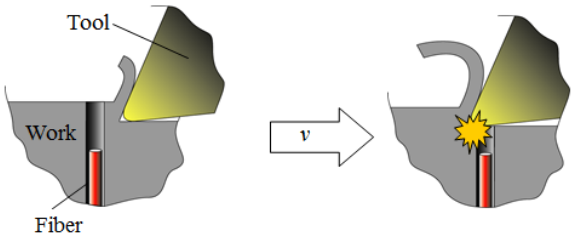

Fig. 6.2 Sudden acceleration detection by acceleration pickup

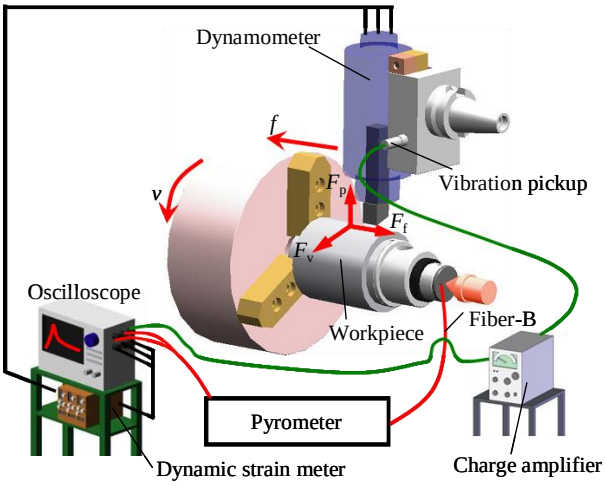

Fig. 6.3 Overall experimental setup

6.2 Methodology

6.2.1 Experimental procedure

In this study, a special design workpiece for optical fiber application in temperature measurement is prepared, as shown in **Fig. 6.1**. The temperature at the flank surface of cutting edge is measured when the tool pass through the hole where the fiber was fixed **(Fig. 6.2(a))**. Accurate timing of sensor output is taken by an acceleration pickup; in obtaining sudden acceleration as the tool edge hit the hole **(Fig. 6.2(b)).** Cutting forces are measured by a strain gauge dynamometer while cutting temperature is measured by the two-color pyrometer. In this study, stainless steel SUS316 is selected as workpiece. Overall experimental setup is shown in **Fig. 6.3**, while, material properties and main experimental conditions are shown in **Table 6.2** and **Table 6.3.**

6.2.2 Minimum quantity lubrication (MQL) system

In this study, a system capable of supplying several types of heterogeneous Minimum Quantity Lubrication (MQL) cutting fluids to the rake and flank surface of the cutting tool are designed. MQL with lubrication characteristic is supplied onto the rake face of the tool by rake face nozzle. The characteristics of cutting fluids applied in the study and MQL systems are shown in **Table 6.4** and **Table 6.5**, respectively. Hydroscopic oil mist with coolant characteristic is supplied onto flank face with the application of flexible nozzle (**Fig.6.4**) in MQL system Type D. For MQL system Type C and E, the flexible nozzle is connected to an air cooler, which is connected to an air dryer to supply extreme cold air (-13.6°C).

Table 6.2 Material properties

Materials	TiCN-coated Cermet	SUS316
Young Modulus, E (GPa)	**650**	**205**
Poisson Ratio, ε	**0.25**	0.30
Thermal Conductivity, k (W/(m·K))	**59**	**17**
Density, ρ (kg/m^3)	**14900**	**8070**
Volumetric Heat Capacity, c ($\times 10^6$ J/(m^3·K))	**15.0**	**2.78**
Hardness Vickers, $HV_{0.3}$ (GPa)	**13.7**	**2.2**

Table 6.3 Cutting condition for conventional turning

Workpiece		Stainless Steel (SUS316)
Cutting Tool Model Nose Radius Rake Angle, α Insert	: : : :	TNMGM1600408 0.8(mm) -6 (°) TiCN Coated Cermet
<u>Cutting Condition</u> Cutting Speed Depth of Cut Feed Cutting Style	 : : : :	 50 ~ 200(m/min) 0.5(mm) 0.3(mm/rev) Dry, Various types of dual spray MQL, MQL and cold air

Table 6.4 Characteristic of cutting fluid for conventional turning process

Fluid Type Oil A Oil B	 Vegetable oil Hydroscopic oil
Viscosity [mm^2/s]	37
Oil Contents [%] Oil A Oil B	 99 30
Oil Pressure [Mpa] Cold air Pressure [Mpa]	0.6 0.6
Cold air temperature [˚C]	-13.6

Table 6.5 Variation of MQL supplying system applied

System Type	MQL type for rake face	Fluid rate (mL/h)	MQL type for flank face	Fluid rate (mL/h)	Total fluid rate (mL/h)
Dry	**Dry**	**-**	**Dry**	**-**	**-**
A	**Oil A**	**30**	**Dry**	**-**	**30**
B	Oil B	100	Dry	-	100
C	**Oil A**	**30**	**Cold air**	**-**	**30**
D	Oil A	30	Oil B	100	130
E	**Oil A**	**30**	**Cold air + Oil B**	**100**	**130**

It should be noted that in MQL system type A and B, cutting fluid is supplied onto the rake face only. In MQL system type C, D and E, Oil A is supplied onto the rake face while various combinations of hydroscopic oil (Oil B) and cold air are supplied onto the flank face. MQL system Type E is the important Extreme Cold Mist system, which will be focused on throughout the study.

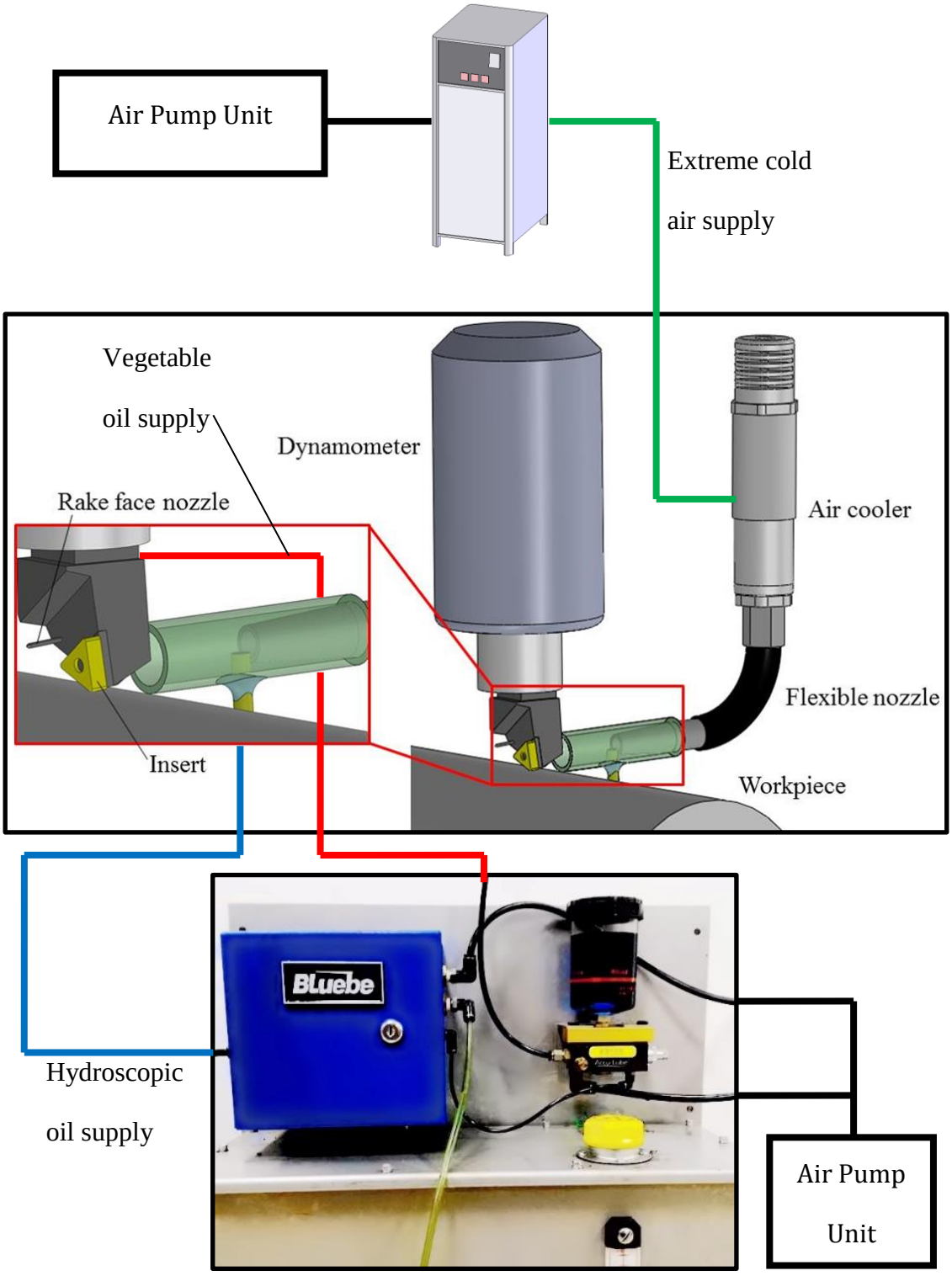

Fig. 6.4 MQL supplying method onto rake and flank face of the tool during cutting process

6.3 Results and discussions

6.3.1 Influence of MQL onto cutting force on cutting process stainless steel SUS316

Figs. 6.5 (a), 6.5 (b) and 6.5 (c) show the relationship between cutting speed v_c and cutting force components: principal force F_p, thrust force F_t, and feed force F_f, for the cutting process of stainless steel (SUS316) with TiCN-coated cermet cutting tool, respectively. The cutting process involves several types of MQL systems, for depth-of-cut a=0.5 mm, and feed rate f=0.3 mm/rev.

It is observed that the cutting force F decreases as the cutting speed v_c increases. The principal force F_p decreases up to approximately 50N with the application of MQL Type A and E, while feed force F_f and thrust force F_t decrease up to nearly 30N and 60N, respectively with the application of MQL Type E.

It is assumed that the oil mist can penetrate the contact zone between chip and tool with high efficiency for MQL system Type A and Type E, where both systems are capable of reducing the principal force, F_p effectively. However, only MQL system Type E is able to reduce the feed force F_f and thrust force F_t with higher efficiency. This is due to the MQL system Type E is capable of reducing the temperature at the tool flank with its extremely low temperature cold mist and higher total fluid rate.

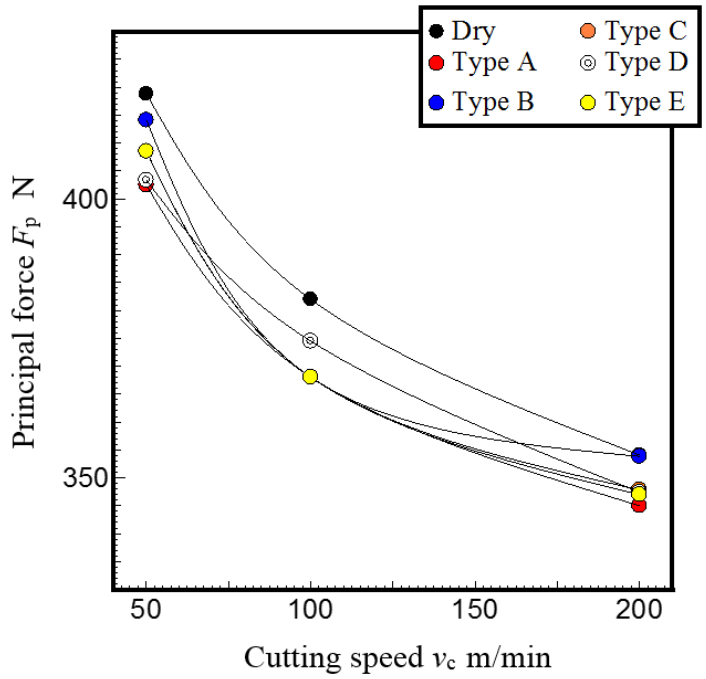

Fig 6.5 (a) Relationship between cutting speed v_c and principal force F_p for various MQL systems

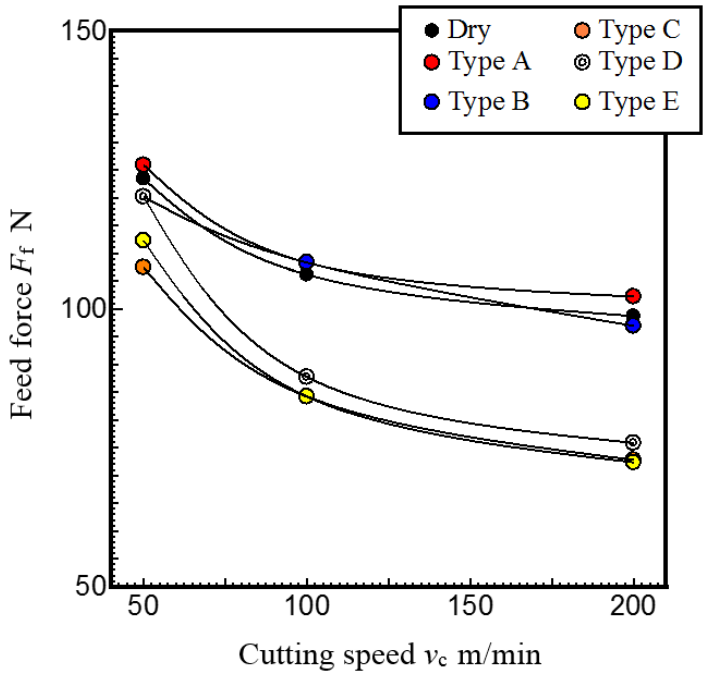

Fig 6.5 (b) Relationship between cutting speed v_c and feed force F_f for various MQL systems

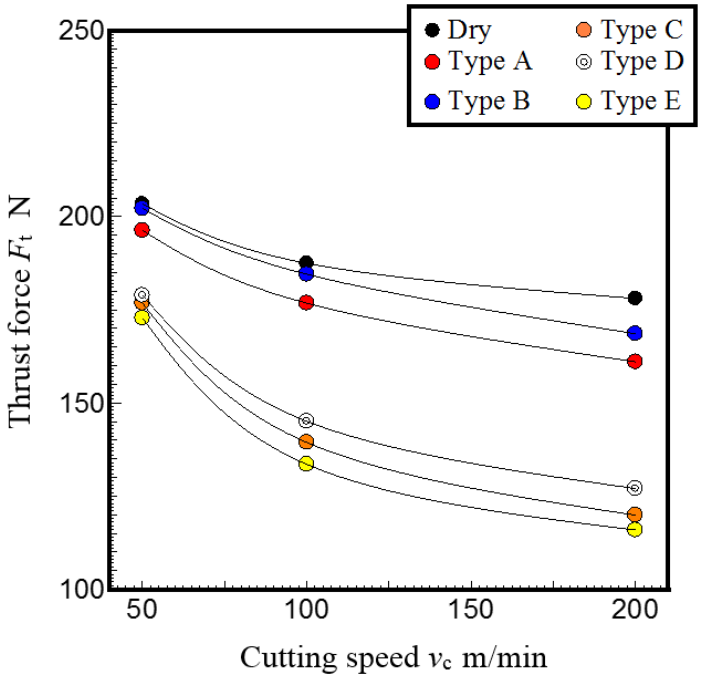

Fig 6.5 (c) Relationship between cutting speed v_c and thrust force F_t for various MQL systems

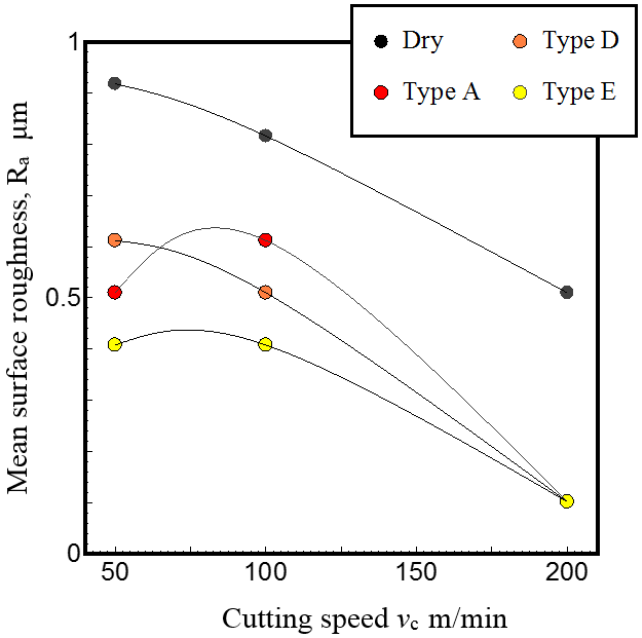

Fig 6.6 (a): Relationship between cutting speed v_c and mean surface roughness R_a for various MQL systems

6.3.2 Influence of MQL onto surface roughness on cutting process stainless steel SUS316

Fig. 6.6 (a) shows the relationship between cutting speed v_c and mean surface roughness, R_a (during the cutting process of stainless steel SUS 316 with TiCN-coated cermet cutting tool in dry and MQL system Type A, C and E for depth-of-cut a=0.5 mm and feed rate f =0.3 mm/rev cutting conditions.

It is observed that, the mean surface roughness R_a decreases as cutting speed v_c increases. Meanwhile, MQL system Type E shows the lowest mean surface roughness R_a followed by MQL system Type C. It can be understood that, the low-temperature MQL is capable of increasing the tool rigidity and increasing the smoothness of chip flow. The MQL System type E can reduce the frictional coefficient along with tool temperature, improving the surface roughness of the machined surface, as shown as in **Fig. 6.6 (b).**

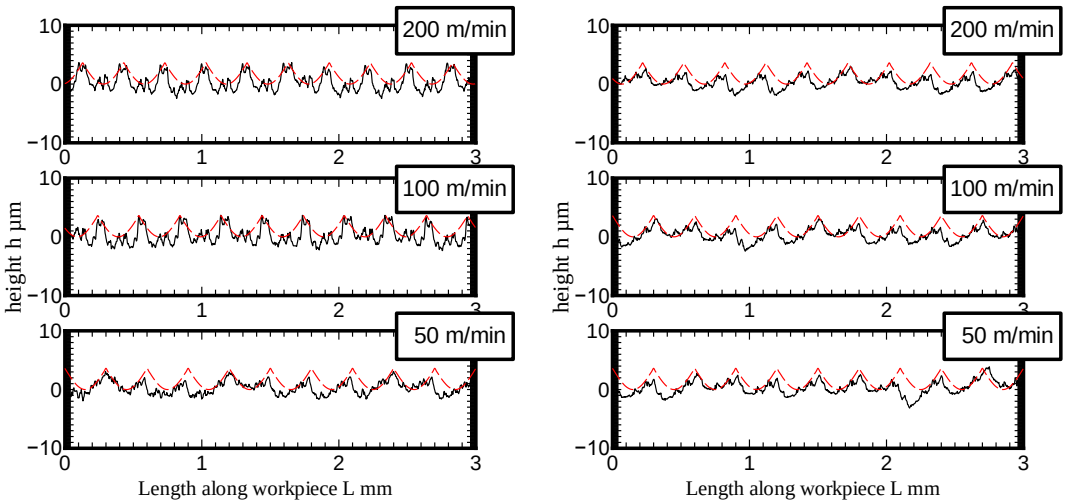

Fig 6.6 (b) Surface roughness profile comparison between MQL system Type A (left) , MQL system Type E (right) and ideal surface roughness profile (red line)

6.3.3 Influence of MQL onto tool edge temperature on cutting process stainless steel SUS316

Fig. 6.7 shows the relationship between cutting speed v_c and tool edge temperature, θ (during the cutting process of stainless steel (SUS 316) with the TiCN-coated cermet cutting tool in dry and MQL system Type A, C and E. Typical output reading is shown in **Fig. 6.8**.

It is observed that, the cutting temperature of Extreme Cold Mist system shows the lowest tool edge temperature, up to 100~150°C compared to dry cutting condition, and up to 50°C compared to MQL system Type C. It can be assumed that during the Extreme Cold Mist system, the tool edge is cooled by forced heat convection of extreme cold air, plus with latent

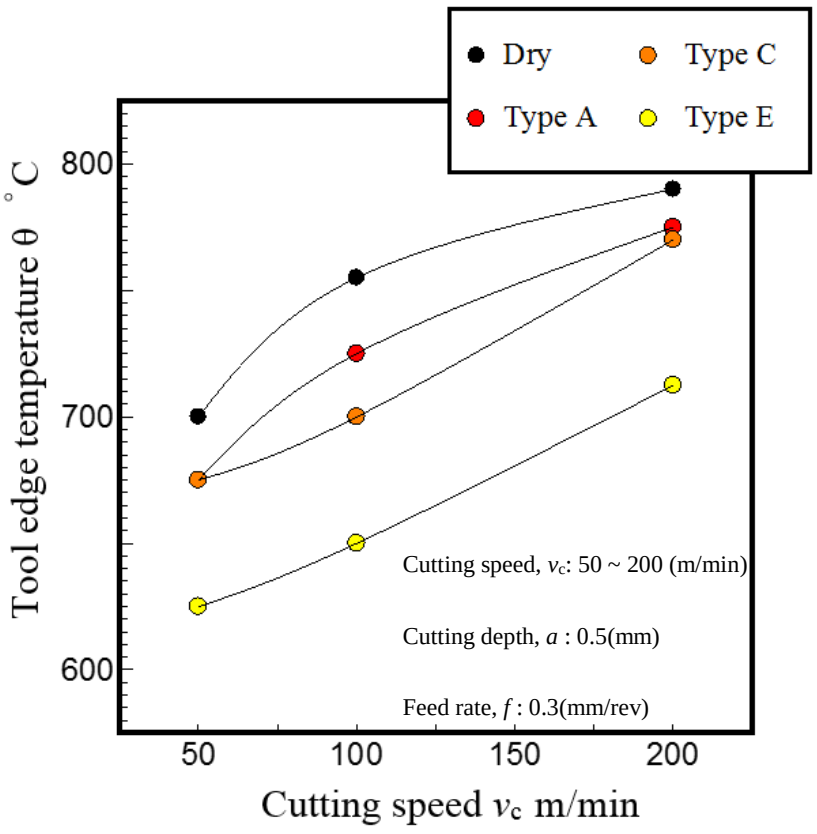

Fig. 6.7 Relationship between relationship between cutting speed v_c and tool edge temperature, θ for various MQL systems

heat of oil mist (Hydroscopic oil).

Additionally, in MQL system Type E (Extreme Cold Mist system), the lubrication is improved and cutting chip is removed smoothly (refer to **Fig. 6.6**). Thus, the temperature is reduced further due to stable cutting process.

In term of cutting efficiency, by taken into consideration of the tool edge temperature for cutting speed 200 m/min for MQL system Type E (Extreme Cold Mist system), which is 700°C, the equivalent temperature for dry cutting process is at the cutting speed of 50 m/min. Thus, the cutting efficiency through the application of MQL system Type E (Extreme Cold Mist system) is **200/50 = 4 times** higher than dry cutting.

In MQL System Type C, where only extreme cold air is supplied onto the flank face, it is assumed that heat convection of temperature from the tool surface is insufficient and ineffective compared to the mixture of cold air and hydroscopic oil mist. Additionally, it was found during the study that, when the hydroscopic oil that contains a lot of water is supplied

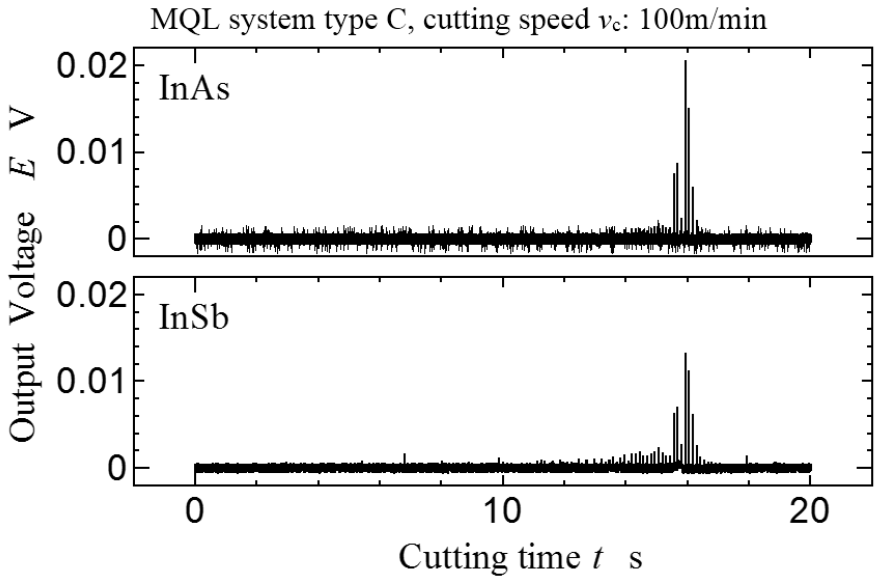

Fig. 6.8 Typical output signal by the two-color pyrometer

with lower flow rate; the oil agent freezes when the cold air mist gets below the freezing point, removing the original lubricity. However, the system is improved by increasing the flow rate of the hydroscopic oil supply several times higher, where the original lubricity is maintained without freezing even at freezing temperatures. Along with the best results of cutting resistance, finish surface roughness, and tool flank temperature obtained during the cutting process, it can be concluded that, MQL system Type E (Extreme Cold Mist system) is the best MQL system based on the current study.

6.4 Conclusions

In this study, turning processing experiments were conducted on stainless steel (SUS316) with the application of various MQL conditions. Cutting force was measured and the effect of cold air was studied. Several conclusions can be made as following.

(1) Supplying vegetable oil to the rake face is able to reduce principal cutting force F_p up to 50N compared to the dry method, whereas the vegetable oil mist is able to lubricate the contact surface between tool and chip.

(2) By supplying cold air (–13.6°C) with hydroscopic oil (Extreme Cold Mist system) at 100mL/h volume rate, the system is able to reduce the feed force F_f and thrust force F_t up to 30 N and 60 N compared to dry method, respectively.

(3) By supplying cold air (–13.6°C) to the flank face (Extreme Cold Mist system), the finished surface roughness is greatly improved compared with the dry method.

(4) By supplying cold air (–13.6°C) to the flank face (Extreme Cold Mist system), cutting temperature is reduced up to 100~150°C compared to dry cutting condition.

(5) During the application of Extreme Cold Mist system, the effectiveness of cutting process is increased 4 times higher than dry cutting.

(6) Based on the best results obtained from cutting force, finish surface roughness and tool flank temperature, it can be concluded that Extreme Cold Mist system is the best MQL system in the current study.

References

[1] El-Wardany, T., Mohammed, E., & Elbestawi, M. (1996). Cutting temperature of ceramic tools in high speed machining of difficult-to-cut materials. *International Journal of Machine Tools and Manufacture,36*(5), 611-634.

[2] Debnath, S., Reddy, M. M., & Yi, Q. S. (2014). Environmental friendly cutting fluids and cooling techniques in machining: a review. *Journal of Cleaner Production,83*, 33-47.

[3] Shyha, I., Gariani, S., & Bhatti, M. (2015). Investigation of Cutting Tools and Working Conditions Effects when Cutting Ti-6al-4V using Vegetable Oil-Based Cutting Fluids. *Procedia Engineering,132*, 577-584.

[4] Priarone, P. C., Robiglio, M., Settineri, L., & Tebaldo, V. (2015). Effectiveness of Minimizing Cutting Fluid Use when Turning Difficult-to-cut Alloys. *Procedia CIRP,29*, 341-346.

[5] Agustina, B. D., Bernal, C., Camacho, A., & Rubio, E. (2013). Experimental Analysis of the Cutting Forces Obtained in Dry Turning Processes of UNS A97075 Aluminium Alloys. *Procedia Engineering,63*, 694-699.

[6] Tsisar, V., Kondo, M., Muroga, T., Nagasaka, T., & Matushita, I. (2012). Morphological and compositional features of corrosion behavior of SUS410–SUS410, SUS316–SUS316 and SUS410–SUS316 TIG welded joints in Li. *Fusion Engineering and Design,87*(4), 363-368.

[7] Ueda, T., Hosokawa, A., & Yamada, K. (2006). Effect of Oil Mist on Tool Temperature in Cutting. *Journal of Manufacturing Science and Engineering,128*(1), 130.

[8] Rahim, E., Ibrahim, M., Rahim, A., Aziz, S., & Mohid, Z. (2015). Experimental Investigation of Minimum Quantity Lubrication (MQL) as a Sustainable Cooling Technique. Procedia CIRP, 26, 351-354.

CHAPTER 7

CONCLUSION

This study aims to make it clear about the lubrication and cooling effects in MQL during cutting process through simulation analyses and experimental validation, as well as proposing a new MQL system in improving the cutting process of difficult-to-cut material. Several MQL systems are tested, and cutting characteristic for each system is analyzed. In the early stage of the study, two FEM models are utilized to evaluate MQL. While later in the study, a new MQL system is proposed and tested on cutting process difficult-to-cut material. The new MQL system is proven able to decrease cutting force, suppressing the increment of cutting temperature and extending the tool life.

It is revealed through the study that, supplying heterogeneous oil MQL is considered as a method with high possibility. Several parameters, such as direction and range of the MQL nozzle, and flow rate significantly affect the efficiency within the system, where the ability to supply MQL accurately onto the cutting zone is important.

In the study, FEM evaluation of the influence of the MQL in cutting process of mild steel S45C is discussed. Two serial FEM analytical orthogonal models were designed and executed using the application package software Deforms™-3D. Orthogonal cutting tests of medium steel JIS S45C was executed with the TiCN-coated cermet tool in order verify the FEM models. Three significant parameters (MQL friction coefficients; chip thickness and contact length) are observed from the orthogonal cutting experiment and considered as important MQL parameters. Finally, evaluation with the finite-element method is executed by

the application of DEFORM™-3D software. It is proven that, FEM is capable of evaluating the MQL characteristic with a good degree of accuracy.

Chapter 2 explains the fundamental understanding that is needed on mechanics, parameters, models, and formulations involved in metal cutting, that is needed in designing an effective FEM model. Cutting process is complicated, whereas involvement of numbers of parameters, affected the process outcomes. Characteristics for several FEM models were discussed, from simplified 2D orthogonal cutting model to complex 3D cutting model in FEM to imitate the actual process. It is an invaluable effort, in improving the knowledge and understanding, as well as increasing the efficiency in production and manufacturing systems and industries.

In Chapter 3, several FEM models in evaluating MQL were designed for the application of SFTC DEFORM™-3D. Equivalent orthogonal cutting process of the medium carbon steel, JIS S45C, is also executed. The FEM models are considered interrelated, and the validity of the models is verified by the experimental data for dry and MQL cutting tests. Experimentally obtained data, such as the cutting force, MQL friction coefficient μ_{MQL}, contact length l_c, and chip thickness t_c, is utilized in validating the FEM mode. FEM model with Arbitrary Lagrangian-Eulerian (ALE) formulation applied pre-determined chip thickness along with MQL friction coefficients. It is found that, the cutting force has a direct relationship with MQL friction coefficient and chip thickness. This phenomenon is proven by FEM, where the varying MQL friction coefficient inputs obtained from the experimental procedure on various types of MQL affected the estimated cutting force. The FEM shows significant accuracy with the experimental results. The study shows that, the FEM can aid in understanding the influence of MQL during the cutting process, in terms of lubrication effect.

In Chapter 4, the FEM model is designed with the convective heat transfer coefficients is taken into consideration in evaluating the effect of MQL as coolant. Experimental procedure for temperature measurement with the application of thermocouple is executed. Mean temperature for each MQL system is measured and the effect of MQL as a coolant is observed. It is found that MQL system with the convective heat transfer coefficients can reduce the cutting temperature during the experiment. This characteristic is taken into consideration and FEM evaluation on MQL in terms of cooling effect is done. FEM results show good agreement with the experimental data, thus it is proven that cooling type MQL requires cutting fluids that have a higher convective heat transfer coefficient. This information is appreciated in surveying new type of MQL system, where Extreme Cold Mist MQL system is proposed and utilized during the cutting process difficult-to-cut material.

Chapter 5 explains the temperature measurement technique that has been used throughout this study. The pyrometer setup has been designed and proven to be able to measure temperature, even in wet conditions, whereas temperature measurement is obtained using the voltage ratio of the InAs and InSb outputs.

In Chapter 6, conventional turning process is executed on stainless steel (SUS316) with the application of various MQL conditions, including the surveyed MQL system in Chapter 4, Extreme Cold Mist system. Cutting force was measured and the effect of cold air was studied. It is proven that, supplying vegetable oil to the rake face can reduce principal cutting force component F_p up to 50N compared to the dry type, whereas the vegetable oil mist capable of lubricating the contact surface between tool and chip. However, by utilizing Extreme Cold Mist system, (cold air (–13.6°C) + hydroscopic oil with 100mL/h volume rate), capable of decreasing feed force F_f and thrust force F_t component up to 30 N and 60 N compared to dry type, respectively. Additionally, by applying Extreme Cold Mist system (–

13.6°C) to the flank face, the finished surface roughness is greatly improved compared with the dry type. This is supported by the results of tool edge temperature where it is proven that the Extreme Cold Mist system can reduce the cutting temperature significantly, thus it is assumed capable to reduce tool wear and increase tool life.

The study showed the capability of FEM in evaluating the influence of MQL, validated by the experimental works, not only from the view of improvement of manufacturing understanding and efficiency, but also in tribological and material perspective. It is recommended that, mechanic of contact during the cutting process to be viewed in molecular level, in improving the understanding the mechanic of MQL during contact between two surfaces, especially in the case of cutting process. Further study can be done in various types of MQL, such as high-pressure coolant and cryogenic cutting process and cutting process of difficult-to-cut material. Furthermore, the proposed FEM process can be utilized in estimating principal force, F_p, thrust force, F_t, chip thickness, t_c and contact length, l_c with a good degree of accuracy. New MQL systems can be developed, and more studies can be done with the application of FEM in the future.

LIST OF PUBLICATIONS

1. Ahmad Shahir Jamaludin, Akira Hosokawa, Tatsuaki Furumoto, Tomohiro Koyano, Yohei Hashimoto, "Evaluation of the Minimum Quantity Lubrication in Orthogonal Cutting with the Application of Finite Element Method", International Journal of Mechanical and Mechatronics Engineering IJMME-IJENS, Accepted on January 22nd 2017.

2. Ahmad Shahir Jamaludin, Akira Hosokawa, Tatsuaki Furumoto, Tomohiro Koyano, "Studies on Effective Parameters for FEM Analysis of MQL Cutting", International Design and Concurrent Engineering Conference 2015, Tokushima, Japan, September 7, 2015.

ACKNOWLEDGEMENT

This dissertation will not be possible without the help of numerous individuals in so many ways. Firstly, I would like to express my deepest gratitude to my supervisor, Prof. Akira Hosokawa for the precious guidance, advises and encouragements that have been provided throughout my research, as well as being my supportive mentor during my Bachelor study.

I am also would like to thank Assocs. Prof. Tatsuaki Furumoto for the helps, and guidance that he gave me, a very deep appreciation to Prof. Asakawa Naoki for the motivational support and Prof. Ryiochi Monzen for guidance throughout my study.

I would like to thank Dr. Tomohiro Koyano and Dr. Yohei Hashimoto for their technical supports and all the members of Manufacturing Systems Laboratory for the advices and the help during the presentation and experiments.

I would like to express my deepest love and thankfulness for my wife, Norasilah Ali and my sons Amir Safwan and Lutfi Haris for being supportive, patience and all the prayers during the struggling period of my research.

I also would like to extend my appreciation and gratitude towards Malaysian community in Kanazawa for their invaluable help.

I am also would like to express my sincere thanks the Okuma Co. Ltd. for providing us with the precious machining center and turning lathe. Finally yet importantly, I am grateful to Ministry of Education, Malaysia and Universiti Malaysia Pahang for their financial supports during my studies at Kanazawa University.